Fundamental Study on Thermally and Chemically Robust Molecular Sensors

李, 文君

Fundamental Study on Thermally and Chemically Robust Molecular Sensors

A DISSERTATION SUBMITTED TO

INTERDISCIPLINARY GRADUATE

SCHOOL OF ENGINEERING SCIENCE,

KYUSHU UNIVERSITY

IN PARTIAL FULFILLMENT OF REQUIREMENTS FOR THE DEGREE OF

DOCTOR OF PHILOSOPHY IN ENGINEERING

LI WENJUN

February 2022

Acknowledgements

This work was conducted at the Institute for Materials Chemistry and Engineering, and the Department of Molecular and Material Sciences in Interdisciplinary Graduate School of Engineering Sciences, Kyushu University, during the period 2017-2022.

I would like to thank my supervisor, Prof. Takeshi Yanagida for granting me the opportunity to undertake my PhD research program. I would like to express my sincere gratitude to Prof. Kazuki Nagashima from his extensive and profound knowledge, opinions and keen interests in scientific research. I wish to thank the other staffs in our Laboratory, Prof. Tsunaki Takahashi, Prof. Takuro Hosomi, Dr. Masaki Kanai, Dr. Masaru Suzuki, Dr. Xixi Zhao and Dr. Benjarong Samransuksame and Dr. Jiangyang Liu for their constructive advices and technical supports of various experiments for my research.

I would like to take this opportunity to thank several former staffs, Prof. Yong He, Prof. Guozhu Zhang, Dr. Mickael Boudot, Prof. Gang Meng, Prof. Fuwei Zhuge, Dr. Yosuke Hanai for their insightful advices and constructive discussions. I really thank to the secretary in our Laboratory, Ms. Hiroko, Imaizumi and Ms. Maki Inuoe for their kind help in my daily life and study.

I would like to sincerely thank our excellent collaborators, including Mr. Atsuo Nakao and Mr. Atsuhi Shunori from Panasonic Corporation, Prof. Wataru Mizukami and Prof. Yuriko Aoki from Kyushu University.

In addition, I thank all current members in our Laboratory: Mr. Kentaro Nakamura, Mr. Ryoma Kamei, Mr. Haruka Honda and Mr. Yusuke Tonomoto. They were good supporters in my research and daily life. And I acknowledge all alumni in

our Laboratory: Dr. Zetao Zhu, Dr. Hao Zeng, Dr. Ruolin Yan, Dr. Hiroshi Anzai, Mr. Masahiro Shimuzu, Mr. Satoru Shiraishi, Mr. Mizuki Matsui, Mr. Shojiro Hayata, Mr. Hiroki Yamashita, Mr. Yuki Nagamatsu, Mr. Kentaro Nakabayashi, Mr. Yuya Akihiro, Mr. Junxion Zhang, Ms. Mengke Pei, Mr. Rimon Yamaguchi, Mr. Sameh Okasha, Mr. Akihide Inoue, Ms. Chie Nakamura.

I would like to guive special thanks to my dear friend Prof. Chen Wang, Mr. Chaiyanut Jirayupat, Ms. Yuqing He and Ms. Kasumi Nagata, who has always believed in me and encouraged me to help me through the darkest times.

Last but not the least, I want to thank my lovely friends and families. Their love, understanding and encouragement give me great support during my PhD research.

Wenjun Li

Abstract

This dissertation is dedicated to the fundamental study of chemical reactions on polymer and metal oxide for realizing the robust and molecular selective gas sensors. Gas sensors have been used in a wide range of industrial and domestic applications, such as petroleum, chemical, steel, metallurgy, mining, environmental protection, municipal, medical, food and many other fields. In recent years, with the rapid development of the Internet of Things (IoT), applications of gas sensors in the emerging smart home, wearable devices, and intelligent mobile terminals have surged forward, significantly expanding the application space, and the demands have changed by orders of magnitude. These demands require the gas sensors to develop in the forms of miniaturization, intelligence and multifunction. The successful application of new material preparation technologies in nanostructures and thin films provides conditions for the realization of new functions of gas sensors. Using MEMS technology to help realize the miniaturization of the sensor size, and then to study the integration of multi-gas sensors to achieve multi-functionality, and the integration of gas sensors with digital circuits and algorithms will become an inevitable way to realize intelligence. Miniaturized and intelligent gas sensors will become a new highlight to activate the market. Among the numerous types of gas sensors, polymer and metal oxide-based gas sensors are considered as the promising candidates. Although polymer-based sensors have lots of advantages, such as low cost, tailor for target molecule, and low energy consuming. However, long-term robustness is a critical issue for polymer-based sensors which has constricted their commercial value in practical application. When it comes to metal oxide-based sensors, they also have advantages like simple structure,

low price, quick response and high sensitivity. But they have the inevitable concern of the interference from ambient gas and temperature.

Addressing on above weaknesses, for understanding the degradation mechanism of polymer-based sensor, a device with the capability to perform both electrical molecular sensing and infrared (IR) spectroscopy was first developed to correlate the degradation of sensing properties with the chemical state in Polyethylene Glycol-Carbon black (PEG-CB) nanocomposite sensor. By comparing the sensing properties and the IR spectroscopy on a same device, it was found that the oxidation of PEG was a key factor for the degradation of sensing performance. Depending on the mechanism, an anti-oxidizing agent (i.e. ascorbic acid) was incorporated into the PEG-CB nanocomposite sensor to inhibit the PEG oxidation and successfully proved its long-term stability in ambient air for 30 days. Second, we investigated the molecule-to-surface interaction on metal oxide, aiming at increasing the selectivity to target molecule based on the understanding. We prepared three nanowire array structures including ZnO nanowires, ZnO/ZrO_2 core/shell nanowires and ZnO/TiO_2 core/shell nanowires for investigating the material dependence on the molecular adsorption behaviors. The well-spaced nanowires and the well-defined surface area of nanowire array structure allowed us to fairly characterize the molecule-to-surface interaction with different material species while suppressing the steric hinderance of molecular diffusion. Spectroscopic and spectrometric analyses revealed that the Lewis acidity of meal cations gave a strong impact on the bonding strength of molecules but not on the adsorption amount. In addition, we proposed an edge-less seed layer structure using two-layers resist method to define the growth direction for in-situ fabrication of hydrothermally grown ZnO bridging nanosensors. This well-defined bridging nanostructures not only substantially suppressed the unintentional variations of electrical resistances between electrodes,

but also significantly enhance the sensing responses for NO_2 with the smaller standard deviation and the lower limitation of detection compared with those using conventional shape edge seed layers. Furthermore, we demonstrated a discriminative molecular sensing in mixture using a difference of reactivity in adsorbed molecules on metal oxide nanowire surface. Sol-gel ZrO_2 coated nanowires exhibited distinct selectivity for collecting 2-nonanone (C9 ketone) in mixture containing chemically similar nonanal (C9 aldehyde), which was not available in sputter ZrO_2 coated nanowires. IR spectroscopy and x-ray photoemission spectroscopy (XPS) indicated that such selectivity in sol-gel ZrO_2 coated nanowires was caused by the difference of oxidation stability in adsorbed species. Aldehyde i.e. nonanal was easily oxidated by activated oxygen on sol-gel ZrO_2 surface while ketone i.e. 2-nonanone with higher resistivity for oxidation remains on the surface. Meanwhile, this ketone sensing surface showed the excellent thermally robustness for keeping its selectivity at 400 ^oC for near 3×10^7 years. These results have overcome the robustness bottleneck for polymer sensors and enhanced the selectivity and robustness for metal oxide sensors with the understanding of chemical reaction on polymer and metal oxide.

We believe that based on these findings such as rational mechanism of molecule-to-surface reaction, people will have a deeper understanding of the underlying molecular sensing mechanism. In addition, with an in-depth understanding of the sensing mechanism, the next generation of chemical detection technology innovation will come in the foreseeable future.

CONTENTS

CHAPTER I

GENERAL INTRODUCTION

1.1 Introduction

1.1.1 Why are Chemical Sensors so Important in Modern Society?

In modern society, the development of science and the adoption of advanced technologies have led to extremely rapid industrial development, while greatly improving people's living. However, with this comes a great deal of damage and pollution to the environment. Of which, air pollution, an issue that is closely related to us, is becoming increasingly serious. The harmful gas molecules produced by human activities, together with the atmosphere from nature, fill our living world. Certainly, air pollution is not only a problem that caused by human overexploitation of nature and a deficiency of awareness, but also influenced by the spontaneous behaviors of nature. For example, volcanic eruption, forest fires and radioactive decay of rocks also release gases that can lead to air pollution. Both human-made air pollution and natural air pollution can greatly affect people and the planet. The most significant issue with air pollution is its impact on human health, agriculture and many other fields that are related to humans. As one of the world's biggest killer, quote World Health Organization (WHO), the environment (outdoor air pollution) in urban and rural areas contributed to 4.2 million premature deaths worldwide in 2016. At the same time, indoor air pollution also causes serious health risk for over 2 million people. 99% of the world's population lives in places that do not meet WHO air quality guidelines levels in 2019. Hazard and toxic gases are not only directly harmful to the lung and respiratory system, but also can cause serious damage to other organ systems. Numerous serious health problems, such as heart disease, fertility problems, cancers, miscarriage, and stroke are connected to air pollution.[1-3] In addition, Volatile organic compounds (VOCs) as the typical gas molecules[4] have been found to be biomarkers for

a number of diseases, since some of them are products of metabolic processes. Therefore, it is important to detect these molecules, not only to prevent us from the hazard environment, but also to be aware of lesions.

Diverse demand for gas molecule detection has accelerated the development of related science and technology. Chemical sensor is an efficient way to help improve our ability to monitor gas molecules in the surrounding environment. The signals from chemical sensor can give direct evidence to help avert possible risks. Meanwhile, chemical sensors can be used various kinds of applications including consumer device, industry 4.0 and medical application (i.e., remote patient monitoring). During the development process, developing sensors with high sensitivity (Sensitivity), high selectivity (Selectivity), high stability (Stability), fast response (Speed), low cost (Cost) are the main objectives. With the development of Internet of Things (IoT), micro and nano processing technology and artificial intelligence technology, artificial olfaction technology built by gas sensor array (simulating the olfactory receptors in biological olfaction) and artificial intelligence algorithm (simulating the olfactory nervous system in biological olfaction) is playing an important role in many fields, helping to realize the development route of gas sensors from "functional implementation" to "performance enhancement" to "intelligence". Actively exploring new principles, new materials, new mechanisms and new devices for gas sensors has important scientific significance and practical value for comprehensively improving the performance of artificial olfaction, expanding the scope of use of artificial olfaction. Currently, according to Yole Development's analysis report, by 2023, the global gas sensor market will reach $1 billion.[5] Accurate and reliable sensors provide the foundation for engineers to understand the characteristics of applications ranging from industry and daily objects. With large amount of data collected by sensor, more informed decision

can be made, enabling the Internet of Things (IoT). With the innovation for IoT keeping open new horizons for improving the quality of life, sensor technology must keep pace.

1.1.2 Applications of Polymer and Metal Oxide on Chemical Sensor for Molecular Detection

Chemical sensors are sensors that respond when certain chemicals are present, with the response signal, these certain chemicals can be detected. Mechanism of chemical sensors diverse from the physical and chemical feature, and normally depends on the material's reaction, electrical activity, etc. In 2000, A. Heeger, A. MacDiarmid and H. Shirakawa won the Nobel Prize in Chemistry for their work on conducting polymers.[6] Since then, functional polymers have extensive attention and developed rapidly, from basic research to applications in the information field. Therefore, polymers with advantages of low cost, simple fabrication, diversity in structure, easily combine with other inorganic materials, fast response, low energy consumption (sensitive at room temperature) have attracted attention from researcher in sensor field for last two decades. Hong[7] reported a chemical sensor based on layered structure consist of Divinyl styrene polymer and isoprene polymer, which can be applied in environment control of trace organic contaminants due to its high sensitivity. Rösler[8] used hydrophobic polymers to realize the off-line detect of pollutants in drink water with Quartz-crystal-microbalance (QCM). Doleman[9] built a sensing system with an array of conductive polymers (Poly (4-vinyl phenol), poly (N-vinyl pyrrolidone), poly (sulfone), poly (methyl methacrylate), poly (caprolactone), poly (ethylene-co-vinyl acetate), poly (ethylene oxide) polyethylene, poly (vinylidene fluoride), poly (ethylene glycol)), which can automatically realize odor detection. What's more, their work also detected the threshold of human and e-nose with this sensor array. Liu[10] successfully estimated the volume of pethidine hydrochloride and content uniformity in injections and tablets

by using Poly (vinyl chloride), because Pethidine–phosphate tungstate ion can associate with PVC as an electroactive material. Numerous researches and works shown that functional polymers, when suitably modified or synthesized for specific tasks, have proven to have great potential in the innovation of sensor device. The tailored polymers can play a well-define roles in sensors after rational design, whether sensing by themselves or by fixing the substance responsible for sensing the composition of the analyte. Adhikari and Majumdar with their review paper shows that during 1999-2004, the most widely used material in various sensor construction in various applications was polymer.[11] Even though the history of polymer sensors is short, its contribution to widespread applications in sensors is capable to be compared to that of silicon in semiconductor sensors.[12]

When it comes to semiconductor sensors, metal oxides material is currently the most studied gas sensing materials for semiconductor gas sensors. In fact, most commercial gas sensors are metal oxides sensors. Heiland[13], Bielanski[14] and Seiyama[15] reported the discovery that the conductivity of metal oxide semiconductors alters when exposed to gas molecules, in 1954-1962. Those are the initial reports on the phenomenon of the metal oxide-gas molecule reaction effect, while the electrical conductivity change of ZnO film was induced by hydrogen, carbon dioxide, toluene and propane. Then Taguchi took a decisive step by producing a SnO_2 based semiconductor device for monitoring low concentrations of combustible gases[16], bringing metal oxide-based semiconductor sensors into industrial sensors (Taguchi-type sensors). Since then, the field of metal oxide-based gas sensors have been bloomed. With its' advantages of high sensitivity, fast response time, low cost and good reliability, etc., and has become one of the world's most productive and widely used sensors. This type of sensor mainly includes SnO_2, SnO, and Fe_2O_3. Nowadays, many companies are producing and

marketing this type of gas sensors, like Figaro, FIS, MICS, UST, CityTech, etc. [17-23] In addition, many new materials have been developed. For example, single metal oxide materials include WO_3, In_2O_3, TiO_2, BaO_2, CdO, V_2O_5, Al_2O_3, ZrO_2, etc.; there are also mixed metal oxide materials such as Zn_2SnO_4, NiCuO, $AlVO_4$, $CdSnO_3$, Na_2SO_4 - $In2O_3$, ZnO-CuO, CdO-SnO_2, SnO_2-TiO_2-$In2O_3$, etc.[24-32] The applications ranged from explosive gases or toxic gases alarms to car intake air control to components in complex chemical sensor systems.[33-34]

At present, the study of sensitive materials is the main research direction of gas sensors and a popular research direction because the properties of sensitive materials determine their main performance. The main research direction is to develop nano-gas sensitive materials with low working temperature, high sensitivity and high selectivity. In recent decades, the development of nanotechnology has greatly facilitated the application of materials with sizes in the nanoscale range in gas sensors. These nanostructures have a high surface area to volume ratio and thus provide sensors with higher sensitivity and reliability than conventional sensor devices. Meanwhile, with the development of micro- and nano-fabrication technologies, silicon-based micro-thermal plates developed with advanced MEMS (Micro-Electro-Mechanical Systems), NEMS (Nano-Electro-Mechanical Systems) or EBL (Electron Beam Lithography) technologies are gradually replacing ceramic plates, and the size of sensors is shrinking from centimeter to nanometer scale, further reducing the size and power consumption of sensors.

1.1.3 Problems in Polymer and Metal Oxide-Based Sensors

Research and development of conductivity polymer and metal oxide-based sensors has led to a number of publications that primarily report excellent gas sensing results

obtained by measuring electrical signals in a laboratory environment far from the characteristics of realistic operating conditions.[7-15] Polymers are known to be one of the most suitable materials for general purpose sensors, mainly because of their physical and chemical properties, it is easy for them to be modified for specific tasks, easy miniaturization and low cost manufacturing. A major disadvantage (polymer nanomaterials as a whole) is that they are not as stable as their bulk counterparts. The change in structure led to degradation of sensing performance. Such as, polymer−carbon nanocomposite sensors often suffer from degradation of sensing performance in an air environment. On the other hand, metal oxide sensor has advantages of low cost, simple manufacturing, high sensitivity, long term stability and simple circuit. The disadvantage is that it must work at high temperatures, has poor gas selectivity, unsatisfactory stability at high temperature, and high energy requirements. During long-term use at high temperatures, contamination of the surrounding environment and re-growth of grain boundaries often lead to degradation of sensing performance, which prevents us from collecting accurate molecular information over time.[35] Above all, further studies from chemical, spectroscopic and structural perspectives are needed to elucidate the mechanisms of molecule to surface interactions for robust and high selective gas sensing.

1.2 Framework of This Thesis

This thesis consists of seven chapters, which are introduced as follows:

- Chapter I is a general introduction of the motivation and structure for the research in this dissertation, including the importance of molecularly detection by chemical sensors, the application of polymer and metal oxide in chemical sensors and their facing problems, the framework for this thesis is also included.

- Chapter II outlines the overview of gas molecular detection technology, including a literature review of conventional method and current strategies for portable sized modern application. Special emphasis is placed on polymer-based sensor and metal oxide nanowires as an important part of robust and selectivity sensor improvement.
- Chapter III presents a study for understanding and controlling the degradation of polyethylene glycol (PEG)-carbon black nanocomposite sensor. With the understanding of degradation mechanism, the sensing performance was successfully kept for long-term cycling, which is of great importance for practical application.
- Chapter IV shows a nanowire array structure with well-spaced nanowires and a clear surface area. It serves as a new platform for studying the interaction of volatile molecules on the surface of nano-scale metal oxides. By changing the types of metal oxides (ZnO, ZrO_2, TiO_2), we successfully revealed the effect of metal cations on the adsorption behavior of ketone compounds.
- Chapter V demonstrate the significant effect of edge-topological regulation on *in-situ* fabrication of hydrothermally grown ZnO bridging nanosensors. We propose an edge-less seed layer structure using two-layers resist methods to define the growth direction for *in-situ* fabrication of bridging nanosensors. Bridging nanosensors fabricated using such edge-less seed layer structures exhibited much superior directional controllability for *in-situ* fabrication.
- Chapter VI reports a discriminative molecular sensing of ketone in mixture by a nanowire selector-integrated hybrid sensor device. This strategy of using the difference in reactivity between adsorbed molecules and molecular recognition surface breaks through the limitation of molecular sensing for electrically

discriminating the chemically similar molecules in mixture. In addition, this ketone sensing surface is extremely thermally robust by using ZrO_2 coated on to nanowires.

- Chapter VII finally gives an overall conclusion of this thesis and the perspective for possible future work.

1.3 References

(1) Kelly F J, Fussell J C. Air pollution and public health: emerging hazards and improved understanding of risk[J]. Environmental geochemistry and health, 2015, 37(4): 631-649.

(2) Pope III C A, Dockery D W. Health effects of fine particulate air pollution: lines that connect[J]. Journal of the air & waste management association, 2006, 56(6): 709-742.

(3) Farmer S A, Nelin T D, Falvo M J, et al. Ambient and household air pollution: complex triggers of disease[J]. American Journal of Physiology-Heart and Circulatory Physiology, 2014, 307(4): H467-H476.

(4) ToxTown, US National Library of Medicine, May 31, 2017.

(5) http://www.yole.fr/2018_press_releases.aspx

(6) Shirakawa H, Louis E J, MacDiarmid A G, et al. Synthesis of electrically conducting organic polymers: halogen derivatives of polyacetylene,(CH) x[J]. Journal of the Chemical Society, Chemical Communications, 1977 (16): 578-580.

(7) Ji H-S, McNiven S, Yano K, Ikebukuro K, Bornscheuer UT, Schmid RD, Karube I. Highly sensitive trilayer piezoelectric odor sensor. Anal Chim Acta 1999;387:39–45.

(8) Rösler S, Lucklum R, Borngra¨ber R, Hartmann J, HauptmannP. Sensor system for the detection of organic pollutants in water by thickness shear mode resonators. Sensors Actuators B 1998;48:415–24.

(9) Doleman BJ, Lewis NS. Comparison of odor detection thresholds and odor discriminabilities of a conducting polymer composite electronic nose vs mamallian olfaction. Sensors Actuators B 2001;72:41–50.

(10) Liu ZH, Wen ML, Yao Y, Xiong J. Plastic pethidine hydrochloride membrane sensor and its pharmaceutical applications. Sensors Actuators B 2001;77:219–23.

(11) B. Adhikari, S. Majumdar, Polymers in sensor applications, Prog. Polym. Sci. 29(2004) 699–766.

(12) Harsányi, Gábor. "Polymer films in sensor applications: a review of present uses and future possibilities." Sensor Review (2000).]

(13) Heiland G. Zum Einfluß von adsorbiertem Sauerstoff auf die elektrische Leitfähigkeit von Zinkoxydkristallen[J]. Zeitschrift für Physik, 1954, 138(3-4): 459-464.

(14) Bielański A, Dereń J, Haber J. Electric conductivity and catalytic activity of semiconducting oxide catalysts[J]. Nature, 1957, 179(4561): 668-669.

(15) Seiyama T, Kato A, Fujiishi K, et al. A new detector for gaseous components using semiconductive thin films[J]. Analytical Chemistry, 1962, 34(11): 1502-1503.

(16) N. Taguchi, U.S. Patent 3,631,436 (1971).

(17) www.figaro.co.jp/en/

(18) www.fisinc.co.jp/en/

(19) sgx.cdistore.com

(20) www.ustsensor.com

(21) www.citytech.com

(22) www.appliedsensortech.com

(23) www.newcosmos-global.com

(24) Gali, P.; Sapkota, G.; Syllaios, A. J.; Littler, C.; Philipose, U. Nanotechnology 2013, 24, 225704.

(25) Liu, X.; Chang, Z.; Luo, L.; Lei, X.; Liu, J.; Sun, X. J. Mater. Chem. 2012, 22, 7232.

(26) Wang, C.; Cui, X.; Liu, J.; Zhou, X.; Cheng, X.; Sun, P.; Hu, X.; Li, X.; Zheng, J.; Lu, G. ACS Sens. 2016, 1, 131-136.

(27) Dou, Z.; Cao, C.; Chen, Y.; Song, W. Chem. Commun. 2014, 50, 14889.

(28) Zhang, F.; Zhu, A.; Luo, Y.; Tian, Y.; Yang, J.; Qin, Y. J. Phys. Chem. C 2010, 114, 19214-19219.

(29) Zhou, X.; Li, X.; Sun, H.; Sun, P.; Liang, X.; Liu, F.; Hu, X.; Lu, G. ACS Appl. Mater. Interfaces 2015, 7, 15414-15421.

(30) Zhou X.; Feng, W.; Wang, C.; Hu, X.; Li, X.; Sun, P.; Shimanoe, K.; Yamazoe, N.; Lu, G. J. Mater. Chem. A 2014, 2, 17683-17690.

(31) Yang, X.; Zhang, S.; Yu, Q.; Sun, P.; Liu, F.; Lu, H.; Yan, X.; Zhou, X.; Liang, X.; Gao, Y.; Lu, G. Sens. Actuators B Chem. 2018, 270, 538-544.

(32) Yang, X.; Gao, H.; Zhao, L.; Wang, T.; Sun, P.; Liu, F.; Lu, G. Sens. Actuators B Chem. 2018, 266, 302-310.

(33) Hesse J, Gardner J W, Göpel W. Sensors for automotive technology[M]. Weinheim: Wiley-VCH Verlag, 2003.

(34) T.C. Pearce, S.S. Schiffman, H. Troy Nagle, J.W. Gardner. Handbook of machine olfaction: electronic nose technology[M]. John Wiley & Sons, 2006.

(35) Rüffer, D.; Hoehne, F.; Bühler, J. Sensors 2018, 18, 1052.

CHAPTER II

LITERATURE REVIEW

2.1 Introduction

As we stated in Chapter 1, this thesis focuses on some current issues regarding gas molecule detection using polymer-based sensors and metal oxide-based gas sensors. A comprehensive review of the current situation is necessary to gain a deep understanding of the purpose and significance of this work. In this chapter, we first review the classification of gas molecule detection technologies, including large-scale laboratory instruments such as GC/MS, optical spectroscopy, and other small gas sensors. Then, we narrow down the field into polymer sensor and metal oxide sensor device.

2.2 Various methods for volatile molecules detection

2.2.1 Conventional Instruments

In this section, analytical or detection techniques based on the bulk instruments for the gas molecules are described. These instruments mainly include gas chromatographs, mass spectrometers, optical spectrometers and some techniques that combine several technologies. They are mostly on laboratory instruments, which are long and costly. However, they can give good identification results and are widely used as analytical standards in many fields.[1]

Gas chromatograph (GC) is a method that combines the characteristics of gas chromatography and mass spectrometry to identify different substances in a specimen for analysis.[2] The GC unit consists of three main components: the injection port, the column and the detector. The inlet is a device that introduces the sample into a continuous stream of carrier gas. Nowadays, automatic sample feeders are mostly used to introduce the sample into the inlet automatically. The sample passes from the syringe

through the septum into a heated chamber, where the heat causes the sample and the sample matrix to evaporate, and the carrier gas then purges all (non-split mode) or part (split mode) of the evaporated sample into the column. In the split mode, most of the mixture of sample and carrier gas is evacuated through the split outlet. When the analyte in the sample contains a high analytical concentration (>0.1%), a split injection is appropriate, while for trace analysis with only a small amount of analyte (<0.01%), a non-split injection is preferred.

There are two main types of chromatographic columns (packed columns and capillary columns), and capillary columns are more often used because of their small inner diameter and high separation efficiency. When a multi-component mixed sample enters the column, each component runs through the column at a different rate due to the different adsorption forces of the adsorbents in the column on each component. The component with the weakest adsorption is easily desorbed and leaves the column first to enter the detector, while the component with the strongest adsorption is the least likely to be desorbed and therefore leaves the column last. In this way, the components are separated from each other in the column and are detected and recorded sequentially in the detector. [3]

There are a variety of detectors that can be utilized in gas chromatography, the most widely used being the flame ionization detector (FID) [4,5] and the thermal conductivity detector (TCD) [6]. These two detectors are very powerful, which are sensitive to kinds of analytes and can determine a broad range of concentrations but cannot be utilized to detect water molecule. Meanwhile, the TCD detection is non-destructive, thus it can be tandemly connected with the destructive FID (before the FID) to present the complementary analyses of the analyte. Mass spectrometry is a method that first ionizes a substance, identifies ions depending on their mass-to-charge (m/z) ratio, and then

measures the intensity of different ion spectral peaks to gain the purpose of analysis. [7, 8] It consists of three parts, ionizer, mass analyzer and detector. The general mechanism is to ionize the components of sample in the ionizer. It will produce the positively charged ions with different charge-to-quality ratios, which will be accelerated via the electric field to produce an ion beam that enter the mass analyzer. In the mass analyzer, the ions with different charge to mass ratios are separated in space or time by electric or magnetic fields, or they are focused to the detector by means of filtration to obtain mass spectra, thus obtaining mass and concentration (or partial pressure) related spectra.

Optical spectroscopy is a technique for recognizing substances and determining their chemical composition and relative content based on the spectra of substances. FT-IR and UV-vis spectroscopy are now widely used to identify a wide variety of organic compounds. IR spectroscopy is an instrument that uses the absorption characteristics of substances to infrared radiation of different wavelengths to analyze molecular structure and chemical composition. An infrared spectrometer normally consists of light source, monochromator, detector and processing system. Depending on the spectroscopic system, it can be divided into dispersive and interferometric types. IR spectrum can be categorized into near-infrared, mid-infrared and far-infrared light depending on its relationship with the visible spectrum. [9-13] Far-infrared light (about 400-10 cm^{-1}) is adjacent to microwaves, has low energy and can be used in rotational spectroscopy. Mid-infrared light (about 4000-400 cm^{-1}) can be utilized to explore the fundamental vibrations and related rotational-vibration structures. Higher energy near-infrared light (14000-4000 cm^{-1}) can excite overtone and harmonic vibrations. IR spectroscopy works on the principle that chemical bonds have different frequencies due to different vibrational energy levels. The resonance frequency or vibrational frequency depends

on the shape of the molecular equipotential surface, the atomic mass, and ultimately the associated vibrational coupling.[14,15]

UV spectrum is the absorption spectrum generated by the leap of electrons when the molecules of a substance absorb the electromagnetic waves in the UV-VIS region. [16,17] Usually, the wavelength range of UV spectrum is mainly from 200 to 800 nm (among which 10-200 nm is the vacuum UV region, and its spectrum is less studied because of the strong absorption of electromagnetic waves in the far UV region by air).[18] Since the molecules of different substances have different compositions and structures, their characteristic energy levels are also different, and their energy level differences are different, and each substance can only absorb light radiation with their molecular internal energy level differences, so the absorption of different wavelengths of light by different substances is selective. It is usually only an auxiliary analytical tool, and other analytical methods, such as IR, NMR, EPR and other integrated techniques, are needed to analyze for obtain accurate data.[19,20]

Due to their complex configuration and operation, these above systems are very rare in daily applications. [20-24]

2.2.2 Portable Chemical Sensor

Portable gas detection technology can be used for hazardous gas detection, organic VOC gas detection, combustible gas detection, single gas detection. Accurately make early warning hidden danger detection technology development day by day, in the accident precursor inspection, elimination of the application is more and more extensive, its development direction is miniaturization and automation, in order to achieve long-term monitoring. They can be classified into (1) Electrochemical gas sensor, (2) Catalytic combustion gas sensor, (3) Infrared sensor, and (4) PID photonic sensor.[22-24] Among them, Electrochemical sensor is a sensor based on the electrochemical

properties of the analyte and converts the chemical quantity of the analyte into an electrical quantity for sensing and detection. [25] The earliest electrochemical sensors date back to the 1950s, when electrochemical sensors were used for oxygen monitoring. By the 1980s, electrochemical sensors began to be used to monitor a variety of toxic gas, showed good sensitivity and selectivity. [26-28] Chemical sensor should meet the following requirements: (1) stability--means the stability of the sensor response during the entire operating time. In ideal case, the annual zero drift of the sensor is less than 10% under continuous operating conditions, (2) Sensitivity-- the ratio of the amount of change in the sensor output to the amount of change in the measured input and is largely dependent on the technology used in the sensor construction, (3) Selectivity--also referred to as cross-sensitivity. [29-30] It can be defined by measuring the sensor response generated via a certain concentration of an interfering gas. This characteristic is critical in applications where multiple gases are tracked since cross-sensitivity reduces the repeatability and reliability of the measurement. Therefore, the ideal sensor should have high sensitivity and high selectivity.

The basic characteristics of gas sensors, i.e. sensitivity, selectivity as well as stability, are determined mainly by the choice of materials. The selection of appropriate materials and the development of new materials optimize the sensitive characteristics of gas sensors.

2.3 polymer sensors

Polymer is an indispensable part of the modern sensor equipment. It performs an invaluable role in medicine, chemical reaction control and gas recognition, and can even be used as e-noses or e-tongues. [31-33] Many real-time applications are given in various kinds of polymer-based sensors. However, research on this subject is still in

progress. New approaches are being sought, and the mechanisms of the specific reactions taking place in polymer-based sensors are not entirely understood. To achieve in-depth analysis of polymer sensor still requires lots of efforts.

2.3.1 Carbon-Polymer Sensors

Polymer-carbon black composite is a new type of chemical detection sensor for electronic nose. [34-36] These composite materials are obtained via blending carbon black and polymer in a suitable solvent. The mixture is coated on the substrate between the two metal electrodes. After the solvent evaporates, a composite film is left. These chemical resistor arrays are made of polymers and carbon black with different chemical properties, which expand reversibly and cause resistance changes when exposed to chemical vapors.

Carbon materials have high carrier mobility, good mechanical properties, stable physicochemical properties, and good room-temperature conductivity, which can compensate for the shortcomings of traditional metal-oxide-semiconductor sensing materials. The non-covalent modification of carbon-based materials with organic molecules can modulate the electron transport ability of polymer materials, improve the recognition and adsorption ability of detected gases, and obtain high sensing characteristics. The polymer carbon black sensor is sensitive to various vapors ranging from ppb to ppm.[37-40] Their sensitivity relies on the analyte and the polymer. The response of the sensor is inversely proportional to the vapor pressure of the analyte. Low vapor pressure (larger molecular weight) compounds can usually be detected at very low levels (ppb), while compounds with very high vapor pressures can also be detected at high ppm levels (Doleman et al., 1998).[41] This trend is due to the vapor distribution coefficient between the solid phase of the sensor and the gas phase in the

area above the sensor. Low vapor pressure materials are more likely to be present in the polymer, resulting in a lower detection threshold.[42]

2.4 Metal-Oxide Nanowire based sensor devices

Metal oxides are semiconductor materials and can be classified into n-type and p-type according to the carrier type.[43] Metal oxides alone are widely used for detecting various gaseous species, including volatile gases like ethanol, methanol, acetone, and inorganic gases (carbon monoxide, hydrogen sulfide, and nitric oxide), due to their excellent gas-sensitive properties.[44-48] Metal oxides are widely used in various gas sensors due to their non-toxicity, low cost, and small size of the sensor components. Metal oxide semiconductor sensitive materials rely mainly on the occurrence of physical-chemical adsorption between the surface defects of the semiconductor and the target gas, which causes the bending of the semiconductor energy band and leads to changes in the electrical parameters of the semiconductor. According to this principle, the higher the density of surface states and the more active sites of a semiconductor sensitive material, the stronger the adsorption capacity of the sensing target molecule, and thus the better the sensitivity, response recovery and other characteristics of the sensor. Improving the adsorption function of the surface of sensitive materials, improving the conduction rate of electrons on the material surface and increasing the efficiency of the material surface utilization are effective ways to improve the gas sensing performance. By structuring the surface (boundary) of the material, such as porosity, low dimensionality, and layering, the specific surface area of the material can be effectively increased.[49-52] Nanotechnology is used to chemically modify electrodes, change the electrode surface structure, control the electrochemical process, and achieve functional modification and modulation of electrochemical sensors at the molecular

level. The electrodes are chemically modified with new nano-functional materials (including carbon-based materials such as graphene, carbon nanotubes and mesoporous carbon; semiconductor metal oxides such as TiO_2 and SnO_2; precious metals such as Au, Ag, Pd and Pt; and conductive polymers such as polyaniline and polypyrrole) to achieve the detection of toxic and hazardous gases, heavy metal ions and organic pollutants in the environment.

2..4.1 Integrated Nanowires Sensor

Afzali et al[53] obtained ZnO-reduced graphene composites by dispersing graphene oxide on the surface of pre-prepared ZnO nanowires and using the photocatalytic properties of ZnO to reduce the graphene oxide after UV light irradiation. Afzali et al [71] investigated the sensing properties of the composites towards oxygen. The results showed that the composite exhibited opposite semiconductor behavior to that of ZnO alone in sensing, where the composite exhibited p-type semiconductor behavior while ZnO alone exhibited the opposite n-type semiconductor behavior. It is also found that the composite material can respond to O_2 at room temperature but has a long recovery time. By increasing the temperature (200°C), the recovery time of the composite material decreases significantly and the sensitivity is greatly improved, which is about twice as much as that at room temperature.

Early metal oxide semiconductor sensors sensitive layer mostly used a thick film composed of micron particles, given that semiconductor sensors are based on the charge interaction between the gas molecules adsorbed on the sensor surface and the oxide surface to detect gas molecules,[54] early micron particle thick film sensors in the sensitivity and detection limits and other aspects of performance are not high, power consumption is also in the wattage range, cannot meet the trace pollution molecules in

the environment in real time, the long-time monitoring of trace pollution molecules in the environment. The development of nanoscience and technology has provided a great impetus to the development of oxide semiconductor sensors. Compared with oxide bulk materials, the increase in specific surface area of nanomaterials leads to more surface suspension bonds and surface defects, which provide more sites for chemical and physical interactions between gas molecules on the sensor surface and enhance the charge exchange between gas molecules and oxide semiconductor sensors. [55-57] Among them, the oxide nanowires have a unique quasi-one-dimensional geometric configuration with the advantages of both large specific surface area and single-crystal carrier transport channels, making them one of the ideal units for building next-generation ultra-micro/ultra-low-power gas sensors. [58]

2..4.2 Nanowires Array Sensor

Nanowire array-based gas sensors show multitudinous device structures based on a variety of processing technologies and design schemes. Among metal oxide nanowire sensors, single nanowire sensors have good stability, high sensitivity in a suspended device configuration, and low self-heating power consumption, but the device process is complex and the yield is low.[59] Many indirect methods can achieve self-assembly of metal oxide nanowires on a substrate covered with an underlying electrode, such as contact printing[60], Langmuir-Blodgett technique[61], microfluidic channeling[62], bubbling method[63], etc. However, the liquid-phase method of self-assembly suffers from easy contamination, weak adhesion, weak electrical contact[64] and difficulty in obtaining a suspension device. In contrast, metal oxide nanowires grown directly on a substrate with an underlying electrode by the vapor-phase method have stable electrical contact with the underlying electrode[65], which can not only overcome the bottleneck of complex preparation process and low yield of single suspended nanowire sensors, but

also the nanowires are exposed to the gas to be measured and achieve ultra-low power consumption by self-heating[66], which can give full play to the nanowire in the highly integrated, highly sensitive, and low-power potential in the field of sensing.

2.5 Summary of Literature Review

In this chapter, the literatures on gas molecular detection via various methods (GC/MS, FT-IR, UV-VIS, polymer sensor and metal oxide sensor) are reviewed. Bulky and expensive GC/MS, FT-IR and UV-VIS instruments can undoubtedly provide accurate analysis of chemical substances, but they cannot be utilized in people's daily life. Portable gas sensor is a promising way to realize the real-time detection of chemical molecules. In this chapter, polymer-based gas sensor and metal oxide sensor were mainly discussed. With advantages such as good sensitivity, fast response, scaling, polymer-based sensor was considered as a promising candidate for molecular detection. Metal oxide sensor is one of the most widely used commercial sensors. The sensing mechanism of polymer sensor and metal oxide sensor are simply discussed. However, both of polymer-based sensor and metal oxide sensor have their disadvantages.

Subsequently, problems of polymer sensor and metal oxide sensor are discussed. For polymer sensor, the long-term robustness is a crucial issue. Unlike polymer sensor, metal oxide sensor has good robustness, but the selectivity is a bottle-neck problem. It is difficult to overcome these issues with lack of understanding of the molecule-to-surface interaction. Choosing suitable polymer for polymer sensor is one of the effective ways to enhance the sensing performance. With advanced fabrication and deposition techniques on nanomaterials, integrated metal oxide sensor with nanowire array can be developed to meet various requirements.

2.6 References

(1) Pavia, D. L.; Lampman, G. M.; Kritz, G. S.; Engel, R. G. Introduction to Organic Laboratory Techniques (4th Ed.). Thomson Brooks/Cole., 2006.

(2) Hites, R. A. Anal. Chem. 2016, 88, 6955-6961.

(3) Abraham, M. H.; Poole, C. F.; Poole, S. K. J. Chromatogr. A 1999, 842, 79-114.

(4) https://www.chromedia.org/dchro/gfx/ZapdlvkHC.jpeg

(5) McWILLIAM, I. G.; DEWAR, R. A. Nature 1958, 181, 760.

(6) Grob, R. L.; Barry, E. F. Modern Practice of Gas Chromatography (4th Ed.). John Wiley & Sons., 2004.

(7) De Hoffmann, E.; Stroobant, V. Mass Spectrometry: Principles and Applications, 3rd ed.; John Wiley & Sons: Chichester, 2011.

(8) Gross, J. H. Mass Spectrometry: A Textbook, 2nd ed.; Springer: Heidelberg, Germany, 2011.

(9) Cooper J B, Wise K L, Welch W T, et al. Determination of weight percent oxygen in commercial gasoline: a comparison between FT-Raman, FT-IR, and dispersive near-IR spectroscopies[J]. Applied spectroscopy, 1996, 50(7): 917-921.

(10) Kim Y, Rose C A, Liu Y, et al. Ft-IR and near-infared FT-Raman studies of the secondary structure of insulinotropin in the solid state: α-helix to β-sheet conversion induced by phenol and/or by high shear force[J]. Journal of pharmaceutical sciences, 1994, 83(8): 1175-1180.

(11) Langkilde F W, Svantesson A. Identification of celluloses with Fourier-transform (FT) mid-infrared, FT-Raman and near-infrared spectrometry[J]. Journal of pharmaceutical and biomedical analysis, 1995, 13(4-5): 409-414.

(12) Bellamy M K, Mortensen A N, Hammaker R M, et al. Chemical mapping in the mid-and near-IR spectral regions by Hadamard transform/FT-IR spectrometry[J]. Applied spectroscopy, 1997, 51(4): 477-486.

(13) Shumin H, Ronghua Z, Xuetong Z. A Study of Near-and Super-Critical Fluids Using Diamond Anvil Cell and in-Situ FT-IR Spectroscopy[J]. Acta Geologica Sinica-English Edition, 2000, 74(2): 412-417.

(14) Akagi, S. K.; Burling, I. R.; Mendoza, A.; Johnson, T. J.; Cameron, M.; Griffith, D. W. T.; Paton-Walsh, C.; Weise, D. R.; Reardon, J.; Yokelson, R. J. Atmos. Chem. Phys. 2014, 14, 199.

(15) Hung, H.-M.; Chen, Y.-Q.; Martin, S. T. J. Phys. Chem. A 2012, 117, 108.

(16) Perkampus H H. UV-VIS Spectroscopy and its Applications[M]. Springer Science & Business Media, 2013.

(17) Klamt A. Calculation of UV/Vis spectra in solution[J]. The Journal of Physical Chemistry, 1996, 100(9): 3349-3353.

(18) Rahman A, Yalin A P, Surla V, et al. Absolute UV and VUV emission in the 110–400 nm region from 13.56 MHz driven hollow slot microplasmas operating in open air[J]. Plasma Sources Science and Technology, 2004, 13(3): 537.

(19) Hills, A. J.; Zimmerman, P. R. Anal. Chem. 1990, 62, 1055.

(20) Kourtidis, K.; Ziomas, I.; Zerefos, C.; Achilleas, G.; Balis, D.; Tzoumaka, P. Atmos. Environ. 2000, 34, 1471.

(21) Bornhop, D. J.; Wangsgaard, J. G. J. High Resolution Chroma. 1991, 14, 344-347.

(22) Noziere, B.; Kalberer, M.; Claeys, M.; Allan, J.; D'Anna, B.; Decesari, S.; Finessi, E.; Glasius, M.; Grgic, I.; Hamilton, J. F.; Hoffmann, T.; Iinuma, Y.; Jaoui, M.; Kahnt, A.; Kampf, C. J.; Kourtchev, I.; Maenhaut, W.; Marsden, N.; Saarikoski, S.; Schnelle-Kreis, J.; Surratt, J. D.; Szidat, S.; Szmigielski, R.; Wisthaler, A. Chem. Rev. 2015, 115, 3919-3983.

(23) Meng, Z.; Stolz, R. M.; Mendecki, L.; Mirica, K. A. Chem. Rev. 2019, 119, 478-598.

(24) Banica, F. G. Chemical Sensors and Biosensors: Fundamentals and Applications; 2012.

(25) Sekhar, P. K.; Brosha, E. L.; Mukundan, R.; Gaezon, F. Electrochem. Soc. Interface 2010, 19, 5-40.

(26) Electrochemical sensors, biosensors and their biomedical applications[M]. Academic Press, 2011.

(27) Hahn C E W. Tutorial Review. Electrochemical analysis of clinicalblood-gases, gases and vapours[J]. Analyst, 1998, 123(6): 57R-86R.

(28) Valdés M G, González A C V, Calzón J A G, et al. Analytical nanotechnology for food analysis[J]. Microchimica Acta, 2009, 166(1): 1-19.

(29) Wong H S, White M H. A CMOS-integrated'ISFET-operational amplifier'chemical sensor employing differential sensing[J]. IEEE Transactions on Electron Devices, 1989, 36(3): 479-487.

(30) Albert K J, Lewis N S, Schauer C L, et al. Cross-reactive chemical sensor arrays[J]. Chemical reviews, 2000, 100(7): 2595-2626.

(31) Wang, T.; Yu, Q.; Zhang, S.; Kou, X.; Sun, P.; Lu, G. Nanoscale 2018, 10, 4841-4851.

(32) Zhu, Y.; Zhao, Y.; Ma, J.; Cheng, X.; Xie, J.; Xu, P.; Liu, H.; Liu, H.; Zhang, H.; Wu, M.; Elzatahry, A. A.; Alghamdi, A.; Deng, Y.; Zhao, D. J. Am. Chem. Soc. 2017, 139, 10365-10373.

(33) Patolsky, F.; Lieber, C. M. Mater. Today 2005, 8, 20-28.

(34) Munoz B C, Steinthal G, Sunshine S. Conductive polymer-carbon black composites-based sensor arrays for use in an electronic nose[J]. Sensor Review, 1999.

(35) Shevade A V, Ryan M A, Homer M L, et al. Molecular modeling of polymer composite–analyte interactions in electronic nose sensors[J]. Sensors and Actuators B: Chemical, 2003, 93(1-3): 84-91.

(36) Lewis N S. Comparisons between mammalian and artificial olfaction based on arrays of carbon black− polymer composite vapor detectors[J]. Accounts of chemical research, 2004, 37(9): 663-672.

(37) Lonergan M C, Severin E J, Doleman B J, et al. Array-based vapor sensing using chemically sensitive, carbon black− polymer resistors[J]. Chemistry of Materials, 1996, 8(9): 2298-2312.

(38) Lei H, Pitt W G, McGrath L K, et al. Modeling carbon black/polymer composite sensors[J]. Sensors and Actuators B: Chemical, 2007, 125(2): 396-407.

(39) Chen S G, Hu J W, Zhang M Q, et al. Gas sensitivity of carbon black/waterborne polyurethane composites[J]. Carbon, 2004, 42(3): 645-651.

(40) Gao T, Woodka M D, Brunschwig B S, et al. Chemiresistors for array-based vapor sensing using composites of carbon black with low volatility organic molecules[J]. Chemistry of materials, 2006, 18(22): 5193-5202.

(41) Doleman B J, Lonergan M C, Severin E J, et al. Quantitative study of the resolving power of arrays of carbon black− polymer composites in various vapor-sensing tasks[J]. Analytical Chemistry, 1998, 70(19): 4177-4190.

(42) Pejcic B, Eadington P, Ross A. Environmental monitoring of hydrocarbons: A chemical sensor perspective[J]. Environmental science & technology, 2007, 41(18): 6333-6342.

(43) Shankar P, Rayappan J B B. Gas sensing mechanism of metal oxides: The role of ambient atmosphere, type of semiconductor and gases-A review[J]. Sci. Lett. J, 2015, 4(4): 126.

(44) Tiemann M. Porous metal oxides as gas sensors[J]. Chemistry–A European Journal, 2007, 13(30): 8376-8388.

(45) Yamaura H, Tamaki J, Moriya K, et al. Selective CO Detection by Using Indium Oxide-Based Semiconductor Gas Sensor[J]. Journal of the Electrochemical Society, 1996, 143(2): L36.

(46) Basu S, Basu P K. Nanocrystalline metal oxides for methane sensors: role of noble metals[J]. Journal of Sensors, 2009, 2009.

(47) Sun C, Maduraiveeran G, Dutta P. Nitric oxide sensors using combination of p- and n-type semiconducting oxides and its application for detecting NO in human breath[J]. Sensors and Actuators B: Chemical, 2013, 186: 117-125.

(48) Khanna A, Kumar R, Bhatti S S. CuO-doped SnO 2 thin films as hydrogen sulfide gas sensor[J]. Applied physics letters, 2003, 82(24): 4388-4390.

(49) Mishra S, Ghanshyam C, Ram N, et al. Detection mechanism of metal oxide gas sensor under UV radiation[J]. Sensors and Actuators B: Chemical, 2004, 97(2-3): 387-390.

(50) Wang X, Yee S S, Carey W P. Transition between neck-controlled and grain-boundary-controlled sensitivity of metal-oxide gas sensors[J]. Sensors and Actuators B: Chemical, 1995, 25(1-3): 454-457.

(51) Galdikas A, Martūnas Z, Šetkus A. SnInO-based chlorine gas sensor[J]. Sensors and Actuators B: Chemical, 1992, 7(1-3): 633-636.

(52) Korotcenkov G. Metal oxides for solid-state gas sensors: What determines our choice?[J]. Materials Science and Engineering: B, 2007, 139(1): 1-23.

(53) Afzali P, Abdi Y, Arzi E. Directional reduction of graphene oxide sheets using photocatalytic activity of ZnO nanowires for the fabrication of a highly sensitive oxygen sensor. Sensor Actuat B-Chem, 2014, 195: 92–97.

(54) Qin, Y.; Li, X.; Wang, F.; Hu, M. J. Alloys Compd. 2011, 509 (33), 8401.

(55) Zheng, H.; Ou, J. Z.; Strano, M. S.; Kaner, R. B.; Mitchell, A.; Kalantar-zadeh, K. Adv. Funct. Mater. 2011, 21 (12), 2175.

(56) Dey, A. Mater. Sci. Eng. B 2018, 229, 206.

(57) Shen, Y.; Yamazaki, T.; Liu, Z.; Meng, D.; Kikuta, T.; Nakatani, N. Thin Solid Films 2009, 517 (6), 2069.

(58) Kuang, Q.; Lao, C.; Wang, Z. L.; Xie, Z.; Zheng, L. J. Am. Chem. Soc. 2007, 129 (19), 6070.

(59) Meng, G.; Zhuge, F.; Nagashima, K.; Nakao, A.; Kanai, M.; He, Y.; Boudot, M.; Takahashi, T.; Uchida, K.; Yanagida, T. ACS Sensors 2016, 1 (8), 997.

(60) Takahashi, T.; Nichols, P.; Takei, K.; Ford, A. C.; Jamshidi, A.; Wu, M. C.; Ning, C. Z.; Javey, A. Nanotechnology 2012, 23 (4), 045201.

(61) Zhuang, X.; Ning, C. Z.; Pan, A. Adv. Mater. 2012, 24 (1), 13.

(62) Xiong, X.; Jaberansari, L.; Hahm, M. G.; Busnaina, A.; Jung, Y. J. Small 2007, 3 (12), 2006.

(63) Wu, S.; Huang, K.; Shi, E.; Xu, W.; Fang, Y.; Yang, Y.; Cao, A. ACS Nano 2014, 8 (4), 3522.

(64) Hu, H.; Wang, Z.; Ye, Q.; He, J.; Nie, X.; He, G.; Song, C.; Shang, W.; Wu, J.; Tao, P.; et al. ACS Appl. Mater. Interfaces 2016, 8 (31), 20483.

(65) Nguyen, H.; Quy, C. T.; Hoa, N. D.; Lam, N. T.; Duy, N. V.; Quang, V. V.; Hieu, N. V. Sens. Actuators B 2014, 193, 888.

(66) Hung, C. M.; Le, D. T. T.; Van Hieu, N. J. Sci.: Adv. Mater. Devices 2017, 2 (3), 263.

CHAPTER III

MECHANISTIC APPROACH FOR LONG-TERM STABILITY OF POLYMER-BASED CHEMICAL SENSOR

3.1 Abstract

Polymer−carbon nanocomposite sensor is a promising molecular sensing device for electronic nose (e-nose) due to its printability, variety of polymer materials, and low operation temperature; however, the lack of stability in an air environment has been an inevitable issue. Here, we demonstrate a design concept for realizing long-term stability in a polyethylene glycol (PEG) − carbon black (CB) nanocomposite sensor by understanding the underlying phenomena that cause sensor degradation. Comparison of the sensing properties and infrared spectroscopy on the same device revealed that the oxidation-induced consumption of PEG is a crucial factor for the sensor degradation. According to the mechanism, we introduced an antioxidizing agent (i.e., ascorbic acid) into the PEG − CB nanocomposite sensor to suppress the PEG oxidation and successfully demonstrated the long-term stability of sensing properties under an air environment for 30 days, which had been difficult in conventional polymer−carbon nanocomposite sensors.

KEYWORDS: *Chemiresistive sensor, carbon black, polyethylene glycol, nanocomposite, long-term stability*

3.2 Introduction

Chemiresistive sensors, which transduce volatile molecules in surrounding environments into digital information, have recently gained increasing attention due to their ability to collect and monitor chemical information for various usages, such as environmental monitoring, healthcare, food safety, and qualification of industrial fine products in upcoming Internet of Things (IoT) era.[1–8] Chemiresistive sensors are utilized as components of artificial olfaction system's so-called electronic nose (e-nose), and the molecular sensing data collected through the multi sensor array in e-nose are analyzed based on a pattern recognition technique by mimicking the biological olfaction system.[9,10] The goal in this field is to collect time-series molecular sensing data by using IoT devices and exploit them as chemical big data.[11,12] Therefore, development of a long-term stable and low-energy consumption chemiresistive sensor is a major challenge. Among various chemiresistive sensors, a polymer−carbon nanocomposite-based sensor is a promising candidate for e-nose due to its printability, variety of applicable polymer materials, and low operation temperature (usually at room temperature),[13,14] which are hardly attainable in conventional metal-oxide semiconductor sensors.[15–21] Previous studies have been mainly devoted to polymer design for detecting various analyte molecules.[22–25] However, the polymer−carbon nanocomposite sensors often suffer from degradation of sensing performance in an air environment. For example, Chiou et al. reported that a polyethylene glycol/multi-walled carbon nanotube nanocomposite sensor exhibited degradation of sensing response to 46% of its initial value after 100 cycles of acetone sensing at 45 °C.[26] Wu et al. reported the degradation of the sensing response in a similar sensor device to ca. 50% of its initial value within 4 days at 25 °C in air.[27] These degradations of sensing responses strongly affect the pattern recognition performance in e-nose and plausibly

cause fatal errors in data analysis. As such, a rational design concept to realize the long-term stable polymer−carbon composite sensor is strongly desired. Here, we demonstrate a design concept for realizing long-term stability in a polyethylene glycol (PEG)−carbon black (CB) nanocomposite sensor under an air environment. Comparison of the sensing properties and infrared (IR) spectroscopy on the same device revealed that the oxidation-induced consumption of PEG is a crucial factor for sensor degradation. According to the mechanism, we introduced an anti-oxidizing agent (i.e., ascorbic acid) into the PEG−CB nanocomposite sensor to suppress the PEG oxidation and successfully demonstrate the long-term stability of sensing properties for 30 days, which had been difficult in conventional polymer−carbon nanocomposite sensors.

3.3 Result and Discussion

Figure 1(a,b)shows the schematic images of the polymer–carbon nanocomposite-based chemiresistive sensor array and its working principle. The sensor consists of electrically conductive carbon nanoparticles and an electrically insulative polymer. In previous studies, 16 types of gas chromatography stationary phases, which exhibit a wide range of adsorption properties for volatile molecules, were selected as polymer materials for e-nose. [28,29] The adsorption of analyte molecules in the polymer matrix induces a volumetric change of the nanocomposite, leading to the increase of electrical resistance by extending the distance between the carbon nanoparticles. Figure 1c shows the optical microscopy images of the polymer–carbon nanocomposite-based chemiresistive sensor array and a sensor device composed of a PEG–CB nanocomposite (PEG 4000, m.w. 3600–4400). PEG is a typical polymer material for the polymer–carbon nanocomposite sensor, [30,31] which enables the detection of a variety of polar molecules. The PEG–CB nanocomposite has a granular shape as shown

in the Supporting Information Figure S1. Figure 1d shows the successive sensing responses of a PEG–CB nanocomposite sensor to 2.7 ppm nonanal at Day 1 and Day 30. Nonanal is a component of perfume, [32] an attractant for *Culex* mosquitoes, [33] an indicator for lipid peroxidation in muscle foods, [34] and a lung cancer biomarker in exhaled breath. [35] The sensing measurements were conducted once a day at room temperature in air with flowing N_2 carrier gas, and at other times, the device was stored at room temperature in air with 67% relative humidity (RH) under dark conditions. The sensing response significantly decreased to ca. 30% of its initial value within 30days, which is consistent with the previous studies. [36,37] Such a decreasing tendency of the sensing response is more clearly seen in Figure 1e. During the test, the device experienced 150 cycles of molecular sensing. Since the stable sensing response was still observed even after the successive 150 cycles of molecular sensing at Day 1 (Figure S2), the degradation of the sensing response must originate from storing the device rather than from the molecular sensing operation. Thus, the degradation of the sensing response under an air environment is proven to be an inevitable issue in a PEG–CB nanocomposite sensor.

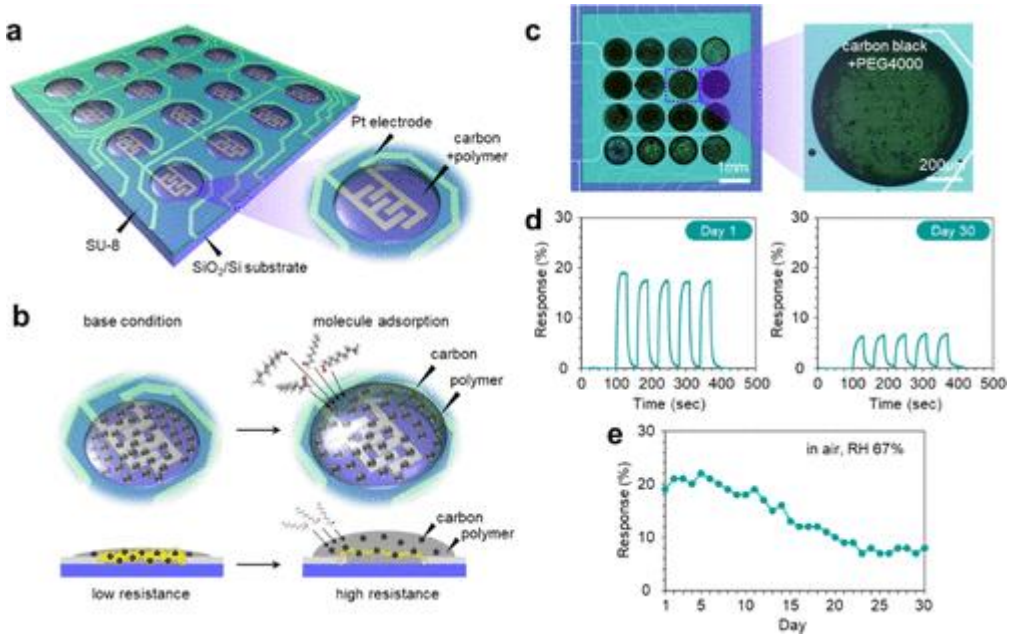

Figure 1. (a,b) Schematic illustrations of (a) chemiresistive sensor array and (b) the working principle of a polymer–carbon nanocomposite sensor. (c) Optical microscopy images of the chemiresistive sensor array (left) and a sensor device of PEG (PEG, PEG4000)–CB nanocomposite (right). (d) Successive sensing responses to 2.7 ppm nonanal at Day 1 (left) and Day 30 (right). (e) Duration of the sensing response to 2.7 ppm nonanal when storing the sensor sample at room temperature in air with RH 67%. All sensing measurements were performed at room temperature in air with N_2 carrier gas.

In order to specify what caused the degradation of the sensing response, we designed a PEG–CB nanocomposite sensor device capable of performing both molecular sensing and IR spectroscopy on the same device by precisely controlling the gap size of Pt electrodes and the thickness of the nanocomposite (see details in the Experimental Section). Such a "2-way device" allows us to directly link the variations of molecular sensing properties and chemical states of the nanocomposite sensor. Figure 2a,b shows the schematic illustration and the photo of the 2-way device, respectively. By using the

2-way device, we first conducted molecular sensing with aging tests under various environments. Figure 2c shows the sensing responses of the 2-way device to 2.7 ppm nonanal at Day 1 and Day 6 for the aging tests in air with RH 0%, N_2 with RH 95%, and N_2 with RH 0%. The aging tests were conducted at 120 °C. Significant degradations of the sensing response were observed at Day 6 in air with RH 0% and N_2 with RH 95%, while the sensing response in N_2 with RH 0% was almost unchanged. Under the former two conditions, the degradation started from Day 2 and progressed with increasing time as shown in Figure 2d. The aging test in O_2 with RH 0% revealed that the observed degradation in air with RH 0% was crucially governed by oxygen (Figure S3). These results suggest that both oxygen and water are the major factors for the degradation of the sensing response in the PEG–CB nanocomposite sensor under an air environment (Figure 1e).

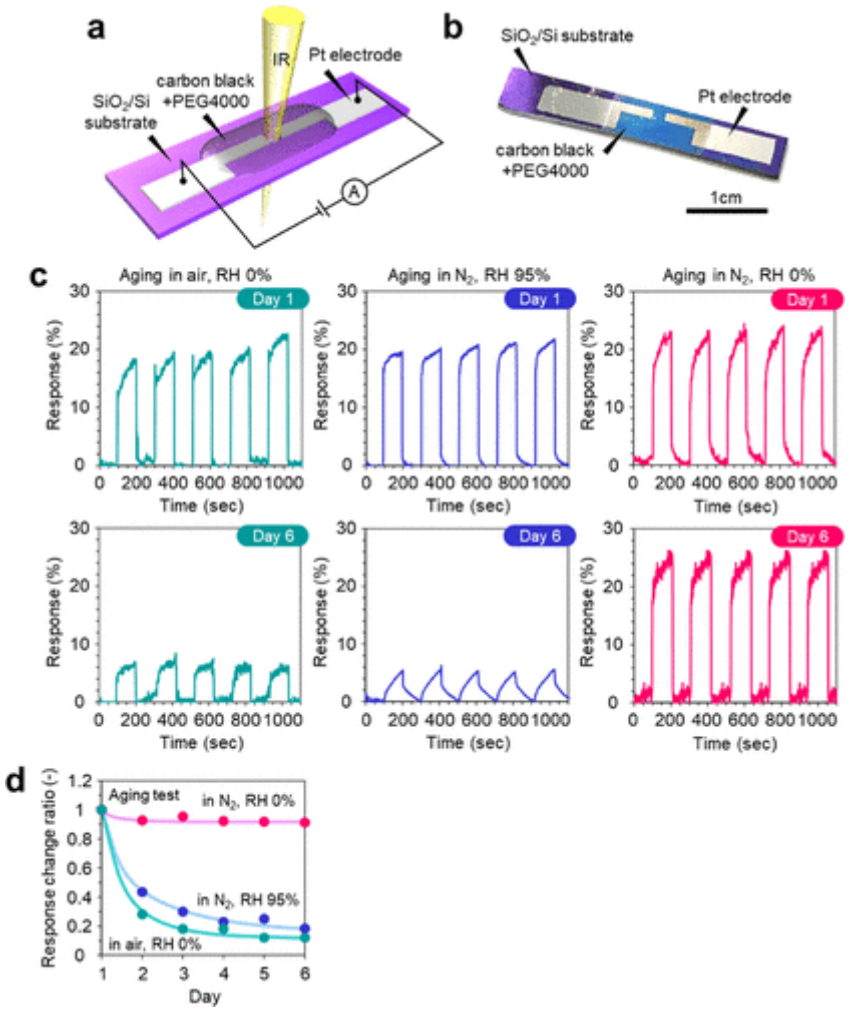

Figure 2. (a) Schematic illustration and (b) photo of the 2-way device capable of performing molecular sensing and IR spectroscopy on the same device. (c) Successive sensing responses to 2.7 ppm nonanal at Day 1 (upper) and Day 6 (lower) when aging the devices in air with RH 0% (left column), N_2 with RH 95% (middle column), and N_2 with RH 0% (right column), respectively. (d) Duration of the sensing response (i.e., response change ratio) to 2.7 ppm nonanal when aging the devices in air with RH 0%, N_2 with RH 95%, and N_2 with RH 0%. The aging tests were conducted at 120 °C. All sensing measurements were performed at room temperature in air with a N_2 carrier gas.

To obtain an in-depth understanding of the degradation mechanism of the PEG–CB nanocomposite sensor in terms of the chemical states, we next performed Fourier transform infrared (FTIR) spectroscopy measurements during the aging tests and compared the results with their molecular sensing data by using the 2-way device. Figure 3 shows the time-dependent FTIR spectra of the 2-way device during the aging tests in (a,d) air with RH 0%, (b,e) N_2 with RH 95%, and (c,f) N_2 with RH 0%, respectively. The aging tests were conducted at 120 °C. Figure 3a–c shows the regions for alkyl group (2800–3200 cm^{-1}) and hydroxyl group (3100–3500 cm^{-1}) and Figure 3d–f shows the carbonyl region (C═O and COO, 1400–1800 cm^{-1}). Similar to the sensing responses shown in Figure 2d, significant variations of IR spectra were observed after Day 2 in air with RH 0% (Figure 3d) and in N_2 with RH 95% (Figure 3b,e), while no obvious variation was seen in N_2 with RH 0% (Figure 3c,f). These trends well correspond to the degradation of the sensing responses shown in Figure 2d and also remind us of the crucial role of oxygen and water. Here, we first discuss the variation of the chemical state of the nanocomposite sensor induced by oxygen. For the aging test in air with RH 0%, three peaks tended to appear at around 1448, 1548, and 1727 cm^{-1} in the carbonyl region (Figure 3d), which are associated with the vibrations of carboxyl groups ν_s(COO) and ν_{as}(COO) and carbonyl group ν(C═O), respectively. [38] They correlate with the formation of aldehyde, formic acid, and acetic acid as oxidation products of PEG. [39–41] The peaks of ν_s(COO) and ν_{as}(COO) became smaller after Day 4, implying the removal of oxidation products. Such formation/removal of carboxyl groups might be irreversible phenomena because they involve the variation of alkyl group as shown in Figure 3a. A similar tendency was observed in the IR spectra of PEG (without CB) but not CB (Figure S5). These results

clearly indicate that the oxidation of PEG triggered the degradation of the sensing response.

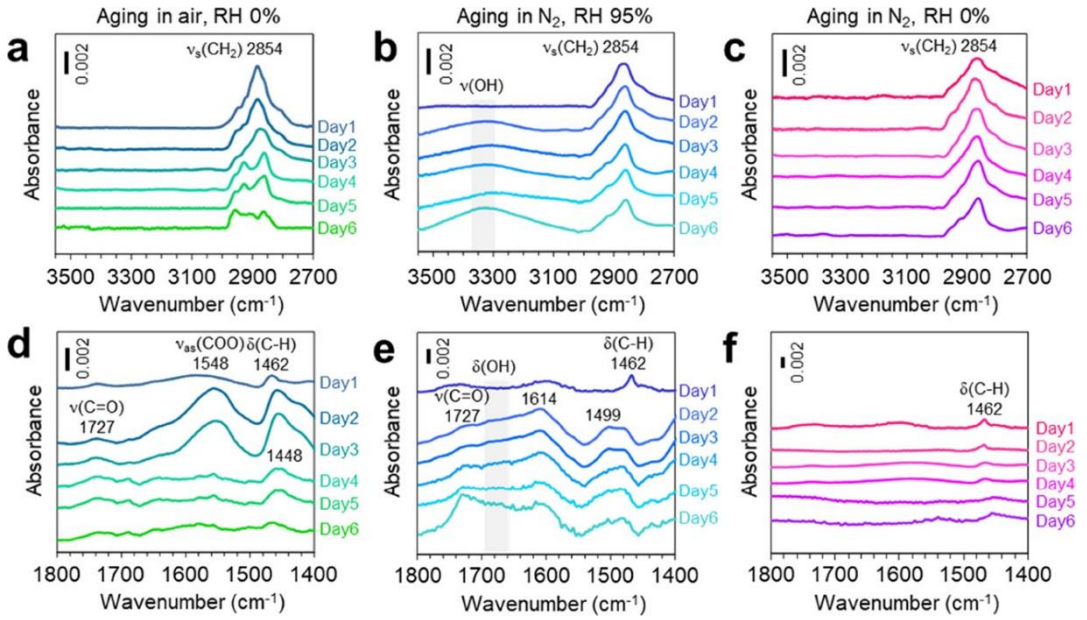

Figure 3. Time-dependent IR spectra of 2-way devices that were aged in (a,d) air with RH 0%, (b,e) N_2 with RH 95%, and (c,f) N_2 with RH 0%, respectively. Panels (a–c) show the regions for alkyl group (2800–3200 cm^{-1}) and hydroxyl group (3100–3500 cm^{-1}) and panels (d–f) show the carbonyl region (C═O and COO, 1400–1800 cm^{-1}). The aging tests were conducted at 120 °C.

Next, we discuss how the chemical state of the PEG–CB nanocomposite sensor varies due to water. For the aging test in N_2 with RH 95%, several peaks tend to appear at around 1460–1540 cm^{-1}, 1580–1760 cm^{-1}, and 3100–3500 cm^{-1}. Two broad peaks at around 1650–1700 cm^{-1} and 3100–3500 cm^{-1} are assigned to δ(OH) and ν(OH), which plausibly originate from the adsorption of water molecules. [42] Consistent results were observed in the sensor resistance, that is, the sensor resistance decreased due to the ionic conduction of adsorbed water (Figure S4). The peak at 1727 cm^{-1} assigned to ν(C═O) tended to be larger during the aging test, which was plausibly due to the formation of an aldehyde group via the gradual oxidation of PEG in aqueous

solution. [43] The other peaks at 1614 and 1499 cm^{-1} were almost unchanged after Day 2. These peaks were sometimes observed in a previous study of PEG while their origins are unclear. [44] Unlike the aging test in air with RH 0%, no significant variation in alkyl group was observed. These results imply that the basic structure of PEG was maintained during the aging test in N_2 with RH 95%. In order to investigate the effect of adsorbed water on the aging of PEG, we performed a thermal treatment to remove the adsorbed water molecules. Figure 4ashows the sensing responses of the 2-way device to 2.7 ppm nonanal at the initial state, after 5 days of aging in N_2 with RH 95% and after 48 h of annealing in N_2 with RH 0%, and Figure 4b,c shows the corresponding IR spectra. Remarkably, the degraded sensing response was recovered to 90% of its initial state after annealing. Consistent results were also observed in the IR spectra, that is, all peaks emerged during the aging test disappeared after the annealing and the shape of the IR spectrum changed back to the initial one. The results indicate that the adsorbed water does not cause fatal degradation in PEG and the sensing response. Also, they clearly highlight that the fatal degradation of the nanocomposite sensor is solely induced by the oxidation of PEG.

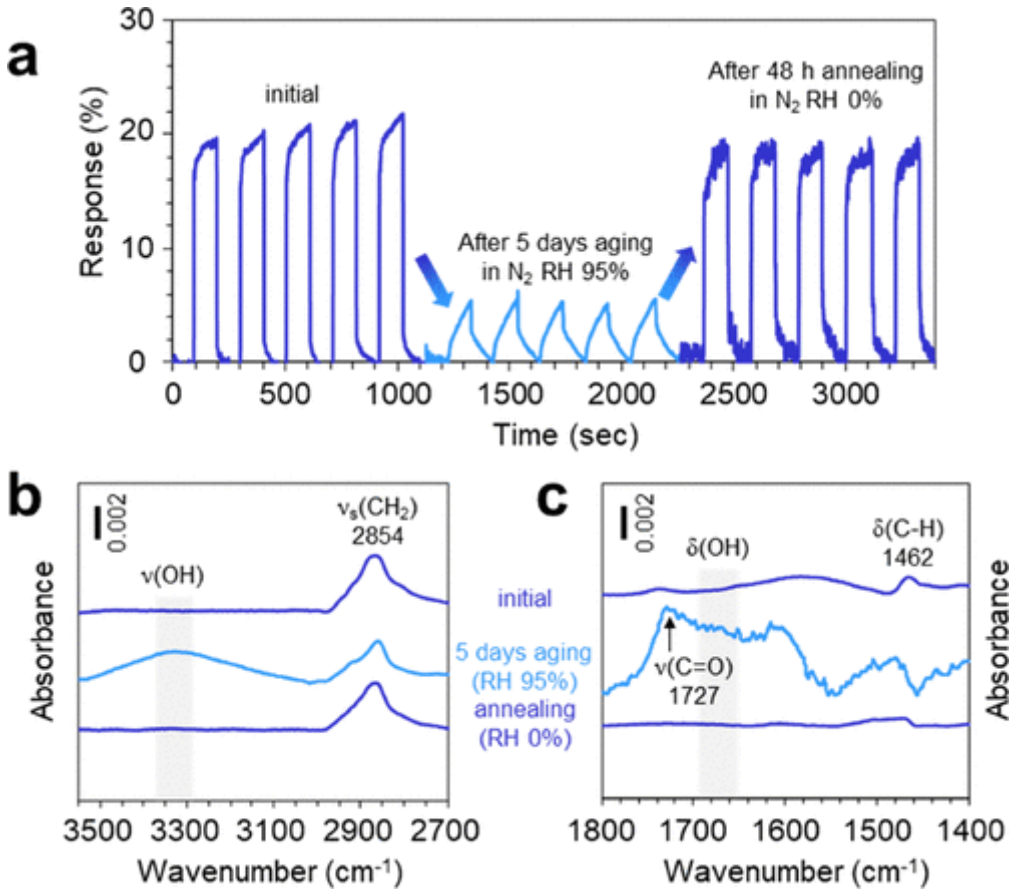

Figure 4. (a) Successive sensing responses of the 2-way device to 2.7 ppm nonanal at the initial state after 5 days of aging in N_2 with RH 95% and after 48 h of annealing in N_2 with RH 0% for dehydration, respectively. The aging test and thermal annealing were conducted at 120 °C. All sensing measurements were performed at room temperature in air with N_2 carrier gas. (b,c) IR spectra of the 2-way device at the initial state after 5 days of aging in N_2 with RH 95% and after 48 h of annealing in N_2 with RH 0% for dehydration, respectively. Panel (b) shows the regions for alkyl group (2800–3200 cm^{-1}) and hydroxyl group (3100–3500 cm^{-1}) and panel (c) show the carbonyl region (C═O and COO, 1400–1800 cm^{-1}).

Here, we consider why the oxidation of PEG led to the degradation of the sensing response in the PEG–CB nanocomposite sensor. The comparison of molecular sensing

data and IR spectra (Figures 2d and 3d) on the same device shows that the degradation of the sensing response was triggered by the oxidation of PEG and further progressed even when the oxidation products were removed. First, we consider that the chemical state of oxidized PEG caused the degradation of the sensing response. This is because the adsorption of analyte molecules and the resultant volumetric change in the polymer–carbon nanocomposite sensors are strongly determined by the affinity between analyte molecules and the polymer material. However, the observed sensor degradation might not be governed by the chemical state of oxidized PEG since a similar degradation trend in sensing response was seen when examining the molecular sensing using the higher polarity molecule of methanol (Figure S6). Next, we assume that the consumption of PEG seriously caused the degradation of the sensing response. This is because the total volumetric change of the nanocomposite sensor during molecular sensing must be suppressed when the amount of PEG is reduced. In fact, the sensing response tended to decrease with decreasing amount ratio of PEG in the PEG–CB nanocomposite (Figure S7). In principle, the oxidation of PEG involves cleavage of the C–C bond. [39–41] Therefore, PEG is supposed to be shorter and consumed via oxidation and the following removal of COO bonds as CO_2 gas (Figure 5a) as implicated by the IR spectra in Figure 3a,d. To directly validate the consumption of PEG, we evaluated the weight of PEG during the aging test in air. As we expected, the weight of PEG drastically decreased during the aging test in air with RH 0% (Figure 5b). Thus, we conclude that the consumption of PEG, triggered by the oxidation, is responsible for the degradation of the sensing response.

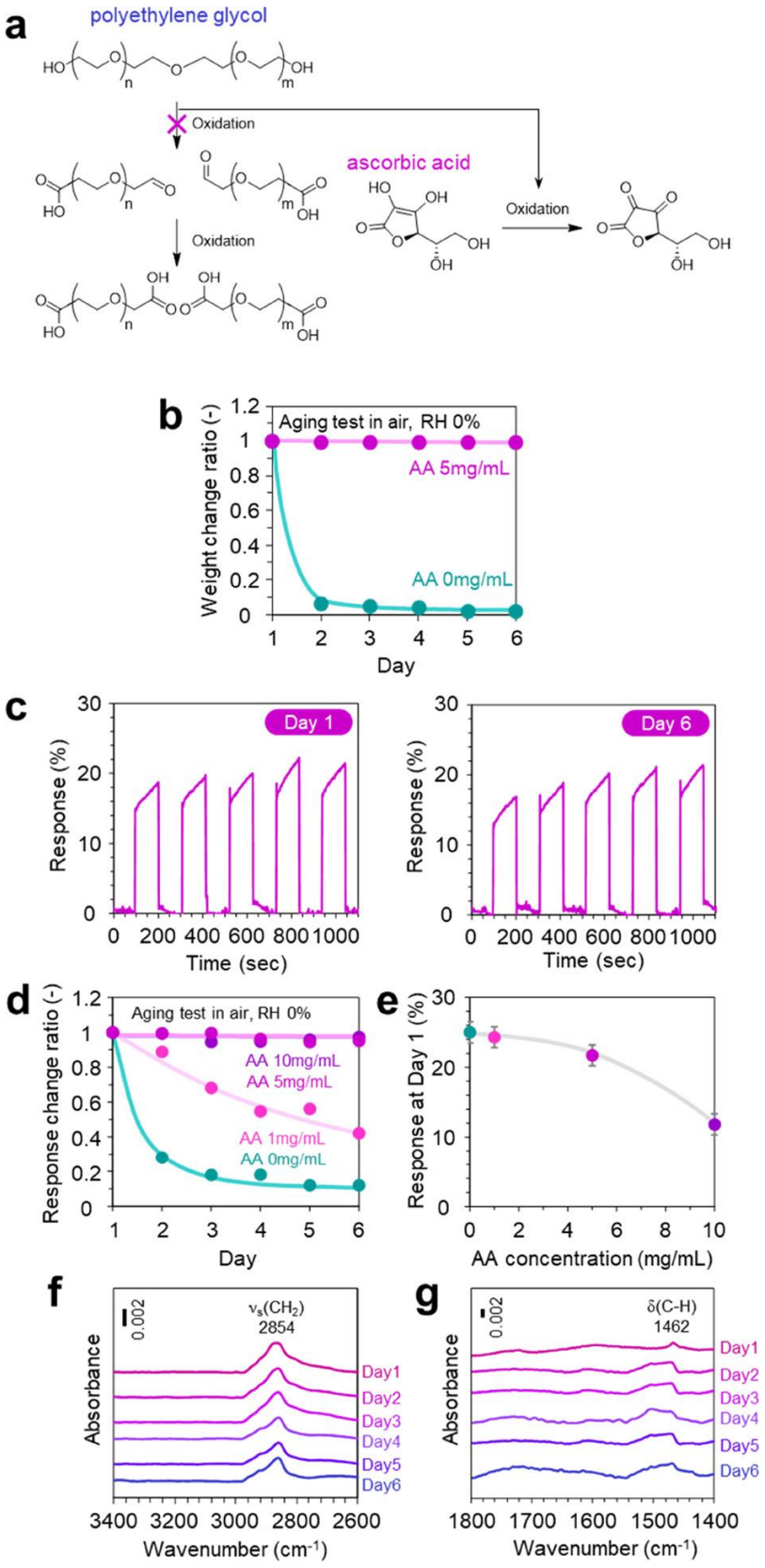

Figure 5. (a) Degradation mechanism of PEG and the proposed approach for suppressing degradation using AA. (b) Duration of weight (i.e., weight change ratio) of

PEG and 5 mg/mL AA-added PEG during the aging test. (c) Successive sensing responses of the 5 mg/mL AA-added 2-way device to 2.7 ppm nonanal at Day 1 and Day 6 during the aging test. (d) Durations of the sensing response (i.e., response change ratio) to 2.7 ppm nonanal and (e) sensor response of the 2-way device with various AA concentrations. All sensing measurements and characterization of sensor resistance were performed at room temperature in air with N_2 carrier gas. (f,g) Time-dependent IR spectra of the 5 mg/mL AA-added 2-way device during the aging test. Panel (f) shows the regions for alkyl group (2800–3200 cm^{-1}) and hydroxyl group (3100–3500 cm^{-1}) and panel (g) shows the carbonyl region (C═O and COO, 1400–1800 cm^{-1}). The aging test was conducted at 120 °C in air at with RH 0%.

The above results suggest that preventing the oxidation of PEG is of crucial importance to achieve the long-term stability of the PEG–CB nanocomposite sensor. In this regard, we examined the addition of an antioxidizing agent (i.e., ascorbic acid (AA)) [43] to the nanocomposite sensor. We expect that the oxidation of PEG is prevented by alternatively oxidizing AA as schematically shown in Figure 5a. In fact, the consumption of PEG was drastically suppressed by the AA addition (Figure S8). Figure 5c shows the successive sensing response of the 2-way device to 2.7 ppm nonanal at Day 1 and Day 6 for the aging test in air with RH 0% when AA of 5 mg/mL was added to the nanocomposite. The aging test was conducted at 120 °C. Contrary to the result shown in Figure 2c, no significant degradation of the sensing response was seen in the AA-added nanocomposite sensor. The effect of the antioxidizing agent is more clearly seen in Figure 5d. The degradation of the sensing response can be prevented by increasing the AA concentration. Note that excess AA addition over 10 mg/mL resulted in the lowering of the sensing response (Figures 5e and S8). This implies that the excess AA interferes with the interaction between PEG andanalyte molecules. The effect of

AA addition on the suppression of degradation in the sensing response was also confirmed by acetone sensing, showing the diverse applicability of the present approach to various analytes (Figure S9). Figure 5f,g shows the IR spectra of the 2-way device during the aging test in air with RH 0% when AA of 5 mg/mL was added to the nanocomposite. The peaks associated with AA cannot be seen at the examined concentration condition (Figure S10). The appearance of ν_s (COO) and ν_{as} (COO) peaks and the variation of alkyl group were not seen in the spectra, indicating that the oxidation of PEG is substantially prevented by adding AA. Such a trend was well consistent with the results of the X-ray diffraction (XRD) measurement (Figure S11). Thus, these results indicate that the oxidation of PEG, which is responsible for the degradation of the PEG–CB nanocomposite sensor, was successfully prevented while maintaining the sensing response by adding an antioxidizing agent (i.e., AA) with a precisely controlled concentration.

Finally, we examined the long-term stability of a PEG–CB nanocomposite sensor. Figure 6a,b shows the optical microscopy images of an AA-added (5 mg/mL) PEG–CB nanocomposite sensor and its successive sensing response to 2.7 ppm nonanal at Day 1 and Day 30. For this experiment, the molecular sensing was performed once a day and the device was kept at room temperature in air with RH 67%. There are no significant variations in the morphology and the sensing response of the nanocomposite sensor. The effect of AA addition on the long-term stability of the nanocomposite sensor can be more clearly seen in Figure 6c. The degradation of the sensing response was significantly improved by adding AA while maintaining the amplitude of the sensing response. Also, the humidity-induced degradation of the sensing response was not seen. This is plausibly due to the fact that the adsorbed water in the nanocomposite sensor is removed by the self-Joule heating occurring during the molecular sensing

measurement. Thus, the long-term stability of the PEG–CB nanocomposite sensor for 30 days was successfully achieved by rationally preventing the oxidation of PEG.

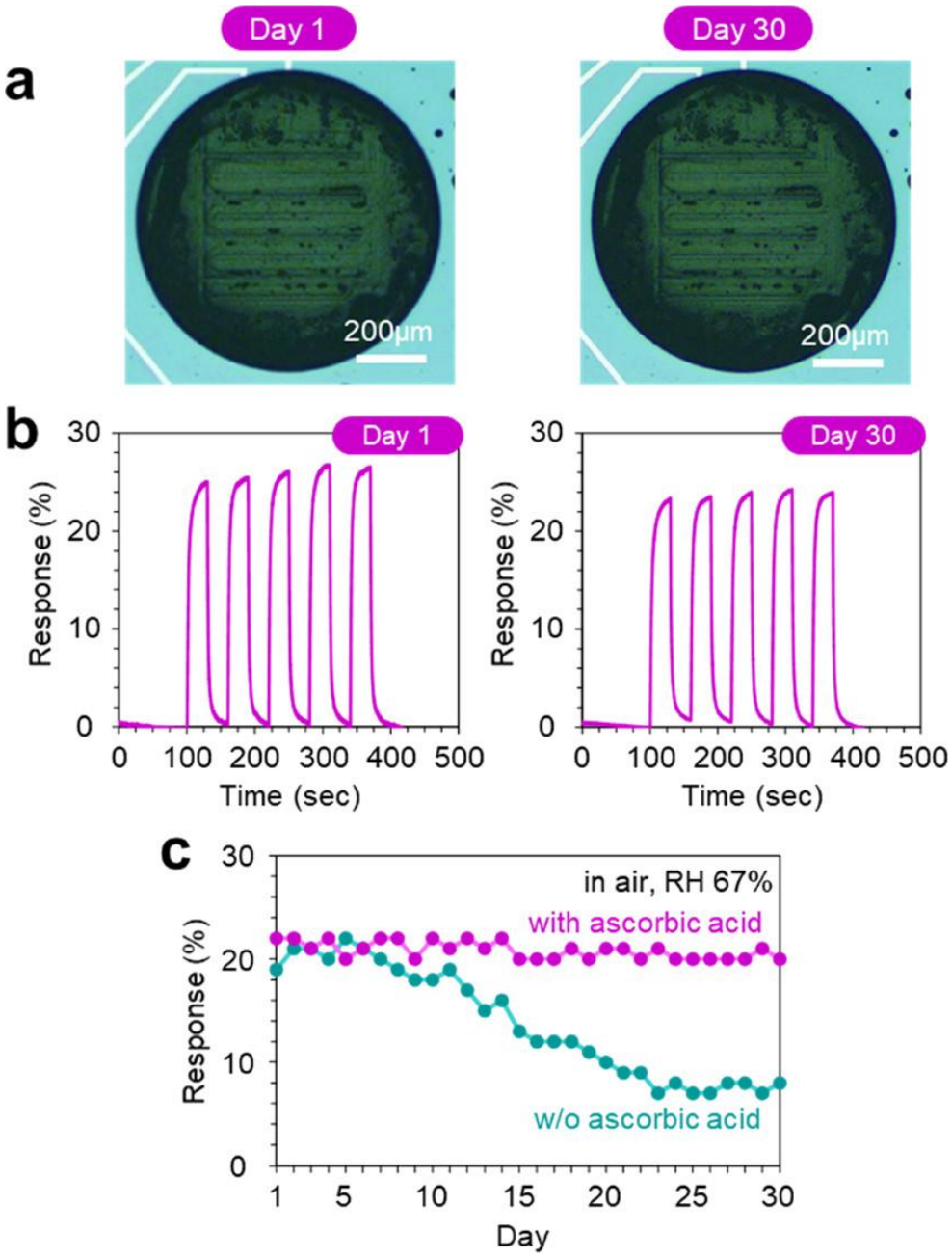

Figure 6. (a) Optical microscopy images of a PEG–CB nanocomposite sensor device with the addition of 5 mg/mL AA at Day 1 (left) and Day 30 (right). (b) Successive sensing responses to 2.7 ppm nonanal at Day 1 (left) and Day 30 (right). (c) Duration of the sensing response to 2.7 ppm nonanal with and without the addition of

AA when storing the sensor sample at room temperature in air with RH 67%. All sensing measurements were performed at room temperature in air with N_2 carrier gas.

3.4 Conclusion

In conclusion, we conducted a mechanistic study for understanding the degradation of the sensing response and realizing long-term stability in a PEG–CB nanocomposite sensor under an air environment, which had been a bottleneck issue in polymer-based chemiresistive sensors. A device capable of performing both electrical molecular sensing and IR spectroscopy was designed to link the degradation of sensing response and the chemical state in a PEG–CB nanocomposite sensor. Comparison of the sensing properties and IR spectroscopy on the same device revealed that the oxidation-induced consumption of PEG is a crucial factor for the sensor degradation. According to the mechanism, we introduced an antioxidizing agent (i.e., AA) into the PEG–CB nanocomposite sensor to suppress the PEG oxidation and successfully demonstrated the long-term stability of sensing properties under an air environment for 30 days. Since oxidation is a common issue in polymer materials, the proposed approach is applicable to diverse polymer–carbon nanocomposite sensors for improving their long-term stability in an air environment.

3.5 Experimental Section

The polymer–CB nanocomposite used in this study was prepared by mixing CB (CB2350, Mitsubishi Chemical) and PEG (PEG4000, Aldrich Chemical Co.) in deionized water with the same quantity of 10 mg/mL. AA (Fujifilm Wako Pure Chemical Co.) was then added to the nanocomposite for suppressing the oxidation of PEG with a concentration of 0–10 mg/mL. The as-prepared nanocomposite was

deposited on a Si substrate (n-type, capped with a 100 nm-thick SiO_2 layer) to fabricate two types of sensor devices including a component of 16-channel sensor array and an electrical sensing/IR spectroscopy 2-way sensor device. For the former sensor device, comb-shaped Pt electrodes with a Ti adhesive layer were first patterned on a 7 × 7 mm^2-sized substrate by combining photolithography and radio frequency sputtering. The gap distance and the thickness of Pt electrodes were 40 μm and 400 nm, respectively. A SU-8 photoresist layer with 45 μm thickness was then coated on the electrode-patterned substrate by spin-coating, and circular holes were patterned on the SU-8 layer by photolithography. The PEG–CB mixed solution was dropped on the patterned substrate by means of ink-jet printing (custom-made, SIJ Technology Inc.).

For the latter device (i.e., electrical sensing/IR spectroscopy 2-way sensor device), Pt electrodes with a Ti adhesive layer were patterned on a 30 × 5 mm^2-sized substrate by means of metal mask. The gap distance and thickness of Pt electrodes for the 2-way device were 2 mm and 300 nm, respectively. The nanocomposite was then spin-coated on the electrode-patterned substrate with the condition of 2000 rpm for 200 s. Both sensor devices were then vacuum-annealed at 120 °C for 24 h to fully remove the solvent. The morphologies of the nanocomposite and the sensor device were characterized by field emission scanning electron microscopy (FESEM, JEOL JSM-7610F) at an accelerating voltage of 15 kV and optical microscopy (OLYMPUS DP21). XRD measurement was performed to evaluate the crystal structure of the nanocomposite. FTIR spectroscopy (Thermo Fisher Scientific Nicolet iS50) was performed for monitoring the degradation of the nanocomposite. The electrical properties and the molecular sensing response of the fabricated sensor devices were characterized by a probe station equipped with a gas supply system, a semiconductor parameter analyzer (Keithley 4200-SCS, for a 2-way device), and a homemade sensing

module (for a component of the 16-channel sensor array). The molecular sensing measurements were conducted using 2.7 ppm nonanal, 5.6 ppm methanol, and 3.9ppm acetone at room temperature in air. Nitrogen (N_2) was utilized as the carrier gas. The readout voltage was 1 V. The sensing response was defined as $(R_g - R_{N2})/R_{N2} \times 100\%$, where R_g and R_{N2} are the resistances of sensor devices exposed to nonanal and N_2, respectively. For the aging tests, the fabricated sensor devices were kept at 120 °C in air with RH 0%, N_2 with RH 95%, and N_2 with RH 0%. Five or six devices were fabricated and characterized for each aging condition in order to obtain reliable data.

3.6 References

(1) Li, K.; Shao, Y.; Yan, H.; Lu, Z.; Griffith, K. J.; Yan, J.; Wang, G.; Fan, H.; Lu, J.; Huang, W.; Bao, B.; Liu, X.; Hou, C.; Zhang, Q.; Li, Y.; Yu, J.; Wang, H. Lattice-contraction triggered synchronous electrochromic actuator. *Nat. Commun.* **2018**, *9*, 1– 11, DOI: 10.1038/s41467-018-07241-7.

(2) Al-Turjman, F.; Lemayian, P. Intelligence, security, and vehicular sensor networks in internet of things (IoT)-enabled smart-cities: An overview. *Comput. Electr. Eng.* **2020**, *87*, 106776 DOI: 10.1016/j.compeleceng.2020.106776.

(3) Zhang, L.; Tian, F.; Nie, H.; Dang, L.; Li, G.; Ye, Q. Classification of multiple indoor air contaminants by an electronic nose and a hybrid support vector machine. *Sens. Actuators, B* **2012**, *174*, 114– 125.

(4) Eusebio, L.; Derudi, M.; Capelli, L.; Nano, G.; Sironi, S. Assessment of the indoor odour impact in a naturally ventilated room. *Sensors* **2017**, *17*, 778,

(5) Macías, M. M.; Manso, A. G.; Orellana, C. J. G.; Velasco, H. M. G.; Caballero, G. R.; Chamizo, J. C. P. Acetic Acid Detection Threshold in Synthetic Wine Samples of a Portable Electronic Nose. *Sensors* **2013**, *13*, 208– 220.

(6) Ampuero, S.; Bosset, J. O. The electronic nose applied to dairy products: a review. *Sens. Actuators, B* **2003**, *94*, 1– 12.

(7) Ho, C. K.; Hughes, R. C. In-Situ Chemiresistor Sensor Package for Real-Time Detection of Volatile Organic Compounds in Soil and Groundwater. *Sensors* **2002**, *2*, 23– 34.

(8) Wilson, A. D. Review of Electronic-nose Technologies and Algorithms to Detect Hazardous Chemicals in the Environment. *Procedia Technol.* **2012**, *1*, 453– 463.

(9) Wang, B.; Cancilla, J. C.; Torrecilla, J. S.; Haick, H. Artificial Sensing Intelligence with Silicon Nanowires for Ultraselective Detection in the Gas Phase. *Nano Lett.* **2014**, *14*, 933– 938.

(10) Nakhleh, M. K.; Amal, H.; Jeries, R.; Broza, Y. Y.; Aboud, M.; Gharra, A.; Ivgi, H.; Khatib, S.; Badarneh, S.; Har-Shai, L.; Glass-Marmor, L.; Lejbkowicz, I.; Miller, A.; Badarny, S.; Winer, R.; Finberg, J.; Cohen-Kaminsky, S.; Perros, F.; Montani, D.; Girerd, B.; Garcia, G.; Simonneau, G.; Nakhoul, F.; Baram, S.; Salim, R.; Hakim, M.; Gruber, M.; Gruber, M.; Ronen, O.; Marshak, T.; Doweck, I.; Nativ, O.; Bahouth, Z.; Shi, D.; Zhang, W.; Hua, Q.; Pan, Y.; Tao, L.; Liu, H.; Karban, A.; Koifman, E.; Rainis, T.; Skapars, R.; Sivins, A.; Ancans, G.; Liepniece-Karele, I.; Kikuste, I.; Lasina, I.; Tolmanis, I.; Johnson, D.; Millstone, S. Z.; Fulton, J.; Wells, J. W.; Wilf, L. H.; Humbert, M.; Leja, M.; Peled, N.; Haick, H. Diagnosis and Classification of 17 Diseases from 1404 Subjects via Pattern Analysis of Exhaled Molecules. *ACS Nano* **2017**, *11*, 112– 125.

(11) Provost, F.; Fawcett, T. Data Science and its Relationship to Big Data and Data-Driven Decision Making. *Big Data* **2013**, *1*, 51– 59.

(12) Bandodkar, A. J.; Jeerapan, I.; Wang, J. Wearable Chemical Sensors: Present Challenges and Future Prospects. *ACS Sens.* **2016**, *1*, 464– 482.

(13) Lorwongtragool, P.; Sowade, E.; Watthanawisuth, N.; Baumann, R. R.; Kerdcharoen, T. A Novel Wearable Electronic Nose for Healthcare Based on Flexible Printed Chemical Sensor Array. *Sensors* **2014**, *14*, 19700– 19712.

(14) Chatterjee, S.; Castro, M.; Feller, J. F. An e-nose made of carbon nanotube-based quantum resistive sensors for the detection of eighteen polar/nonpolar VOC biomarkers of lung cancer. *J. Mater. Chem. B* **2013**, *1*, 4563– 4575.

(15) Tomchenko, A. A.; Harmer, G. P.; Marquis, B. T.; Allen, J. W. Semiconducting metal oxide sensor array for the selective detection of combustion gases. *Sens. Actuators, B* **2003**, *93*, 126– 134.

(16) Sun, Y. F.; Liu, S. B.; Meng, F. L.; Liu, J. Y.; Zhen, J.; Kong, L. T.; Liu, J. H. Metal Oxide Nanostructures and Their Gas Sensing Properties: A Review. *Sensors* **2012**, *12*, 2610– 2631.

(17) Meng, G.; Zhuge, F. W.; Nagashima, K.; Nakao, A.; Kanai, M.; He, Y.; Boudot, M.; Takahashi, T.; Uchida, K.; Yanagida, T. Nanoscale Thermal Management of Single SnO_2 Nanowire: pico-Joule Energy Consumed Molecule Sensor. *ACS Sens.* **2016**, *1*, 997– 1002.

(18) Wang, C.; Hosomi, T.; Nagashima, K.; Takahashi, T.; Zhang, G.; Kanai, M.; Yoshida, H.; Yanagida, T. Phosphonic Acid Modified ZnO Nanowire Sensors: Directing Reaction Pathway of Volatile Carbonyl Compounds. *ACS Appl. Mater. Interfaces* **2020**, *12*, 44265– 44272.

(19) Liu, J.; Nagashima, K.; Nagamatsu, Y.; Hosomi, T.; Saito, H.; Wang, C.; Mizukami, W.; Zhang, G.; Samransuksamer, B.; Takahashi, T.; Kanai, M.; Yasui, T.; Baba, Y.; Yanagida, T. The impact of surface Cu^{2+} of ZnO/$(Cu_{1-x}Zn_x)O$ heterostructured nanowires on the adsorption and chemical transformation of carbonyl compounds. *Chem. Sci.* **2021**, *12*, 5073– 5081.

(20) Nekita, S.; Nagashima, K.; Zhang, G.; Wang, Q.; Kanai, M.; Takahashi, T.; Hosomi, T.; Nakamura, K.; Okuyama, T.; Yanagida, T. Face-Selective

Crystal Growth of Hydrothermal Tungsten Oxide Nanowires for Sensing Volatile Molecules. *ACS Appl. Nano Mater.* **2020**, *3*, 10252– 10260.

(21) Zhang, G.; Hosomi, T.; Mizukami, W.; Liu, J.; Nagashima, K.; Takahashi, T.; Kanai, M.; Sugiyama, T.; Yasui, T.; Aoki, T.; Baba, Y.; Ho, J. C.; Yanagida, T. *J. Mater. Chem.* **2021**, *9*, 5815– 5824.

(22) Hu, N.; Karube, Y.; Arai, M.; Watanabe, T.; Yan, C.; Li, Y.; Liu, Y.; Fukunaga, H. Investigation on sensitivity of a polymer/carbon nanotube composite strain sensor. *Carbon* **2010**, *48*, 680– 687.

(23) Ryan, M. A.; Shevade, A. V.; Zhou, H.; Homer, M. L. Polymer–carbon black composite sensors in an electronic nose for air-quality monitoring. *MRS Bull.* **2004**, *29*, 714– 719.

(24) Zee, F.; Judy, J. W. Micromachined polymer-based chemical gas sensor array. *Sens. Actuators, B* **2001**, *72*, 120– 128.

(25) Xie, H.; Yang, Q.; Sun, X.; Yang, J.; Huang, Y. Gas sensor arrays based on polymer-carbon black to detect organic vapors at low concentration. *Sens. Actuators, B* **2006**, *113*, 887– 891.

(26) Chiou, J. C.; Wu, C. C.; Lin, T. M. Sensitivity Enhancement of Acetone Gas Sensor using Polyethylene Glycol/Multi-Walled Carbon Nanotubes Composite Sensing Film with Thermal Treatment. *Polymer* **2019**, *11*, 423.

(27) Wu, Z.; Chen, X.; Zhu, S.; Zhou, Z.; Yao, Y.; Quan, W.; Liu, B. Enhanced sensitivity of ammonia sensor using graphene/polyaniline nanocomposite. *Sens. Actuators, B* **2013**, *178*, 485– 493.

(28) Wyszynski, B.; Yatabe, R.; Nakao, A.; Nakatani, M.; Oki, A.; Oka, H.; Toko, K. Array of Chemosensitive Resistors with Composites of Gas Chromatography

(GC) Materials and Carbon Black for Detection and Recognition of VOCs: A Basic Study. *Sensors* **1606**, *2017*, 17.

(29) Yatabe, R.; Shunori, A.; Wyszynski, B.; Hanai, Y.; Nakao, A.; Nakatani, M.; Oki, A.; Oka, H.; Washio, T.; Toko, K. Odor Sensor System Using Chemosensitive Resistor Array and Machine Learning. *IEEE Sens. J.* **2021**, *21*, 2077– 2083.

(30) Niu, L.; Luo, Y.; Li, Z. A highly selective chemical gas sensor based on functionalization of multi-walled carbon nanotubes with poly (ethylene glycol). *Sens. Actuators, B* **2007**, *126*, 361– 367.

(31) Rahman, M. M.; Hussein, M. A.; Salam, M. A.; Asiri, A. M. Fabrication of an L-glutathione sensor based on PEG-conjugated functionalized CNT nanocomposites: a real sample analysis. *New J. Chem.* **2017**, *41*, 10761– 10772.

(32) Kim, M.; Sowndhararajan, K.; Choi, H. J.; Park, S. J.; Kim, S. Olfactory Stimulation Effect of Aldehydes, Nonanal, and Decanal on the Human Electroencephalographic Activity, According to Nostril Variation. *Biomedicines* **2019**, *7*, 57.

(33) Syed, Z.; Leal, W. S. Acute olfactory response of Culex mosquitoes to a human- and bird-derived attractant. *Proc. Natl. Acad. Sci. U. S. A.* **2009**, *106*, 18803– 18808.

(34) Ross, C. F.; Smith, D. M. Use of volatiles as indicators of lipid oxidation in muscle foods. *Compr. Rev. Food Sci. Food Saf.* **2006**, *5*, 18– 25.

(35) Itoh, T.; Miwa, T.; Tsuruta, A.; Akamatsu, T.; Izu, N.; Shin, W.; Park, J.; Hida, T.; Eda, T.; Setoguchi, Y. Development of an exhaled breath monitoring system

with semiconductive gas sensors, a gas condenser unit, and gas chromatograph columns. *Sensors* **2016**, *16*, 1891.

(36) Sakai, Y.; Matsuguchi, M.; Hurukawa, T. Humidity sensor using cross-linked poly(chloromethyl styrene). *Sens. Actuators, B* **2000**, *66*, 135– 138.

(37) Gong, M. S.; Kim, J. U.; Kim, J. G. Preparation of water-durable humidity sensor by attachment of polyelectrolyte membrane to electrode substrate by photochemical crosslinking reaction. *Sens. Actuators, B* **2010**, *147*, 539.

(38) Wang, C.; Hosomi, T.; Nagashima, K.; Takahashi, T.; Zhang, G. Z.; Kanai, M.; Zeng, H.; Mizukami, W.; Shioya, N.; Shimoaka, T.; Tamaoka, T.; Yoshida, H.; Takeda, S.; Yasui, T.; Baba, Y.; Aoki, Y.; Terao, J.; Hasegawa, T.; Yanagida, T. Rational method of monitoring molecular transformations on metal-oxide nanowire surfaces. *Nano Lett.* **2019**, *19*, 2443– 2449.

(39) Han, S.; Kim, C.; Kwon, D. Thermal/oxidative degradation and stabilization of polyethylene glycol. *Polymer* **1997**, *38*, 317– 323.

(40) Hester, T. H.; Castillo, D. E.; Goebbert, D. J. Fragmentation of deprotonated polyethylene glycols, $[PEG–H]^-$. *Rapid Commun. Mass Spectrom.* **2013**, *27*, 1643– 1648..

(41) Glastrup, J. Degradation of polyethylene glycol. A study of the reaction mechanism in a model molecule: tetraethylene glycol. *Polym. Degrad. Stab.* **1996**, *52*, 217– 222.

(42) Nodari, L.; Ricciardi, P. Non-invasive identification of paint binders in illuminated manuscripts by ER-FTIR spectroscopy: a systematic study of the influence of different pigments on the binders' characteristic spectral features. *Herit. Sci.* **2019**, *7*, 1– 13.

(43) Hemenway, J. N.; Carvalho, T. C.; Rao, V. M.; Venkatramana, M. R.; Yongmei, W.; Jaquan, K. L.; Ajit, S. N.; Srinivasa, R. P.; Howard, J. S.; Sailesh, A. V. Formation of reactive impurities in aqueous and neat polyethylene glycol 400 and effects of antioxidants and oxidation inducers. *J. Pharm. Sci.* **2012**, *101*, 3305– 3318.

(44) Reddy, K. S.; Prabhakar, M. N.; Babu, P. K.; Venkatesulu, G.; Rao, U. S. K.; Rao, K. C.; Subha, M. C. S. Miscibility Studies of Hydroxypropyl Cellulose/Poly(Ethylene Glycol) in Dilute Solutions and Solid State. *Int. J. Carbohydr. Chem.* **2012**, *2012*, 906389.

3.7 Supporting Information

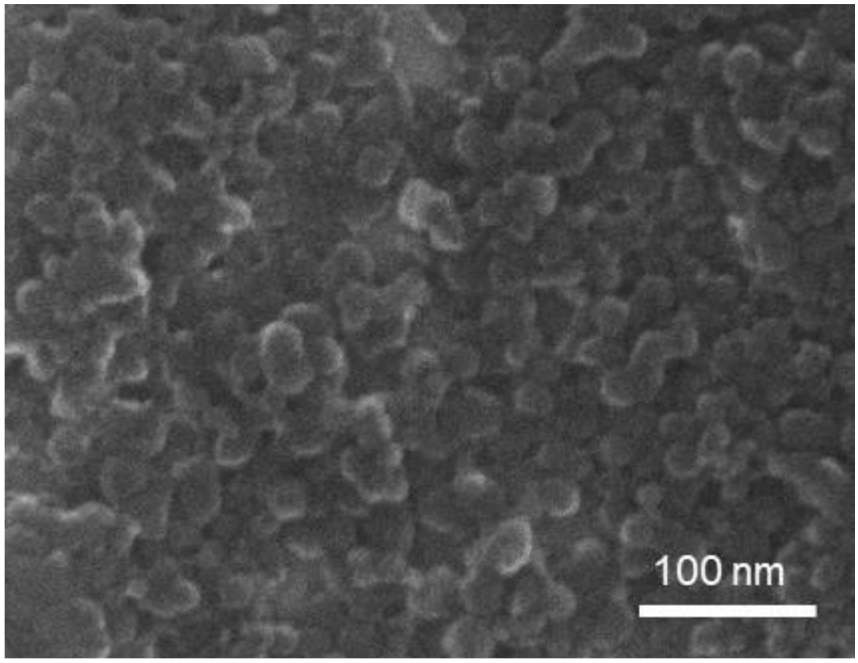

Figure S1. FESEM image of PEG-CB nanocomposite sensor surface.

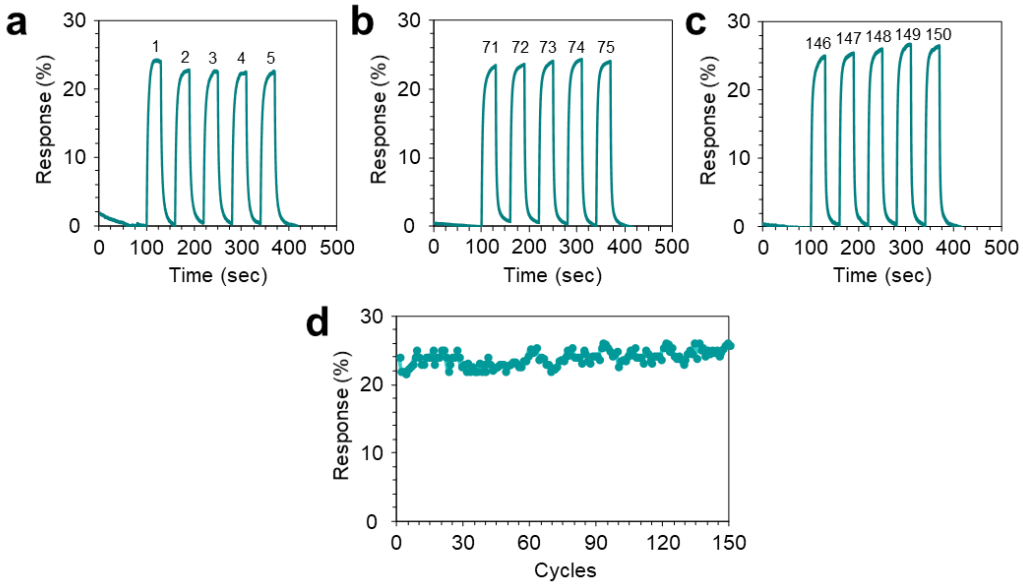

Figure S2. 150 cycles of successive sensing responses of PEG-CB nanocomposite sensor to 2.7 ppm nonanal; (a) 1-5 cycles, (b) 71-75 cycles and (c) 146-150 cycles. (d) Duration of sensing response to 2.7 ppm nonanal. Sensing measurements were performed at room temperature in air with N_2 carrier gas on a same day.

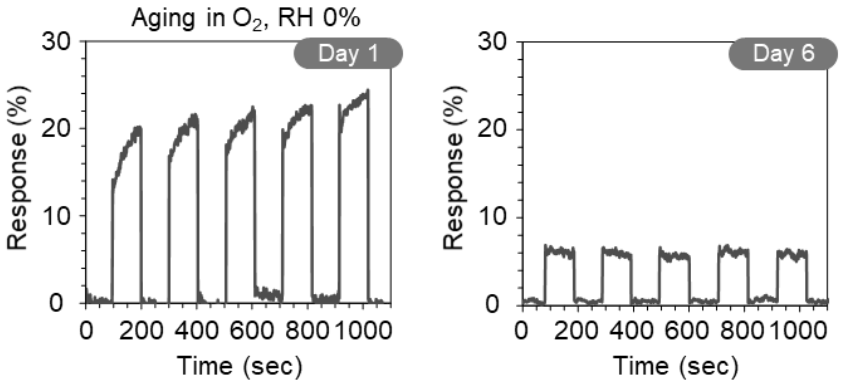

Figure S3. Successive sensing responses of 2-way device to 2.7 ppm nonanal at Day 1 (left) and Day 6 (right) when aging the devices in O_2 with RH 0 %. The aging test was conducted at 120 ºC. The sensing measurements were performed at room temperature in air with N_2 carrier gas.

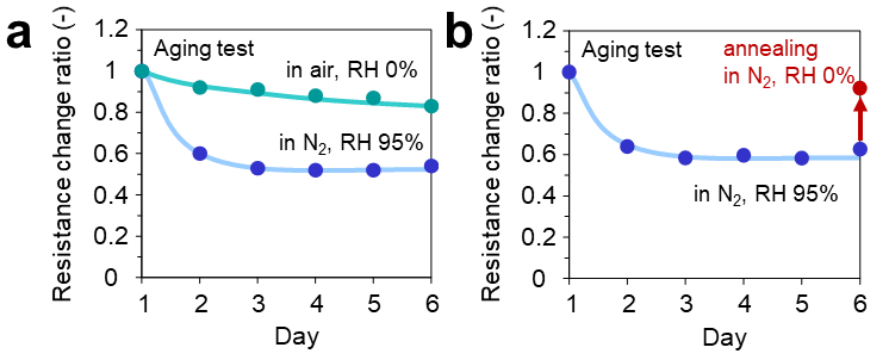

Figure S4. (a) Durations of base resistance of 2-way devices when aging in air with RH 0 % and N_2 with RH 95 %. The aging test was conducted at 120 ºC. (b) Durations of base resistance of 2-way devices when aging in N_2 with RH 95 %, followed by annealing in N_2 with RH 0 %. The aging test was conducted at 120 ºC. All measurements were performed at room temperature under N_2 flow. The base resistance significantly decreased down to ca. 50 % of initial value in high humidity condition while it slightly decreased in air condition. Furthermore, the base resistance was increased when further annealing the device in N_2 with RH 0 %. These indicate that the decreasing trend of sensor resistance in high humidity condition is due to the electrical leakage induced by ionic conduction through the adsorbed water.

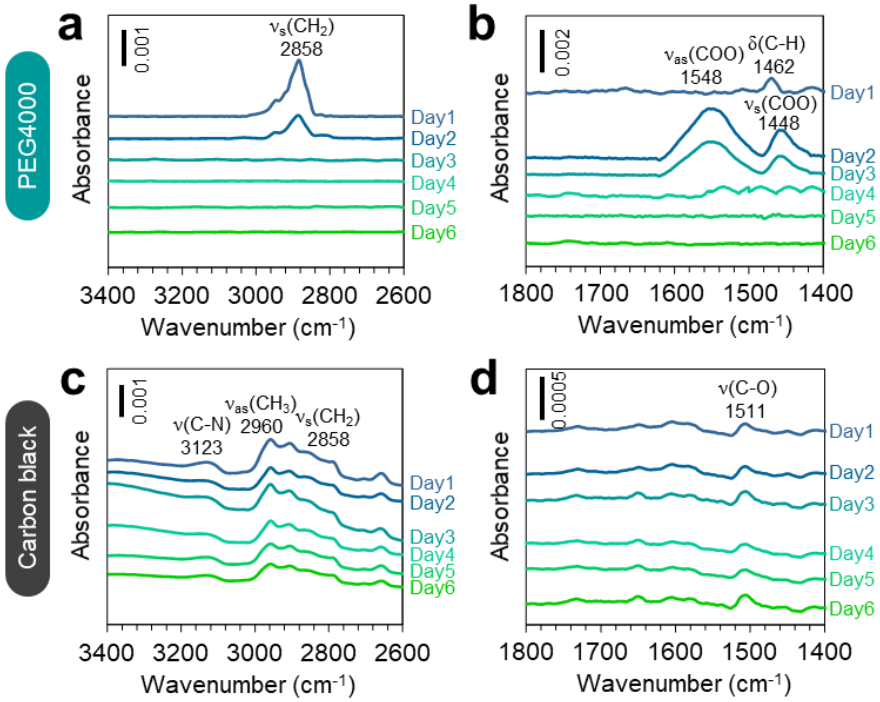

Figure S5. Time-dependent FTIR spectra of (a,b) PEG and (c,d) CB, which were aged in air with RH 0 %. (a) and (c) cover the regions for alkyl group (2800-3200 cm^{-1}) and hydroxyl group (3100-3500 cm-1), and (b) and (d) cover the carbonyl region (C=O and COO, 1400-1800 cm-1), respectively. The aging test was conducted at 120 ºC. In PEG, the νs(CH2) peak almost disappeared after Day 3 and νs(COO) and νas(COO) peaks disappeared after Day 4 while such significant change of $\nu s(CH_2)$ peak was not seen in PEG-CB nanocomposite (Figure 3(a)). This is plausibly because CB served as a mild antioxidant[Ref] and suppressed the oxidation of PEG.

Reference

Hawkins et al. *Rubber Chem. Technol.* **1959**, 32, 4

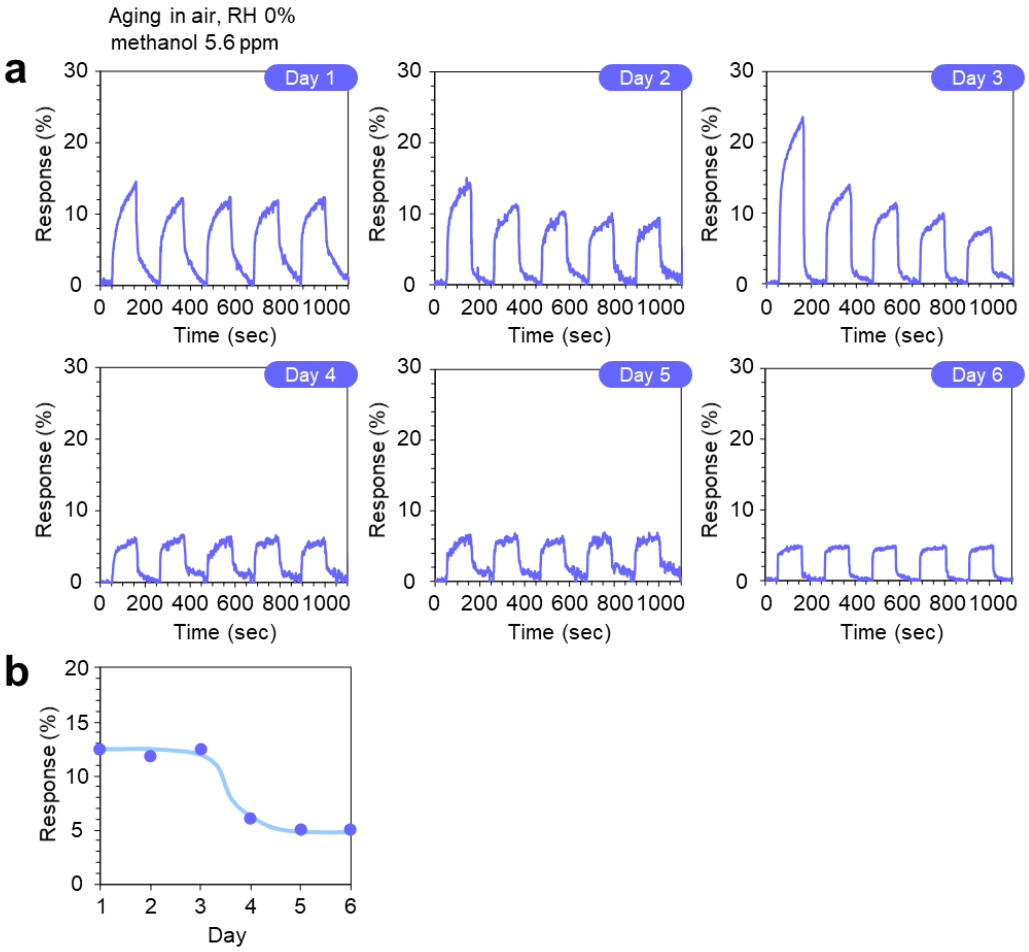

Figure S6. (a) Successive sensing responses of 2-way device to 5.6 ppm methanol from Day 1 to Day 6 when aging the devices in air at with RH 0 %. (b) Duration of sensing response to 5.6 ppm methanol. The aging test was conducted at 120 ºC. The sensing measurements were performed at room temperature in air with N_2 carrier gas.

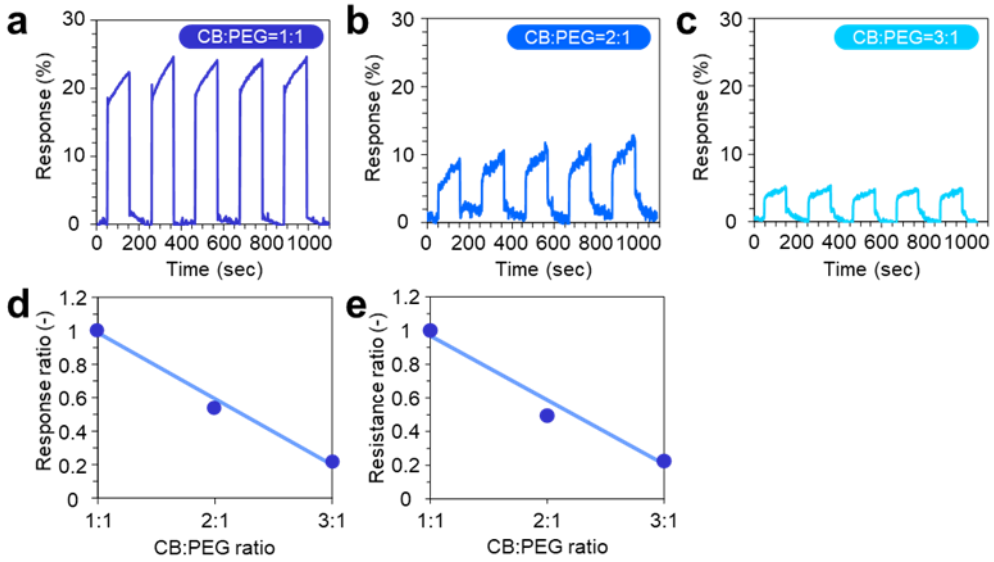

Figure S7. (a-c) Successive sensing responses of 2-way device to 2.7 ppm nonanal with varying the amount ratio of CB:PEG; (a) 1:1, (b) 2:1, (c) 3:1. (d) Sensing response ratio to nonanal and (e) ratio of base resistance with varying the amount ratio of CB:PEG. The sensing measurements were performed at room temperature in air with N_2 carrier gas immediately after fabricating the devices.

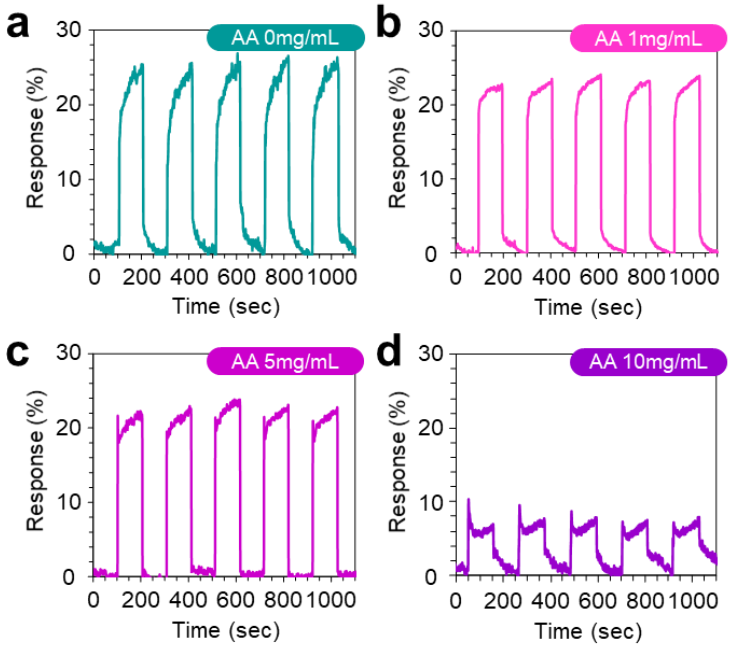

Figure S8. Successive sensing responses of 2-way devices to 2.7 ppm nonanal with various the ascorbic acid (AA) concentration; (a) 0 mg/mL, (b) 1 mg/mL, (c) 5 mg/mL and (d) 10 mg/mL. The sensing measurements were performed at room temperature in air with N_2 carrier gas.

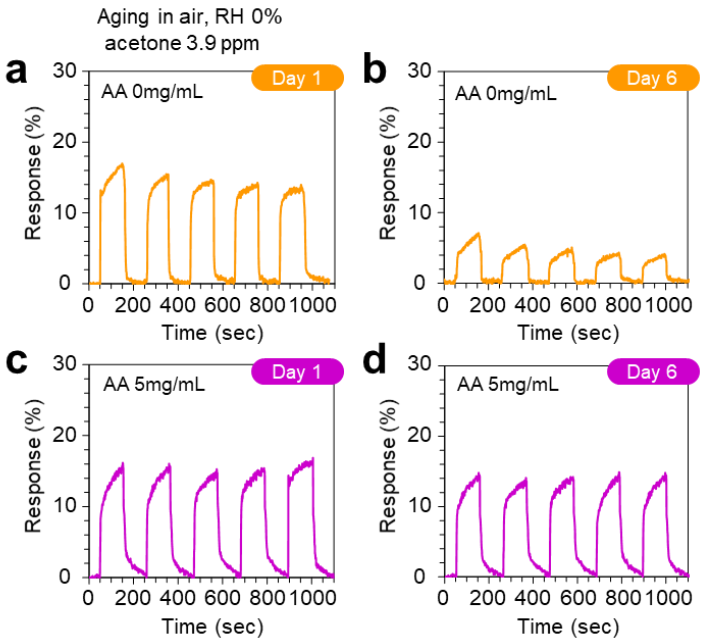

Figure S9. Successive sensing responses of 2-way device to 3.9 ppm acetone when aging the devices in air at with RH 0 % with (a) ascorbic acid (AA) 0 mg/mL (Day 1), (b) AA 0 mg/mL (Day 6), (c) AA 5 mg/mL (Day 1) and (d) AA 5 mg/mL (Day 6). The aging test was conducted at 120 ºC. The sensing measurements were performed at room temperature in air with N_2 carrier gas.

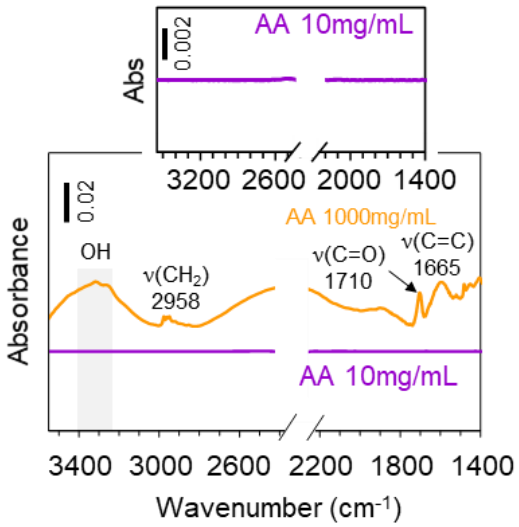

Figure S10. FTIR spectra of ascorbic acid (AA) coated on Si substrate at concentration of 10 mg/mL and 1000 mg/mL in water. The measurements were performed after drying the solvent.

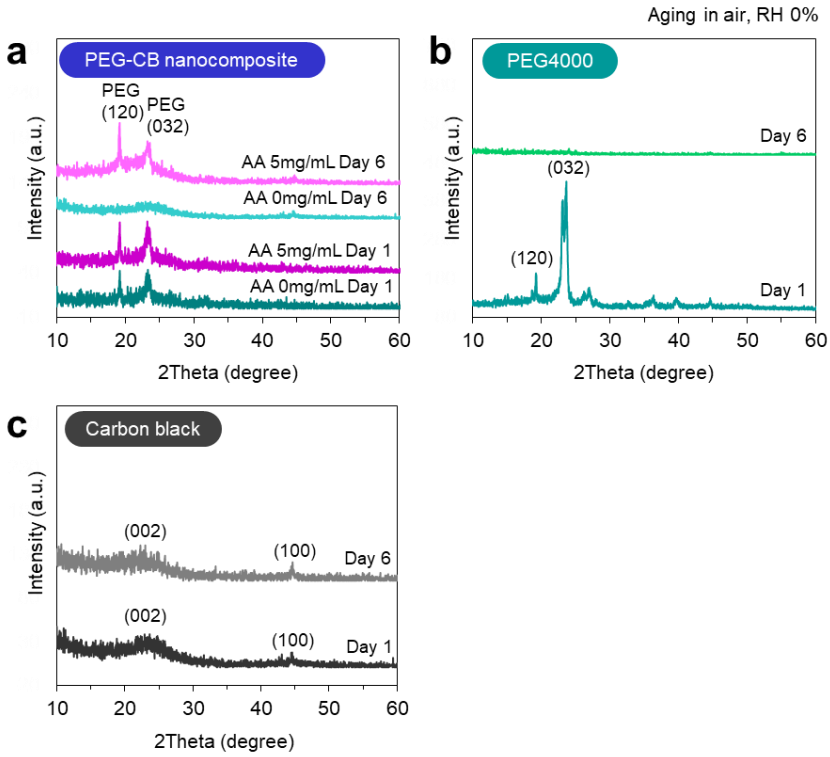

Figure S11. XRD patterns of (a) PEG-CB nanocomposite, (b) PEG and (c) CB when performing aging test (120 ºC, in air, RH 0%). For PEG-CB nanocomposite, the result of ascorbic acid (AA) addition was also displayed.

We found that the peaks observed in PEG and PEG-CB nanocomposite at Day 1 disappeared at Day 6, while no significant variation was observed in CB. On the contrary, when AA was added, the peaks of PEG-CB were maintained even at Day 6. These results strongly support our model that the oxidization induced decomposition of PEG was suppressed by the AA addition.

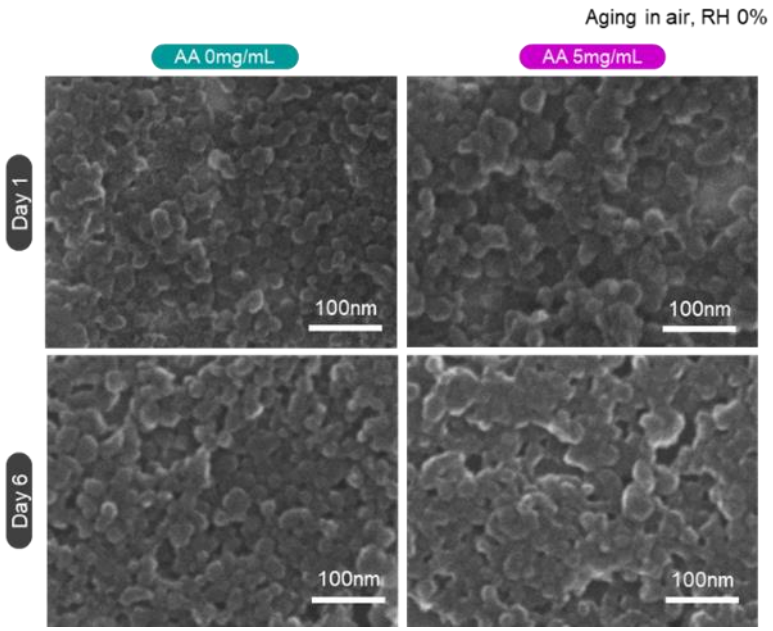

Figure S12. FESEM images of PEG-CB nanocomposite sensor surface with and without ascorbic acid (AA) addition. The result of aging test (120 ºC, in air, RH 0%) is also displayed. No obvious morphological change was observed among all of SEM images.

CHAPTER IV

METAL OXIDE NANOWIRE ARRAY STRUCTURE AS A PLATFORM TO ANALYZE THE ADSORPTION BEHAVIORS OF VOLATILE MOLECULES

4.1 Abstract

Metal oxide nanowires have demonstrated their promise for applications in chemical sensors, inhomogeneous catalysts, molecular filters and so on, due to their material robustness in air/water environments. Understanding a molecule-to-surface interaction of volatile molecule on metal oxide nanowires is of crucial importance to design the performances of these applications. We investigated material dependent molecule-to-surface interactions of volatile molecules using a core-shell metal oxide nanowire array. Varying the metal oxide species (ZnO, ZrO_2 and TiO_2), we clearly observed the metal cation dependence on the bonding strength of 2-nonanone. In addition, the quantitative analysis of molecular adsorption amount was successfully performed using the nanowire array. The results highlighted that the core-shell nanowire array provides a foundation for understanding and designing the molecule-to-surface interactions on various applications.

Keywords: *Metal oxide nanowire array, molecule-to-surface interaction, 2-nonanone, surface metal cations*

4.2 Introduction

Metal oxide nanowires have proven their great promises for applications in chemical sensors, inhomogeneous catalysts, molecular filters and so on, due to their thermal/chemical robustness in air and water.[1-4] Understanding the molecule-to-surface interaction of volatile molecules on metal oxide nanowires is of crucial importance to design the performances of these applications.[5-8] For their fundamental studies, the main interest is the material dependence, and thus many studies have been attempted so far by varying the metal oxide species and/or the dopant species.[9] However, varying the material species frequently involve the morphological changes due to the intrinsic nature of self-assembled nanowire synthesis,[10,11] which makes difficult to quantitatively analyze the molecular adsorption behaviors on various metal oxide nanowire species.

In this study, we employed core-shell metal oxide nanowire array to investigate the molecule-to-surface interaction on various nanowire species. Previous our study demonstrated that ZnO nanowire array on a substrate successfully revealed the impact of Zn^{2+} on the chemical transformation of volatile aldehyde molecules by amplifying the spectroscopic and spectrometric signals using its huge surface.[12] Also, the benefit of the acquired knowledge was proven in the molecular sensing application.[13,14] This study applies the nanowire array as a template to form a core-shell nanowire array with various metal oxide species. The core-shell nanowires allow us to alter the metal oxide species while maintaining the nanowire morphology. The well-defined surface area of nanowire array allows us to quantitatively analyze the molecular adsorption amount when comparing with different material species. In this study, ZnO, ZrO_2 and TiO_2 were selected in terms of the variations of Lewis acidity and coordination number of composed metal cations. The material dependence on the molecular adsorption behaviors was investigated by these nanowire species using analyte molecule of 2-

nonanone, which is known to be a volatile biomarker of *Pseudomonas aeruginosa* in cystic fibrosis and a thermally derived off-flavor compound in milk.[15,16]

4.3 Experimental Section

Fabrication of nanowire array. We prepared three nanowire arrays including ZnO nanowires, ZnO/ZrO_2 core-shell nanowires and ZnO/TiO_2 core-shell nanowires. For constructing the core-shell nanowire arrays, firstly a ZnO nanowire array was prepared on SiO_2 coated Si (100) substrate by a seed-assisted hydrothermal method.[17-20] Ti adhesion layer (5 nm) and ZnO seed layer (100 nm) were deposited on the substrate by radio frequency (RF) sputtering. Aqueous solution for the nanowire growth was prepared by mixing 50 mM zinc acetate dehydrate ($Zn(CH_3COO)_2 \cdot 2H_2O$, Sigma-Aldrich ≥98.0 %), 50 mM hexamethylenetetramine ($C_6H_{12}N_4$, Wako 99.0 %) and 4.0 g polyethyleneimine (PEI, M_n~1800, Sigma-Aldrich 50 wt% in H_2O) in 200 mL deionized (DI) water. The substrate with ZnO seed layer was immersed into the aqueous solution in manner of up-side-down to avoid the precipitated deposition on the substrate during the nanowire growth. ZnO nanowires were grown by conducting the hydrothermal process at 95 ºC for 3-24 h. After the growth, the samples were rinsed by DI water and dried by air blow. For ZnO/ZrO_2 nanowires and ZnO/TiO_2 nanowires, we fabricated the core-shell nanowire heterostructures by depositing the ZrO_2 and TiO_2 shell layers on the ZnO nanowires with RF sputtering at room temperature.[21-23] For comparison, ZnO/ZnO core-shell nanowires were also fabricated in the same manner. Finally, the samples were annealed at 400 ºC in air. Another thermal annealing condition was attempted at 800 ºC in vacuum (8×10^{-3} Pa) for 30 min to modulate the surface state of ZnO nanowires.[12]

Characterization. The morphology, the composition and the chemical state of the prepared nanowire arrays were characterized by field emission scanning electron microscope (FESEM) equipped with energy dispersive x-ray spectroscopy (EDS), x-ray photoemission spectroscopy (XPS). The chemical state and the amount of surface adsorbed molecules were evaluated by Fourier transform infrared spectroscopy (FTIR) equipped with MCT (HgCdTe) detector. The bonding strength of surface-adsorbed molecules was analyzed by the temperature programmed desorption (TPD) measurements using gas chromatograph-mass spectrometry (GCMS). Prior to FTIR and GCMS, the analyte molecule of 2-nonanone was adsorbed on the sample surface at room temperature in a closed vial bottle filled with saturated vapor molecules. The other detailed conditions of these characterization are shown in Supporting Information.

4.4 Results and Discussion

Firstly, we characterized the morphology of nanowire arrays for ZnO nanowires, ZnO/ZrO_2 nanowires and ZnO/TiO_2 nanowires (Figure 1A-C). The results of morphological characterization by SEM are shown in Figure 1D-F and Figure S1. The nanowires were grown to the out-of-plane direction from the substrate and well-spaced each other. The one-dimensional nanowire growth is due to the preferential [0001]-directed crystal growth of ZnO.[17-20] The nanowire surfaces were microscopically smooth, and the averaged nanowire diameter was ca. 120 nm for ZnO nanowires and ca. 150 nm for ZnO/ZrO_2 nanowires and ZnO/TiO_2 nanowires. The nanowire length was constant to be ca. 11 μm for the three nanowire samples. The EDS elemental mappings in Figure 1G-I and Figure S2 show that the shell layers were well-coated onto the core nanowires with ca. 15 nm thickness. Note that the Zn atom diffusion into the shell layer was negligible (Figure 1J,K). As such, the core-shell metal oxide nanowire

arrays were successfully constructed while maintaining their morphology, which offers a reliable platform for investigating a material dependence on the molecule-to-surface interaction.

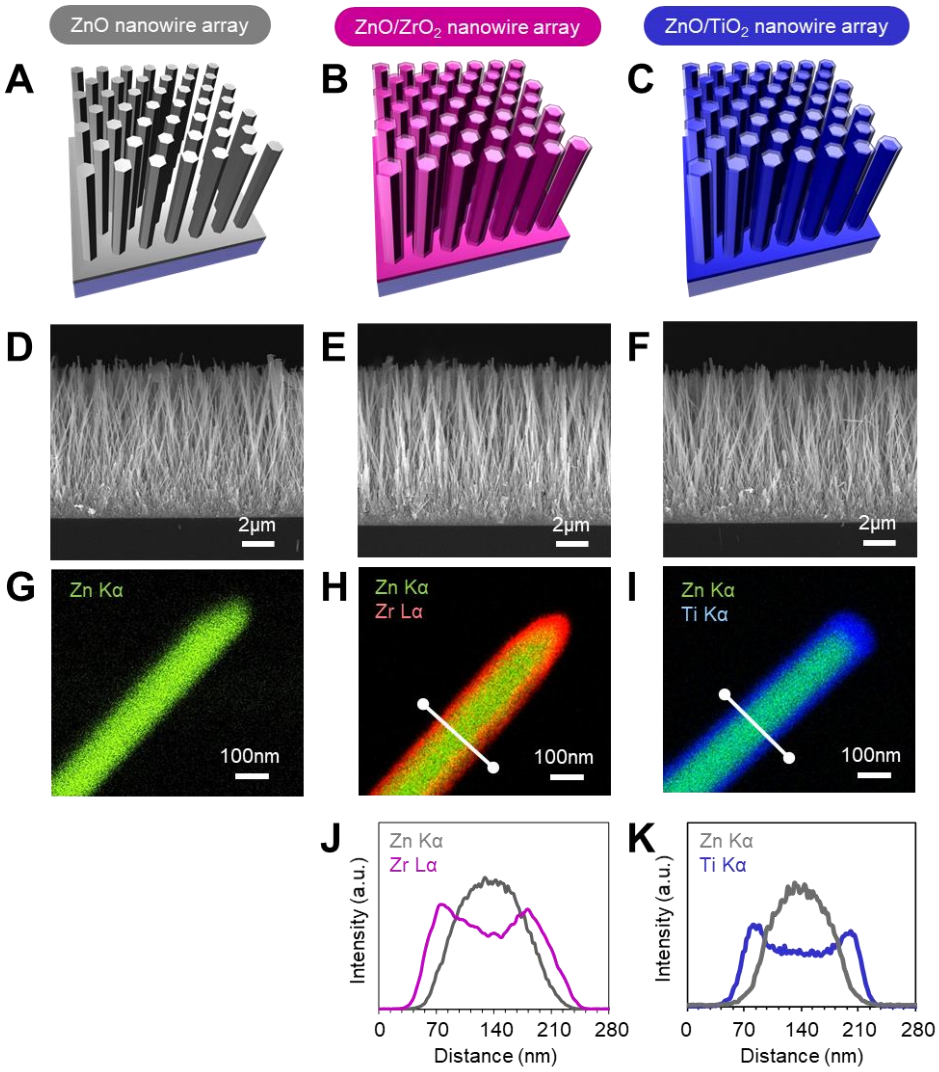

Figure 1. (A-C) Schematic images, (D-F) cross-sectional SEM images, (G-I) EDS elemental mappings and (J,K) elemental line profiles of (A,D,G) ZnO nanowires, (B,E,H,J) ZnO/ZrO_2 nanowires and (C,F,I,K) ZnO/TiO_2 nanowires. For EDS, Zn Kα, Zr Lα and Ti Kα were used.

Next, we characterized the chemical states of metal cations which may affect the molecule-to-surface interactions.[24-26] Figure 2A-C show XPS spectra of the surface metal cations for the three nanowire samples (Zn 3p, Zr 3d and Ti 3p). The binding energy (B.E.) values of the observed peaks were respectively 1021.6 eV for Zn $3p_{3/2}$, 181.8 eV for Zr $3d_{5/2}$ and 458.4 eV for Ti $3p_{3/2}$, indicating that the major valence states of metal cations were Zn^{2+}, Zr^{4+} and Ti^{4+} on the three nanowire samples.[27,28] Figure 2D-F show O1s XPS spectra for the three nanowire samples. In addition to the peaks associated with the lattice oxygen ($O_{lattice}$, B.E.~529.2-530.1 eV), those associated with the surface hydroxyl group (-OH) (O_{OH}, B.E.~531.2-531.4 eV) were observed.[12,29-30] The peak area ratio of $O_{OH}/O_{lattice}$ was 1.13, 0.63 and 0.48 for ZnO nanowires, ZnO/ZrO_2 nanowires and ZnO/TiO_2 nanowires, respectively (Figure 2G) These results showed that more Lewis acid sites (i.e. exposed metal cation sites) exist on ZnO/TiO_2 nanowires and more Brønsted acid sites (i.e. hydroxyl group sites) exist on the ZnO nanowires.

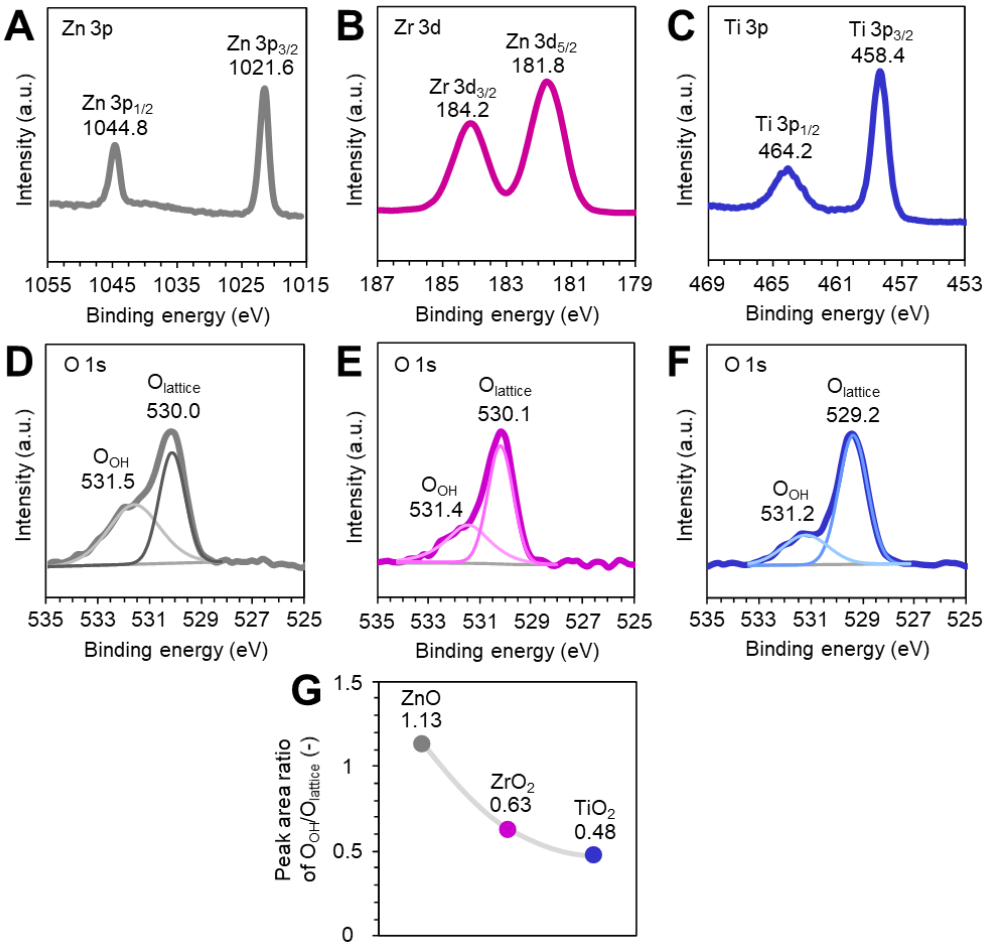

Figure 2. (A-F) XPS spectra of (A,D) ZnO nanowires ((A) Zn 3p, (D) O 1s), (B,E) ZnO/ZrO_2 nanowires ((B) Zr 3d, (E) O 1s) and (C,F) ZnO/TiO_2 nanowires ((C) Ti 3p, (F) O 1s). (G) Peak area ratio of $O_{OH}/O_{lattice}$ of the three tested nanowire array.

Using the nanowire arrays, we examined the spectroscopic analysis for the surface adsorption behaviors of 2-nonanone. 2-nonanone (C9 ketone) is known to be a volatile biomarker of *Pseudomonas aeruginosa* in cystic fibrosis and a thermally derived off-flavor compound in milk.[15,16] Figure 3 shows FTIR spectra of the 2-nonanone adsorbed nanowire samples, where they cover the alkyl region (2800-3000 cm^{-1}: Figure 3A) and the carbonyl/carboxylate region (1500-1800 cm^{-1}: Figure 3B), respectively. As a reference, the spectrum of liquid concentrate of 2-nonanone is also shown. In Figure 3A, four peaks assigned as $\nu_{as}(CH_3)$, $\nu_{as}(CH_2)$, $\nu_s(CH_3)$ and $\nu_s(CH_2)$ were observed.[31]

Since the alkyl group were not reacted through the adsorption event, they were utilized as indicator for evaluating the adsorption amount of 2-nonanone. The nanowire length dependence on molecular adsorption amount indicated that the 2-nonanone was well-diffused into the nanowire array (Figure 4). Here, the peak area of alkyl group was compared among the three nanowire samples (Figure 3C). The results showed that the adsorption amounts of 2-nonanone were almost comparable between the three samples. On the other hand, in Figure 3B, two peaks including the sharp and the broad ones were observed at around 1650-1730 cm^{-1} and 1500-1620 cm^{-1}. These peaks are respectively assigned as ν(C=O) and ν(COO), of which the molecules are coordinated at metal cations (Lewis acid sites).[12,32-34] Note that any other peaks associated with the coordination at Brønsted acid sites and those of dimer were not observable unlike our previous study of nonanal (C9 aldehyde) adsorption on ZnO nanowires.[5] The presence of ν(COO) peaks indicated that the adsorbed 2-nonanone was partially oxidized. For the ν(C=O) peaks, the peak shift in a comparison with liquid concentrate was consistently seen for the three nanowire samples. We found that both the ν(COO) peak intensity and the degree of peak shift for the ν(C=O) peak tended to be larger in the order of ZnO < ZrO_2 < TiO_2 (Figure 3D). The results implied that the molecule-to-surface interaction becomes stronger in this order, and it was coincident with the Lewis acidity of metal cations (Lewis acidity: Zn^{2+} < Zr^{4+} < Ti^{4+}).[35] This implication was well supported by the results of TPD measurements in Figure 5, of which the desorption temperatures of adsorbed 2-nonanone on the three nanowire samples increased in the above order. Thus, these results highlighted that the material dependence on the molecule-to-surface interaction was successfully observed using the core-shell nanowire array.

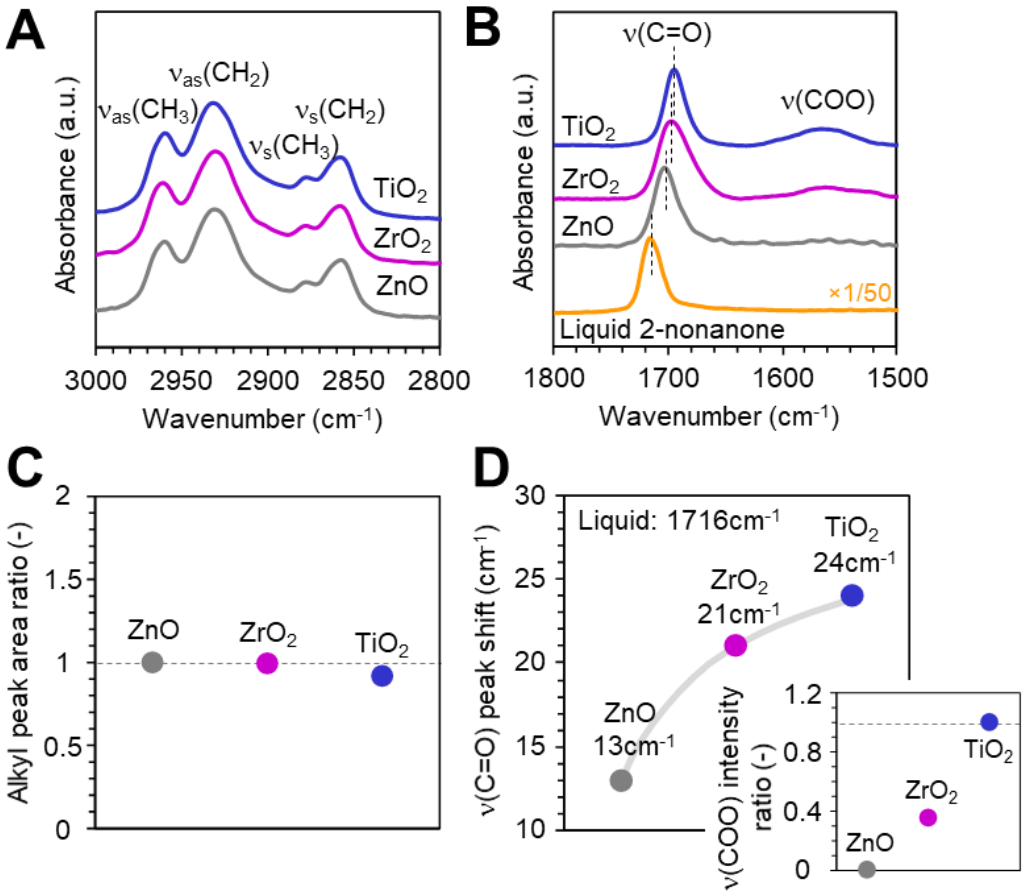

Figure. 3 (A,B) FTIR spectra of 2-nonanone adsorbed metal oxide nanowire array structures at (A) alkyl region and (B) carbonyl region. For comparison, a spectrum of liquid concentrate of 2-nonanone is also shown in (B). (C) Alkyl peak area ratio between the three nanowire samples. (D) Degree of peak shift at ν(C=O) compared with liquid concentrate. Inset shows peak intensity ratio of ν(COO) between the three nanowire samples.

Here we discuss why the 2-nonanone adsorption amounts were comparable between the three nanowire samples with different metal oxide species (Figure 3C). In principle, the molecular adsorption amount might be affected by various factors including the surface area, the adsorption site density, the coordination number and/or the Lewis

acidity of metal cations. Note that the influence of surface area difference was not considerable in our nanowire array as confirmed by the ZnO/ZnO core-shell nanowire array (Figure S3). The results in Figure 3 implied the importance of Lewis acidity and/or Lewis acid site density on the adsorption of 2-nonanone. Since the exposed Lewis acid site density becomes higher in the order of $ZnO<ZrO_2<TiO_2$ (Figure 2G), we assumed that the effect of adsorption site density was compensated by the other competing factors. In order to reveal the mechanism, we performed the thermal annealing of ZnO nanowires in vacuum condition to increase the Lewis acid site density by removing the surface hydroxyl group,[12] and examined its impact on the molecular adsorption amount. On contrary to our expectation, the adsorption amount only slightly increased by annealing, indicating that the adsorption site density doesn't significantly affect the adsorption amount of 2-nonanone (Figure 6 and Figure S4). These results implied that the adsorbed molecules were plausibly saturated at nanowire surface. Since 2-nonanone (C9 ketone) is sterically large molecule, its adsorption at the metal cation site is supposed to be competitive among the molecules even if the sufficient adsorption site density is available. Such obtained implications would be beneficial to design the molecular sensing device, i.e. both a sufficient sensing response and a fast recovery are expected in 2-nonanone sensing by employing the metal oxide nanowires composed of metal cation species with relatively weak Lewis acidity.

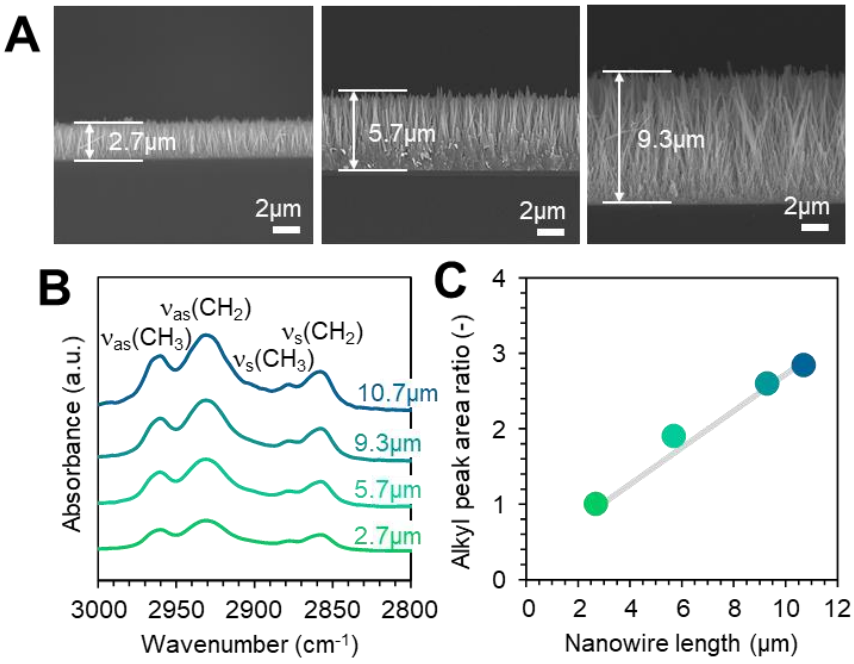

Figure. 4 (A) Cross-sectional SEM images of ZnO nanowire arrays with different nanowire length. (B) FTIR spectra (at alkyl region) of ZnO nanowire arrays with different nanowire length. (C) Alkyl peak area ratio when varying the nanowire length.

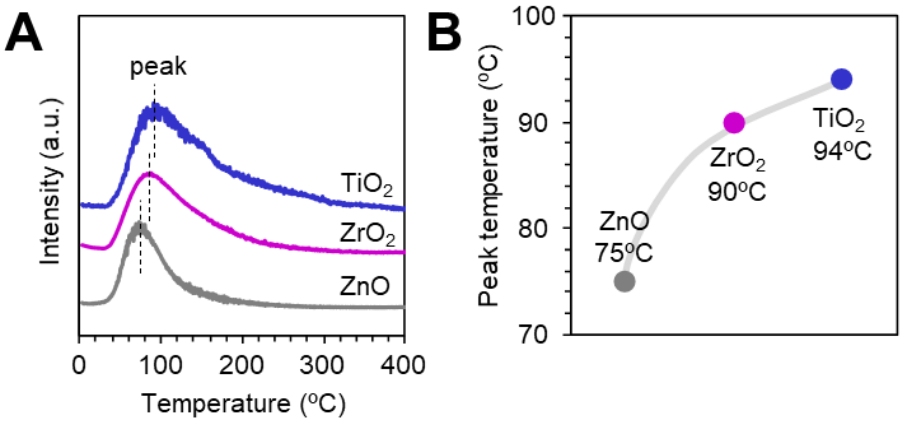

Figure 5. (A) TPD profiles of 2-nonanone adsorbed on the three nanowire samples (at *m*/*z* 58). (B) Peak temperatures of TPD profiles in (A).

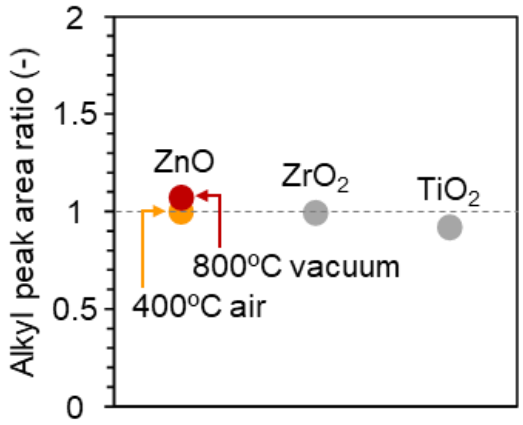

Figure 6. Alkyl peak area ratio when varying the annealing condition. As comparisons, the data of ZnO/ZrO_2 core-shell nanowires and ZnO/TiO_2 core-shell nanowires are also shown.

4.5 Conclusion

In conclusion, we investigated the material dependence on the surface adsorption behaviors of 2-nonanone using a core-shell metal oxide nanowire array. The core-shell nanowire array allowed us to alter the surface metal oxide species while maintaining the nanowire morphology. Spectroscopic and spectrometric analyses revealed that the Lewis acidity of meal cations give a strong impact on the bonding strength of 2-nonanone but not on the adsorption amount. The obtained implications would be beneficial for designing the performance of various metal oxide nanowire-based applications. Thus, this study highlights that the core-shell nanowire array provides a foundation for understanding and designing the molecule-to-surface interactions on various applications.

4.6 References

(1) Z. Zhou, C. Lan, R. Wei and J. C. Ho, *J. Mater. Chem. C* **2019**, *7*, 202.

(2) G. Zhang, H. Zeng, J. Liu, K. Nagashima, T. Takahashi, T. Hosomi, W. Tanaka and T. Yanagida, *Analyst* **2021**, *146*, 6684.

(3) H. C. Song, G. R. Lee, K. Jeon, H. Lee, S. W. Lee, Y. S. Jung and J. Y. Park, *ACS Nano* **2020**, *14*, 8335.

(4) D. Wang, B. Zhu, X. He, Z. Zhu, G. Hutchins, P. Xu and W.-N. Wang, *Environ. Sci.: Nano* **2018**, *5*, 1096.

(5) Y. Ren, W. Xie, Y. Li, J. Ma, J. Li, Y. Liu, Y. Zou and Y. Deng, *ACS Cent. Sci.* 2021, **7**, 1885-1897.

(6) P. Bandyopadhyay, R. Jana, K. Bhattacharyya, O. I. Lebedev, U. Dutta, U. Sarkar, A. Detta and M. M. Seikh, *New J. Chem.* **2019**, *43*, 16621.

(7) J. Wang, Z. Li and Z. Gu, *Sens. Actuators Rep.* **2021**, *3*, 100029.

(8) G. Zhang, T. Hosomi, W. Mizukami, J. Liu, K. Nagashima, T. Takahashi, M. Kanai, T. Sugiyama, T. Yasui, Y. Aoki, Y. Baba, J. C Ho and T. Yanagida, *J. Mater. Chem. A* **2021**, *9*, 5815.

(9) H. Zeng, G. Zhang, K. Nagashima, T. Takahashi, T. Hosomi and T. Yanagida, *Chemosensors* **2021**, *9*, 41.

(10) A. Klamchuen, M. Suzuki, K. Nagashima, H. Yoshida, M. Kanai, F. W. Zhuge, Y. He, G. Meng, S. Kai, S. Takeda, T. Kawai and T. Yanagida, *Nano Lett.* **2015**, *15*, 6406.

(11) J. Liu, K. Nagashima, H. Yamashita, W. Mizukami, J. Uzuhashi, T. Hosomi, M. Kanai, X. Zhao, Y. Miura, G. Zhang, T. Takahashi, M. Suzuki, D. Sakai, B. Samransuksamer, Y. He, T. Ohkubo, T. Yasui, Y. Aoki, J. C. Ho, Y. Baba and

T. Yanagida, *Commun. Mater.* **2020**, *1*, 58.

(12) C. Wang, T. Hosomi, K. Nagashima, T. Takahashi, G. Zhang, M. Kanai, H. Zeng, W. Mizukami, N. Shioya, T. Shimoaka, T. Tamaoka, H. Yoshida, S. Takeda, T. Yasui, Y. Baba, Y. Aoki, J. Terao, T. Hasegawa and T. Yanagida, *Nano Lett.* **2019**, *19*, 2443.

(13) C. Wang, T. Hosomi, K. Nagashima, T. Takahashi, G. Zhang, M. Kanai, H. Yoshida and T. Yanagida, *ACS Appl. Mater. Interfaces* **2020**, *12*, 44265.

(14) J. Liu, K. Nagashima, Y. Nagamatsu, T. Hosomi, H. Saito, C. Wang, W. Mizukami, G. Zhang, B. Samransuksamer, T. Takahashi, M. Kanai, T. Yasui, Y. Baba and T. Yanagida, *Chem. Sci.* **2021**, *12*, 5073.

(15) S. U. Savelev, J. D. Perry, S. J. Bourke, H. Jary, R. Taylor, A. J. Fisher, P. A. Corris, M. Petrie and A. D. Soyza, *Lett. Appl. Microbiol.* **2011**, *52*, 610.

(16) P.A.Vazquez-Landaverde, G. Velazquez, J. A. Torres and M. C. Qian, *J. Dairy Sci.* **2011**, *88*, 3764.

(17) Y. He, T. Yanagida, K. Nagashima, F. W. Zhuge, G. Meng, B. Xu, A. Klamchuen, S. Rahong, M. Kanai, X. M. Li, M. Suzuki, S. Kai and T. Kawai, *J. Phys. Chem. C* **2013**, *117*, 1197.

(18) D. Sakai, K. Nagashima, H. Yoshida, M. Kanai, Y. He, G. Zhang, X. Zhao, T. Takahashi, T. Yasui, T. Hosomi, Y. Uchida, S. Takeda, Y. Baba and T. Yanagida, *Sci. Rep.* **2019**, *9*, 14160.

(19) X. Zhao, K. Nagashima, G. Zhang, T. Hosomi, H. Yoshida, Y. Akihiro, M. Kanai, W. Mizukami, Z. Zhu, T. Takahashi, M. Suzuki, B. Samransuksamer, G. Meng, T. Yasui, Y. Aoki, Y. Baba and T. Yanagida, *Nano Lett.* **2020**, *20*, 599.

(20) Q. Liu, T. Yasui, K. Nagashima, T. Yanagida, M. Hara, M. Horiuchi, Z. Zhu, H. Takahashi, T. Shimada, A. Arima and Y. Baba, *J. Phys. Chem. C* **2020**, 124,

20563.

(21) K. Nagashima, T. Yanagida, H. Tanaka S. Seki, A. Saeki, S. Tagawa and T. Kawai, *J. Am. Chem. Soc.* **2008**, *130*, 5378.

(22) K. Nagashima, T. Yanagida, K. Oka, M. Kanai, A. Klamchuen, J.-S. Kim, B. H. Park and T. Kawai, *Nano Lett.* **2011**, *11*, 2114.

(23) K. Nagashima, T. Yanagida, K. Oka, M. Taniguchi, T. Kawai, J.-S. Kim and B. H. Park, *Nano Lett.* **2010**, *10*, 1359.

(24) N. C. Jeong, J. S. Lee, E. L. Tae, Y. J. Lee and K. B. Yoon, *Angew. Chem., Int. Ed.*, **2008**, *47*, 10128.

(25) D. Degler, U. Weimar and N. Barsan, *ACS Sens.*, **2019**, 4, 2228.

(26) O. Lupan, V. Postica, J. Gröttrup, A. K. Mishra, N. H. de Leeuw, J. F. C. Carreira, J. Rodrigues, N. B. Sedrine, M. R. Correia, T. Monteiro, V. Cretu, I. Tiginyanu, D. Smazna, Y. K. Mishra and R. Adelung, *ACS Appl. Mater. Interfaces*, **2017**, *9*, 4084.

(27) M. C. Biesinger, L. W. M. Lau, A. R. Gerson and R. S. C. Smart, *Appl. Surf. Sci.* **2010**, *257*, 887.

(28) D. D. Sarma and C. N. R. Rao, *J. Electron Spectrosc. Relat. Phenom.* **1980**, *20*, 25.

(29) J.-K. An, N.-K. Chung, J.-T. Kim, S.-H. Hahm, G. Lee, S. B. Lee, T. Lee, I.-S. Park and J.-Y. Yun, *Materials* **2018**, *11*, 386.

(30) C. Fan, C. Chen, J. Wang, X. Fu, Z. Ren, G. Qian and Z. Wang, *Sci. Rep.* **2015**, *5*, 11712.

(31) P. Larkin, 2011. *Infrared and Raman spectroscopy; principles and spectral interpretation.* Amsterdam Elsevier.

(32) M. D. Hernández-Alonso, I. Tejedor-Tejedor, J. M. Coronado and M. A.

Anderson, *Appl. Catal. B* **2011**, *101*, 283.

(33) T. Komanoya, K. Nakajima, M. Kitano and M. Hara, *J. Phys. Chem. C* **2015**, *119*, 26540.

(34) Z. Topalian, B. I. Stefanov, C. G. Granqvist and L. Österlund, *J. Catal.* **2013**, *307*, 265.

(35) O. C. Gagné and C. H. Hawthorne, *Acta Crystallogr., Sect. B: Struct. Sci., Cryst. Eng. Mater.* **2017**, *73*, 956.

4.7 Supporting Information

4.7.1 Sample Characterization Details

The morphology, the composition and the chemical state of the prepared nanowire arrays were characterized by field emission scanning electron microscope (FESEM, JEOL JSM-7610F) equipped with energy dispersive x-ray spectroscopy (EDS) mode and scanning transmission electron microscopy (STEM) mode at accelerating voltage of 15-30 kV, x-ray photoemission spectroscopy (XPS, Kratos AXIS-ULTRA with Al Kα radiation source (12 kV, 5 mA, monochromator) and ULVAC PHI PHI5000 VersaProbe with Al Kα radiation source (15 kV, 25 W, monochromator)). For XPS, the binding energies were corrected at C 1s peak.

Fourier transform infrared spectroscopy (FTIR, Thermo Fisher Scientific Nicolet iS50) equipped with MCT (HgCdTe) detector was employed to characterize the chemical states of adsorbed molecules on the sample surface. Prior to the measurements, the analyte molecule was first adsorbed on the sample surface. Samples with the size of 10 mm×20 mm were suspended in 50 mL vial bottle filled with saturated 2-nonanone and kept for 10 min. Then the samples were transferred to FTIR measurement system. The measurements were performed at room temperature.

For analysing the bonding strength of surface-adsorbed molecules, the analyte molecules were first adsorbed on the sample surface. Samples with the size of 2 mm×20 mm were suspended in 20 mL vial bottle filled with saturated 2-nonanone and kept for 60 s. Then the samples were transferred to gas chromatograph mass spectrometry (GCMS, Shimadzu GCMS-QP2020 Ultra). The temperature programmed desorption (TPD) measurements of adsorbed molecules were conducted using a capillary column (length of 1 m and internal diameter of 0.1 mm) without stationary phases. The samples

were heated at the inlet port from 35 to 500 ºC at a rate of 0.5 ºC/s using a multi-shot pyrolyzer (Frontier Lab EGA-PY-3030D).

4.7.2 Conditions of desorbed gas analyses

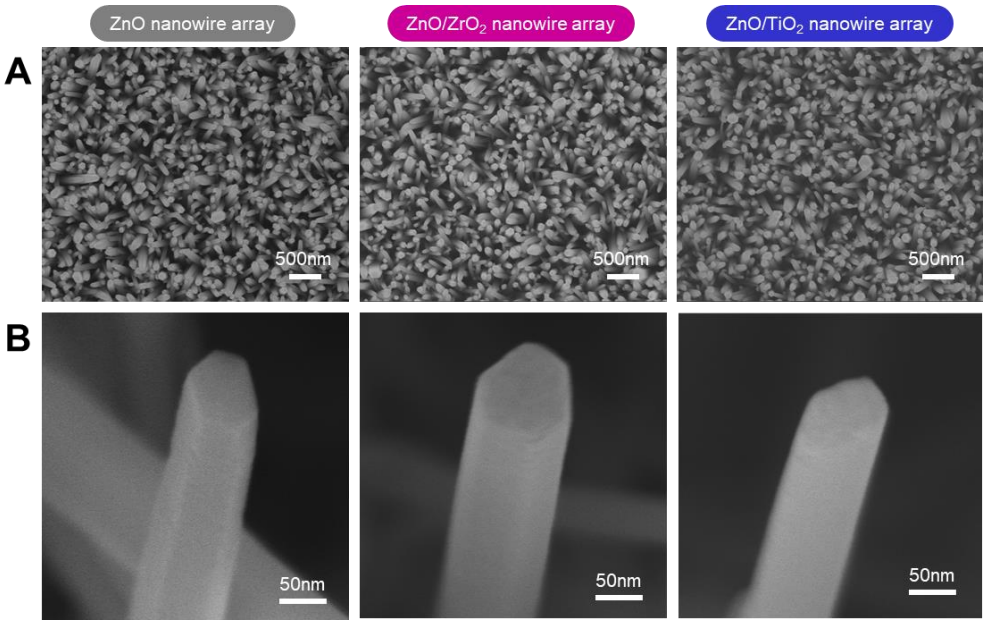

Fig. S1. (A) Top-view SEM images and (B) magnified SEM images of nanowire array structures: ZnO nanowires (left), ZnO/ZrO_2 nanowires (middle) and ZnO/TiO_2 nanowires (right).

We characterized the inter-nanowire spacing and the surface morphology of nanowire array structures. Top-view SEM images in Fig. S1A and magnified SEM images in Fig. S1B show that the nanowires were well-spaced, and the nanowire surfaces were microscopically smooth even after depositing the shell layers (ZrO_2 and TiO_2 layers). These results indicated that the reliable analytical platform to investigate the material dependence on the molecule-to-surface interaction was successfully constructed.

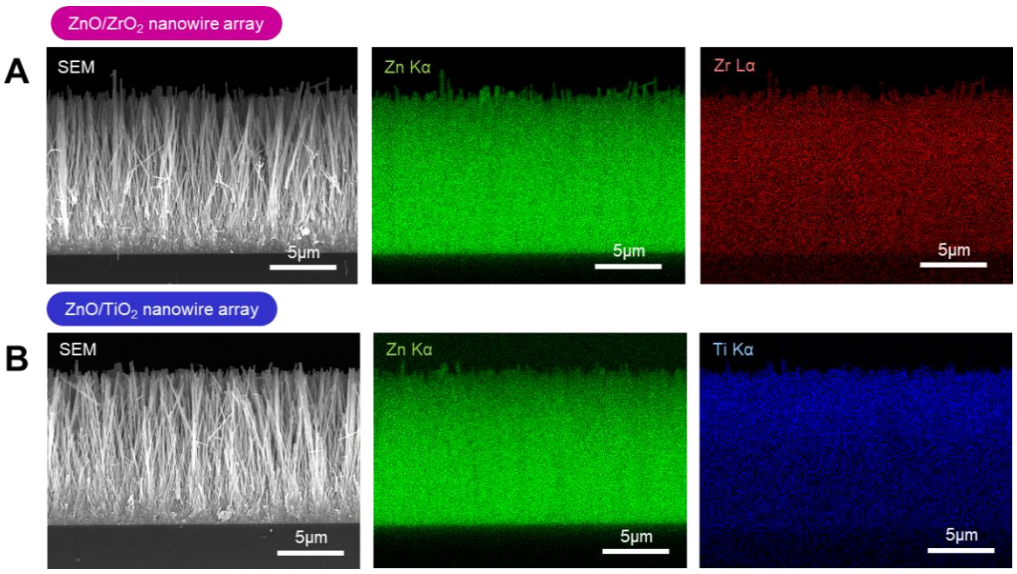

Figure S2. SEM images and EDS elemental mappings of nanowire arrays with cross-sectional view. (A) ZnO/ZrO_2 core-shell nanowires and (B) ZnO/TiO_2 core-shell nanowires, respectively. For elemental mapping, Zn Kα, Zr Lα and Ti Kα were used.

We evaluated the shell layer deposition of ZnO/ZrO_2 core-shell nanowires and ZnO/TiO_2 core-shell nanowires by EDS elemental mappings with cross-sectional view. The well-deposited shell layers on nanowire array were confirmed.

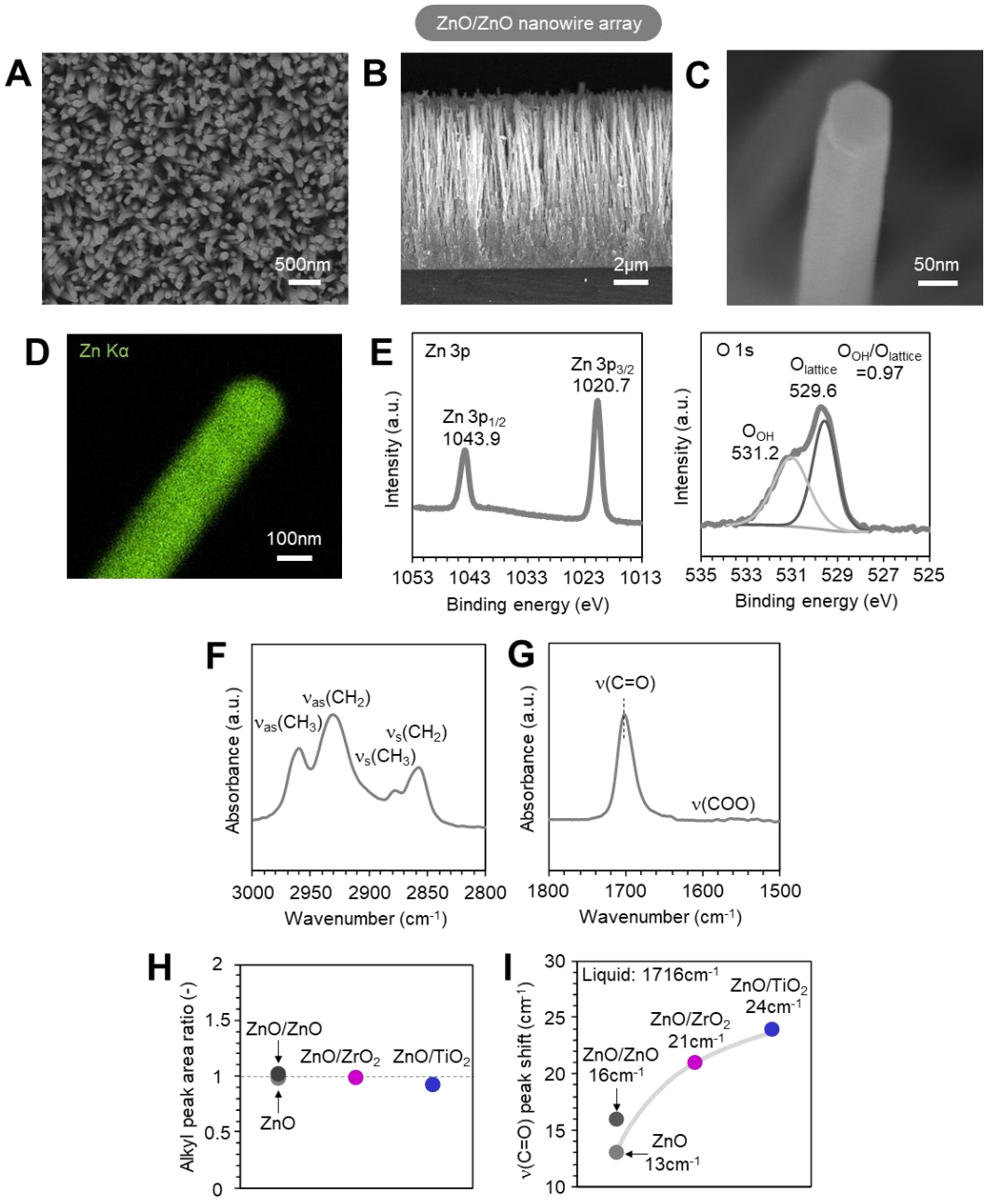

Figure S3. (A) Top view SEM image, (B) cross-sectional SEM image, (C) magnified SEM image, (D) EDS elemental mapping, (E) XPS spectra (Zn3p and O1s) of ZnO/ZnO core-shell nanowires. (F,G) FTIR spectra of 2-nonanone adsorbed ZnO/ZnO core-shell nanowire array at (F) alkyl region and (G) carbonyl region. (H) Alkyl peak area ratio compared with other nanowire samples. (I) Degree of peak shift at ν(C=O)

compared with liquid concentrate. For comparison, the results of other nanowire samples are also shown.

We constructed ZnO/ZnO core-shell nanowires to investigate the impact of surface area difference between the ZnO nanowires and the other core-shell nanowires (ZnO/ZrO_2 nanowires and ZnO/TiO_2 nanowires) on the adsorption behaviors of 2-nonanone. This is because the surface area of core-shell nanowires (ca. 150 nm diameter) must be 1.25 times larger than that of ZnO nanowires (ca. 120 nm diameter). By carefully controlling the deposition rate of ZnO shell layer, we successfully fabricated the ZnO/ZnO core-shell nanowires with almost same diameter as the other core-shell nanowires. As well as the other core-shell nanowires, the smooth nanowire surface was confirmed. XPS data showed that the $O_{OH}/O_{lattice}$ ratio of ZnO/ZnO core-shell nanowires was higher than that of ZnO nanowires. From the FTIR results, we found that the influence of surface area difference on the adsorption amount of 2-nonanone was not considerable in this study, while the metal cation dependent boning strength was also seen in ZnO/ZnO nanowires.

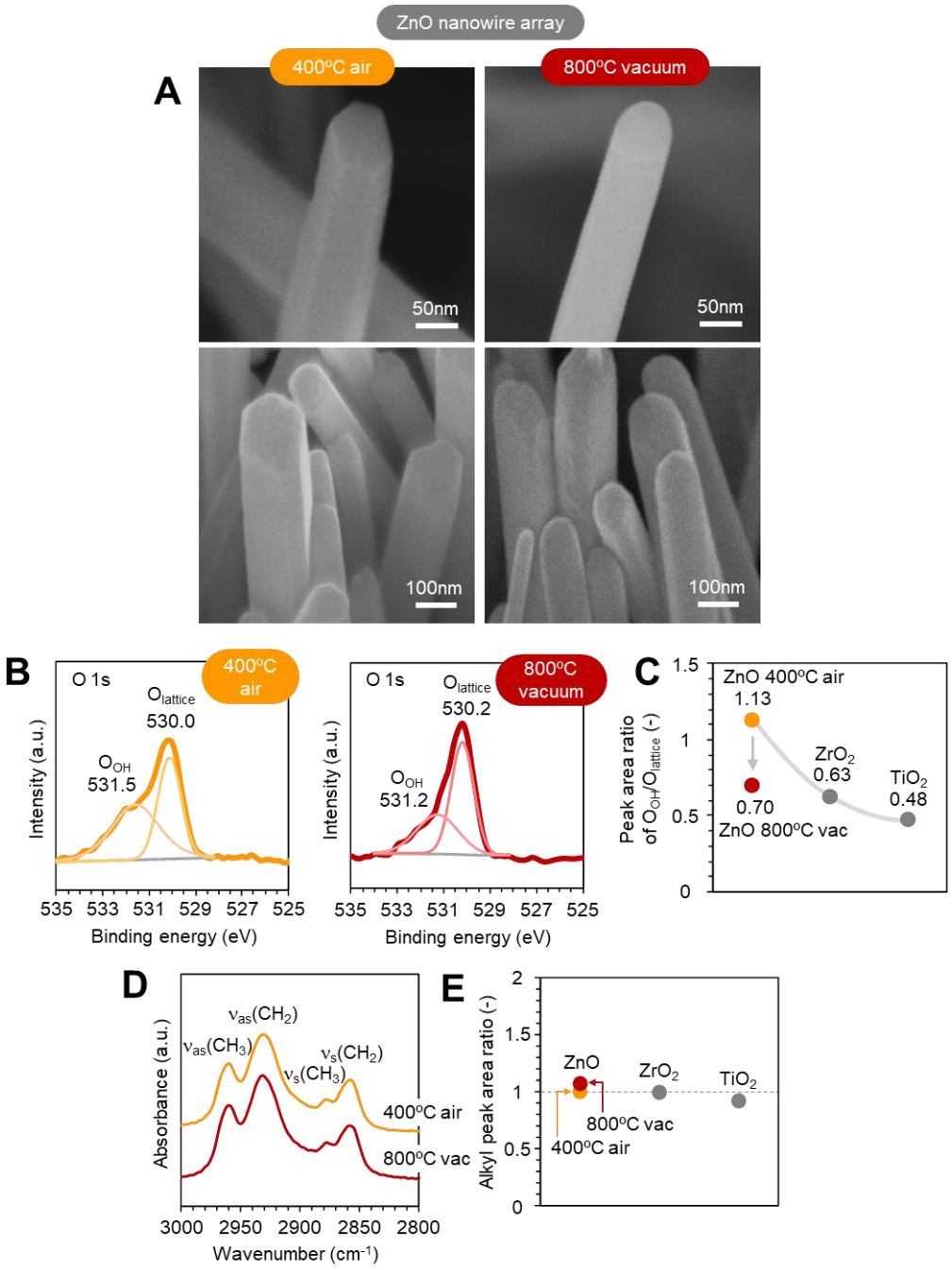

Figure S4. (A) SEM images and (B) O1s XPS spectra of ZnO nanowires when annealing at 400 ºC in air (left) and 800 ºC in vacuum (right). (C) Peak area ratio of $O_{OH}/O_{lattice}$ of the tested nanowire samples. (D) FTIR spectra (at alkyl region) of ZnO nanowire arrays with different annealing conditions. (E) Alkyl peak area ratio when

varying the annealing condition. For comparison, the data of ZnO/ZrO_2 core-shell nanowires and ZnO/TiO_2 core-shell nanowires are also shown in (C) and (E).

To investigate the effect of adsorption site density on the molecular adsorption amount on the nanowire array, we performed the thermal annealing of ZnO nanowires. Our previous study demonstrated that the ratio of surface hydroxyl group (i.e. Brønsted acid sites) tended to decrease while the metal cation sites (i.e. Lewis acid sites) tended to increase when annealing the ZnO nanowires at higher temperature and/or in vacuum condition [Ref 1]. Therefore, we annealed the ZnO nanowires at 800 ºC in vacuum condition and examined its influence on the adsorption amount of 2-nonanone. The nanowire morphology was maintained, and the nanowire surface was kept smooth even after the annealing. XPS data showed that ratio of surface hydroxyl group (i.e. Brønsted acid sites) decreased (the metal cation sites (i.e. Lewis acid sites) increased) by the annealing as consistent with our previous study. The FTIR result showed that no significant variation in the adsorption amount was observed even after the annealing process.

[Ref 1] C. Wang, T. Hosomi, K. Nagashima, T. Takahashi, G. Zhang, M. Kanai, H. Zeng, W. Mizukami, N. Shioya, T. Shimoaka, T. Tamaoka, H. Yoshida, S. Takeda, T. Yasui, Y. Baba, Y. Aoki, J. Terao, T. Hasegawa and T. Yanagida, *Nano Lett.* 2019, **19**, 2443-2449.

CHAPTER V

IN-SITU FABRICATION OF HYDROTHERMALLY GROWN ZNO BRIDGING NANOSENSORS

5.1 Abstract

In-situ fabrication of well-defined bridging nanostructures is an interesting and unique approach to three-dimensionally design nanosensor structures, which are hardly attainable by other methods. Here, we demonstrate the significant effect of edge-topological regulation on *in-situ* fabrication of hydrothermally grown ZnO bridging nanosensors. When employing seed layers with a sharp edge, which is a well-defined structure in conventional lithography, the bridging angle distribution of fabricated nanosensors between two opposing electrodes was random and could not be well defined. We found that such conventionally well-defined shape edge structure is detrimental for *in-situ* fabrication of well-defined bridging nanosensors due to the inherent uncontrollability of growth directions at edges. We propose an edge-less seed layer structure using two-layers resist methods to define the growth direction for *in-situ* fabrication of bridging nanosensors. Bridging nanosensors fabricated using such edge-less seed layer structures exhibited much superior directional controllability for *in-situ* fabrication. Furthermore, the well-defined bridging nanosensors not only substantially suppressed the unintentional variations of electrical resistances between electrodes, but also significantly enhanced the sensing responses for NO_2 with the smaller standard deviation and the lower limitation of detection when compared with those using conventional shape edge seed layers.

Keywords*:* *In-situ* fabrication, Bridging nanostructures, Edge-topological regulation, Hydrothermal growth, Sensors

5.2 Introduction

Manipulating and tailoring three-dimensionally (3D) nanostructures using *in-situ* fabrication of bottom up methods is one of major goals in nanotechnology.[1-5] Such well-defined 3D nanostructures are promising candidates as novel sensor structures, which had not been fabricable by conventional methodologies.[6-10] The *in-situ* fabrication technique is particularly interesting to define the spatial location of nanosensors on a patterned substrate with the resolution of current lithographic technology.[11-13] This fruitful combination of top-down lithographic technology and bottom-up crystal growth technology in *in-situ* fabrication of nanosensors offers an important foundation to construct highly integrated nanosensors via advanced semiconductor technologies.[14-16] Among various 3D nanosensors, a bridging nanostructure between two opposing electrodes is a promising sensor structure, because a contact point between two nanostructures plays an essential role on sensing characteristics of various gases.[17-20] To the best of our knowledge, such *in-situ* fabrication of bridging nanosensors was first demonstrated by Qi and Dai *et al*. using carbon nanotubes for NH_3 and NO_2 sensing.[21] *In-situ* fabrication of bridging Si nanowire sensors for HCl and NH_3 was reported by Kamins *et al*.[22] Anh *et al*. have reported bridging nanosensors of defect-controlled ZnO nanowires for NO_2 detection.[23] Mo-doped ZnO nanowire network sensors with the H_2S selectivity was demonstrated.[24] *In-situ* fabrication of bridging SnO_2 nanowire sensors for liquefied petroleum gas and NH_3 was studied by Thong *et al*.[25] Bridging nanosensor of *p*-type CuO nanowire for CO detection was proposed by Steinhauer *et al*.[26] Bridging nanosensors of GaN nanowires[27] and InAs nanowires[28] were also demonstrated for NO_2 sensing. Although these studies reveal that *in-situ* fabrication of bridging nanosensors is a powerful tool to design three-dimensionally novel nanosensors for various sensing materials, the structural controllability of bridging nanostructures during *in-situ*

fabrication is still rather poor, especially the nano-bridging process is highly a stochastic event, which will cause severe problems when constructing highly integrated nanosensors with high reliability, uniformity and reproducibility required for nanoelectronics.

This study reports the significant effect of edge-topological regulation on *in-situ* fabrication of hydrothermally grown ZnO bridging nanostructures. We found that conventionally well-defined shape edge structure is highly detrimental as a seed layer for *in-situ* fabrication of well-defined bridging nanosensors due to the inherent uncontrollability at edges. Using newly proposed edge-less seed layer structures, we successfully fabricated well-defined bridging nanosensors with much superior electrical properties and gas sensing properties when compared with those using conventional shape edge seed structures.

5.3 Experimental Section

Fabrication of Bridging Nanosensors. Bridging nanosensors were fabricated on photo-lithography patterned Si (100) substrate with a 100 nm thick SiO_2 coated layer. Positive type photoresist (AZP1350) was employed as conventional one-layer photoresist lithography to fabricate bridging nanosensors. Spin-coating of photoresist was performed on a 1cm*1cm size of Si substrate at 4000 rpm for 1min. Followed by a thermal baking procedure at 190°C for 5 min to fully solidification, the patterning of photoresist was performed by photo-lithography (HEIDELBERG instrument □PG 101 UOW1) at energy of 40 mW. Then, Pt electrode was deposited by radio frequency (RF) sputtering at a power of 50 W and an Ar pressure of 0.3 Pa with the thickness of 100 nm. Subsequently, ZnO seed-layer with the thickness of 50 nm (RF at 50 W) was

deposited on pattered substrates just after sputtering Ti thin-layer (~5nm, RF at 50W) on Pt to enhance the adhesion between ZnO seed layer and electrodes. After a lift-off process using N, N-dimethylformamide (DMF) and a rinse process in flowing water, the substrates are ready for 3D bridging fabrication process. To overcome the sharp-edge issues, we propose a two-layer photoresist method, which employs two laminated resists. Spin-coating positive type photoresist (LOR3B) was performed on 1cm*1cm size of Si substrate at 3000 rpm for 1min, thermal baking procedure at 100°C for 2 min for solidification. Subsequently, conventional lithography was performed. The gap size of patterned substrate was ranged from 2□10□m. ZnO bridging nanosensors on patterned seed-layer substrates was fomred by hydrothermal method. The substrate was immersed into a 150 mL aqueous solution containing 25 mM zinc nitrate hexahydrate ($Zn(NO_3)_2 \cdot 6H_2O$, Wako 99.0%) and 25 mM hexamethylenetetramine (HMTA, $(CH_2)_6N_4$ Wako 99.0%), 2.5 mM polyethylenimine (number-average MW 1800, 50 wt % in H_2O) and ammonia ($NH_3 \cdot 6H_2O$, 1 mL, 28% in H_2O). The ZnO nanowires were grown with keeping the solution at 95°C for a serious of growth time in an oven with constant growth temperature. After the growth, the substrate was taken out from the solution and finally rinsed with water. Twelve devices were fabricated for each condition to obtain statistical data.

Characterization. The morphology of fabricated bridging nanosensors was characterized by scanning electron microscopy (SEM, JEOL JSM-7610F) at an accelerating voltage of 15 kV. Electrical property of bridging nanosensors were measured as I−V data using a semiconductor parameter analyzer (Keithley, 4200SCS) with a probe station having a temperature-controlling system. Gas sensing measurements were performed using a homemade testing system consisting of a gas supply system, a probe station with temperature control (JANIS, ST-500), and a

semiconductor analyzer (Keithley 4200SCS) used to collect the electric signal The variations of electrical signals under N_2 or NO_2 ppm were monitored by applying a voltage of 1 V to the electrodes. The sensor response was defined as R_g/Ra, where R_g and R_a are the sensor resistance when exposed to NO_2 and N_2, respectively. We statically evaluated several bridging nanosensors. Testing temperature was set to vary from room temperature to 250 °C. Electrical property and gas sensing measurements were controlled under 200°C.

5.4 Results and Discussion

Figure 1a shows the experimental procedure to fabricate bridging nanosensors using lithographically defined ZnO seed layers on Pt electrodes. The width and gap of bridging nanosensors can be arbitrarily varied. Conventional lift-off process is employed to define the patterns of electrodes and seed layers. Bridging ZnO nanosensors are then *in-situ* formed between two opposing seed layers on the substrate using hydrothermal crystal growth.[29-31]

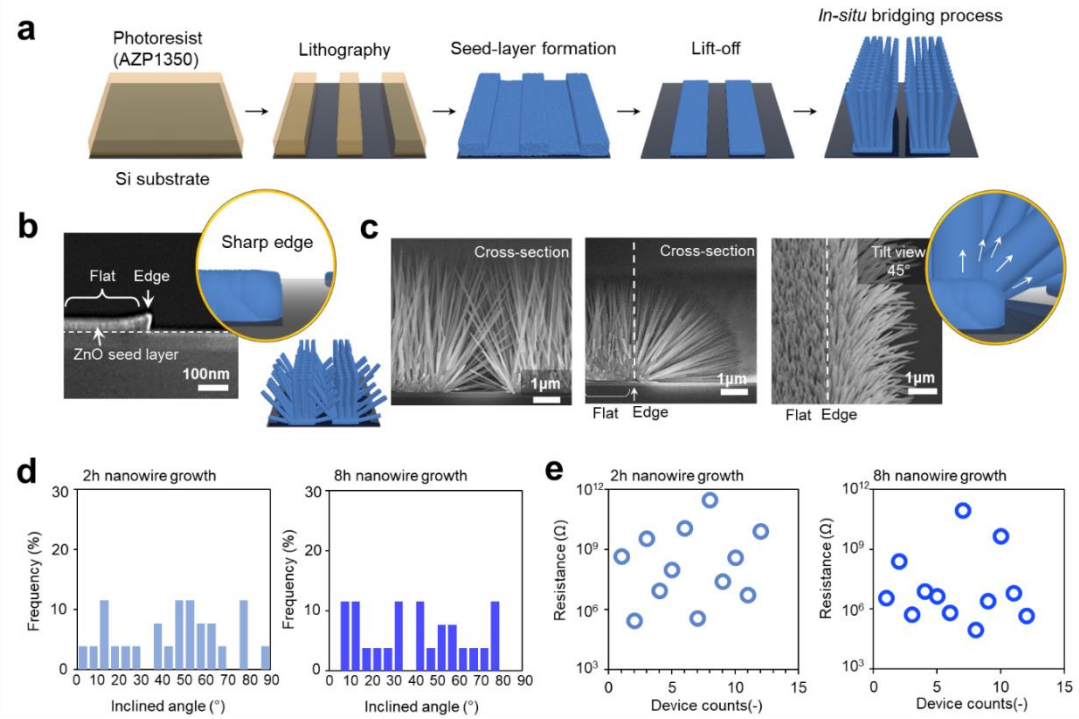

Figure 1. Bridging nanosensors fabricated from a sharp edge seed layer, and their structural and electrical properties: (a) Schematic of experimental procedure to fabricate bridging nanosensors using conventional lift-off process, (b) Cross-sectional scanning electron microscopy (SEM) images of fabricated seed layer with the well-defined sharp edge, (c) Cross-sectional and tilted top-view SEM images of fabricated bridging ZnO nanowires at edge and flat area of seed layer, (d) Bridging angle distribution between two opposing seed layers (2 hours and 8 hours nanowire growth), (e) Statistical variation of electrical resistance of fabricated nanosensors (2 hours and 8 hours nanowire growth).

The length of ZnO nanostructures can be controlled as a function of the growth time.[32,33] Figure 1b shows the cross-sectional SEM image of fabricated seed layer, showing the sharp edge defined by lithography. Figure 1c shows the scanning electron microscopy (SEM) images of bridging nanosensors fabricated. As clearly seen in the SEM images, the fabricated ZnO nanowires were significantly inclined with respect to

the vertical direction of substrate. The angle distribution of ZnO nanowires between two opposing seed layers were analyzed from the cross-sectional SEM images, showing the data in Figure 1d. The random distribution of measured angle values can be seen in the figures. Data also revealed that the inclined ZnO nanowires emerged even in the early growth stage. This random angle distribution has been consistently observed for all bridging nanosensors fabricated from a sharp edge seed layer. (Figure S1) This unintentional structural variation resulted in the gigantic variation of electrical resistances between opposing two electrodes, as shown in Figure 1e. The electrical variability is in the range of 6 orders of magnitude for 12 bridging nanosensors fabricated by the identical experimental procedures. Figure 1c also shows the comparison between edges and flat planes of ZnO seed layers on the cross-sectional and tilted (45 °) SEM images. Clearly, the inclined ZnO nanowires were preferentially formed only at edges of seed layers. Since it is well known that the surface energies at edges are in general higher than those at flat planes due the increased number of surface dangling bonds, a nucleation during ZnO hydrothermal growths preferentially occurs at edges.[34-36] More importantly, the growth direction of ZnO nanowires at edges cannot be intentionally defined and depends on the stochastic event where a nucleation around edges occurs.[37,38] Thus, these results highlight that sharp edge structures of seed layers, which have been regarded as well-defined structures in conventional lithography, are highly detrimental to define *in-situ* fabrication of bridging nanosensors and their structural and electrical properties.

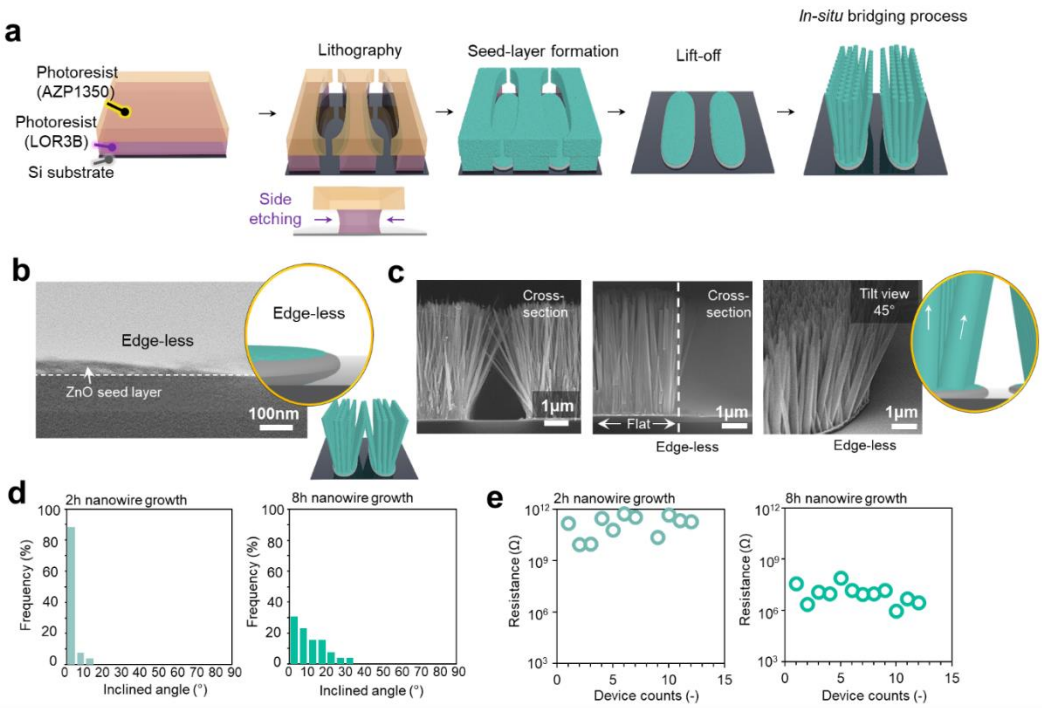

Figure 2. Bridging nanosensors fabricated from a newly proposed edge-less seed layer, and their structural and electrical properties: (a) Schematic of experimental procedure to fabricate bridging nanosensors using conventional lift-off process, (b) Cross-sectional SEM images of fabricated edge-less seed layer, (c) Cross-sectional and tilted top-view SEM images of fabricated bridging ZnO nanowires at edge and flat area of seed layer, (d) Angle distribution of ZnO nanowires between two opposing seed layers, angles were calculated by inclined nanowire angle to vertical direction (2 hours and 8 hours nanowire growth), (e) Statistics electrical resistance of fabricated nanosensors (2 hours and 8 hours nanowire growth).

Next, we aim to control above unintentional statistical variability of structural and electrical properties in *in-situ* fabricated bridging nanosensors. Based on aforementioned edge-based mechanism for variability, we propose an edge-less seed

layer structure to define the growth direction for *in-situ* fabrication of bridging nanosensors. Figure 2a shows the experimental procedure using two-layers resist methods to form an edge-less seed layer structure. The different side etching rate between the two laminated resists creates an umbrella-like structure on the substrate (Figure S2), which results in an edge-less seed layer formation via a surface diffusion to the shadow area during ZnO sputtering process. In addition, the top-view patterns of seed layers were designed to be rounded to avoid geometrical edges (Figure S3-S6). The cross-sectional SEM images of fabricated edge-less seed layers shown in SEM images in Figure 2b revealing the absence of sharp edge structures in the seed layers. Figure 2c shows cross-sectional SEM images of fabricated bridging ZnO nanosensors using above edge-less seed layers. Fabricated ZnO nanowires preferentially grows in the direction perpendicular to the substrate. Figure 2d shows the inclined angle distribution data, and Figure 2e shows the statistical distribution of electrical properties measured between two electrodes. Table 1 shows the comparison between the two bridging sensors on the standard deviation of measured electrical resistances. As clearly seen, there is a significant effect of edge-less seed layers on observed structural and electrical properties of bridging ZnO nanosensors. First, when compared with structures using sharp edge seed layers (Figure 1b), the ratio of inclined ZnO nanowires was substantially suppressed by using edge-less seed layers. As designed, the absence of edge structures in seed layers play an essential role on observed improvements of directional controllability for *in-situ* fabrication of bridging nanosensors. Second, such structural improvement substantially suppresses the unintentional statistical variability of electrical properties shown in Figure 2e. Cross-sectional and tilted (45 °) SEM images for nanowires on edge-less ZnO seed layers were shown in Figure 2c, revealing that the edge-less seed layer enables to define the growth angle of hydrothermal ZnO

nanowires without unintentional inclined nanostructures. The same trend was confirmed for all bridging nanosensors fabricated from edge-less seed layers (Figure S7). Thus, these results highlight that newly proposed methodology using edge-less seed layers allows us to perform well-defined *in-situ* fabrication of bridging nanosensors without uncontrollable structural and electrical properties.

Figure 3 shows the effect of edge-topological regulation on NO_2 sensing response values. In order to examine the scalability and spatial homogeneity of sensor characteristics, we systematically varied the width of bridging nanosensors from 10 to 1000μm, as shown in SEM images of Figure 3a. Spatial selectivity of crystal growth on seed layers enables to modify the device geometry. Figure 3b shows the comparison between the two types of bridging nanosensors on the sensing responses when varying the sensor channel width. The device geometries with the gap width of 2μm and the nanowire length of ~6μm (8 hours growth) were preliminary optimized for NO_2 sensing performance at their operation temperature of 200°C (Figure S8-S10). As clearly seen in the figure, the statistical variation of sensor responses strongly depends on the edge-topological regulation for bridging nanosensors.

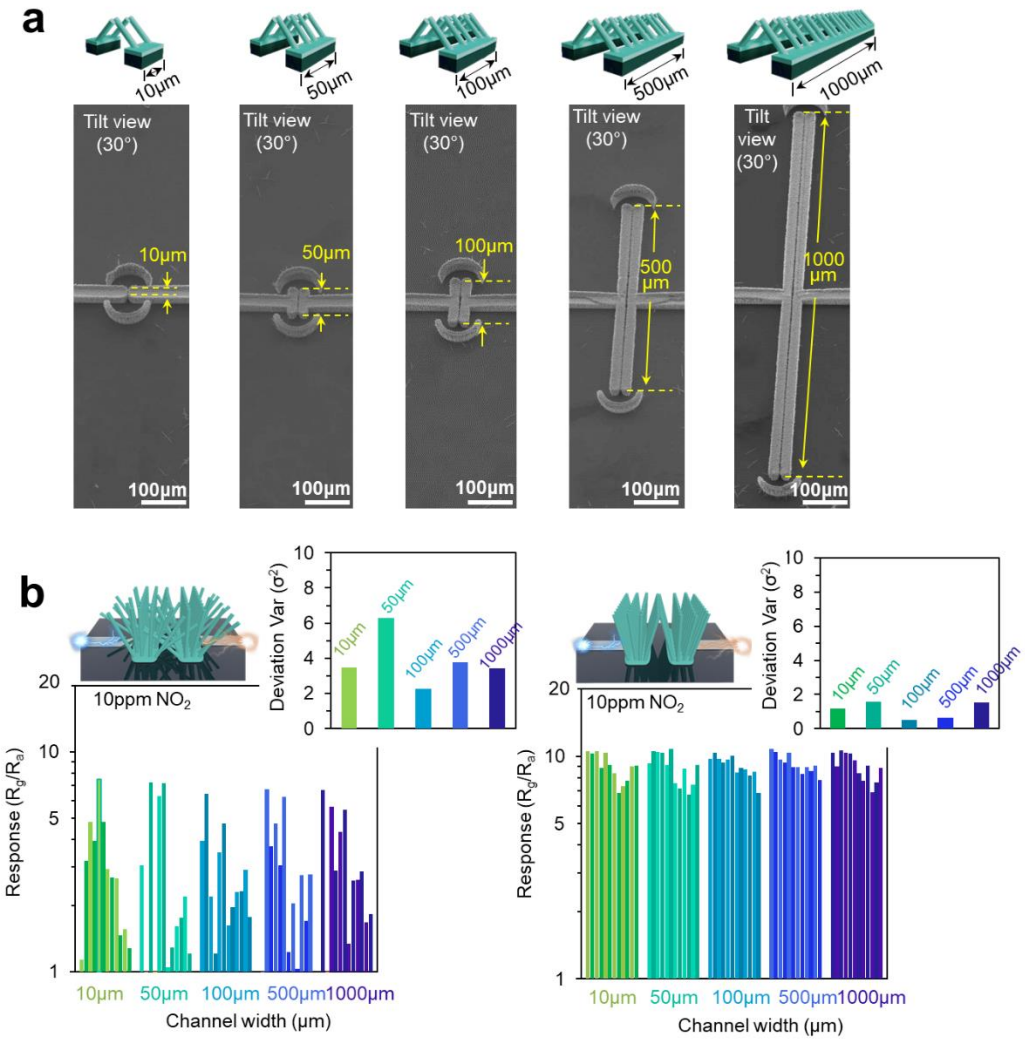

Figure 3. Effect of bridging structural difference on NO_2 sensing data of bridging nanosensors with widths ranged from 10-1000μm: (a) Schematic and SEM images of fabricated bridging nanosensors fabricated from the edge-less seed layer when varying the width ranged from 10 to 1000μm, (b) Comparison between two bridging nanosensors fabricated from the sharp edge seed layer or the edge-less seed layer on NO_2 sensing response data hen varying the width ranged from 10 to 1000μm, the insert figure shows the deviation value (σ^2) of bridging nanosensors.

The standard deviation of sensor responses for bridging nanosensors fabricated from sharp edge seed layers is obviously much larger than those of bridging nanosensors fabricated from edge-less seed layers, and these standard deviation values were shown in the insert figures of Figure 3b. The structural difference between the two in Figure 1 and 2 clearly corresponds to the observed sensor responses and their statistical variation. In addition, for bridging nanosensors fabricated from edge-less seed layers, the sensor response value was almost constant when varying the width of sensors in the range of 10-1000μm. This width insensitivity of sensor responses can be rigorously understood in terms of the definition of sensor response-R_g/R_a and their width, *w*, dependence. If the resistance changes with respect to sensor responses uniformly occur, both R_g and R_a are inversely proportional to *w*, explaining the width insensitivity of sensor responses as constant R_g/R_a. In addition to this width independent property of responses, the constant value of response regardless of sensor length *L* was also confirmed (Figure S11). These results highlight that the bridging nanosensors fabricated from edge-less seed layers are spatially uniform and highly scalable in the range of widths from 10-1000μm.

Figure 4 shows the application of the proposed methodology to the most conventional interdigitated array electrodes as gas sensors. Figure 4a shows the schematic image of fabricated devices with interdigitated array electrodes. (Figure S12) Figure 4b shows the SEM images of fabricated bridging nanosensors.

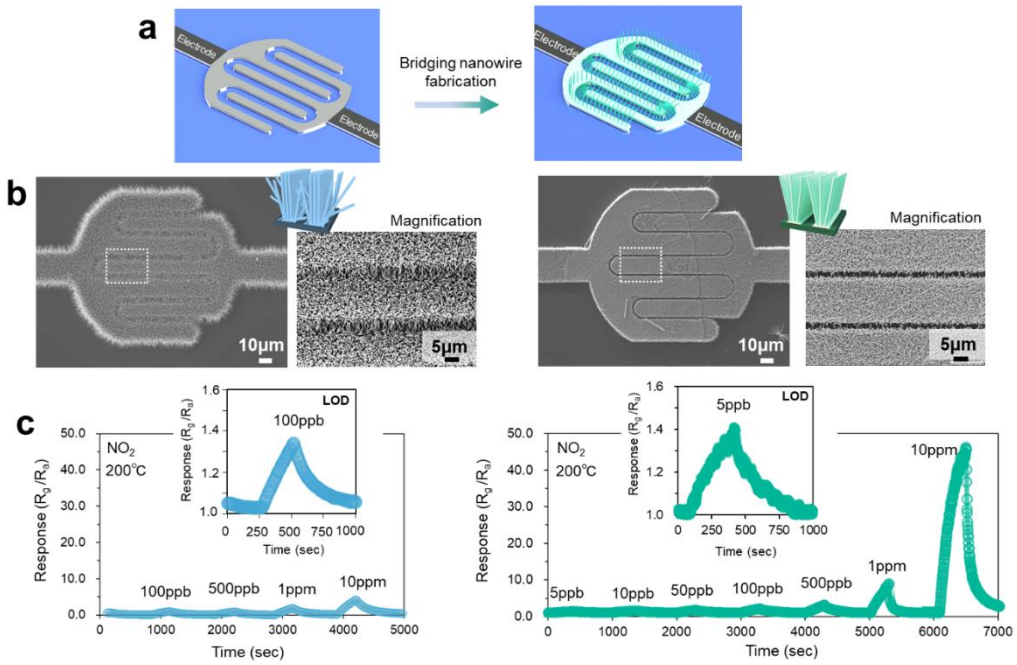

Figure 4. Applicability of bridging nanosensors to interdigitated array electrodes, and comparison between two fabrication processes on NO_2 sensing data: (a) Schematic image of fabricated bridging nanosensors with interdigitated array electrodes, (b) Comparison between two bridging nanosensors fabricated from the sharp edge seed layer or the edge-less seed layer on SEM images of fabricated bridging nanosensors, (c) Comparison between two bridging nanosensors fabricated from the sharp edge seed layer or the edge-less seed layer on NO_2 gas sensing data when varying the concentration.

The gap width of and the nanowire length are 2μm and ~6μm (8 hours growth), respectively, which have been preliminary optimized. The same trend of structural difference can be seen in the images. Figure 4c shows the comparison between the two types of bridging nanosensors on the NO_2 sensor responses when varying the concentration from 5ppb to 10ppm. The limitation of detection (LOD) for bridging

nanosensors fabricated from edge-less seed layers is 5ppb, which is 20 times lower than 100ppb for bridging nanosensors fabricated from sharp edge seed layers. This LOD enhancement is a consequence of precisely regulating nano-bridging events to avoid detrimental merging of two nanostructures. Thus, bridging nanosensors fabricated from edge-less seed layers can be applicable to interdigitated array electrodes with the lower LOD. In addition, we apply this methodology to multi-sensor channel structures, as illustrated in Figure 5a. Figure 5b shows the SEM images of fabricated bridging nanosensors fabricated from edge-less seed layers with well-defined microstructures. Figure 5c shows the spatial variation of NO_2 (10ppm) sensor responses for fabricated multi-sensor channel structures. Clearly, the sensor response is almost identical independent of sensor spatial positions, highlighting the spatial designability and uniformity of the present method. Finally, we demonstrate the *in-situ* controllability of the present method by systematically varying the sensor gap size and the crystal growth time during bridging process. Figure 6a shows the cross-sectional SEM images wen varying the gap size and the bridging process time when employing edge-less seed layers. There is an optimal growth time to complete bridging process, which strongly depends on the device geometry-gap size. The wider gap sizes the longer growth time to accomplish bridging between two opposing electrodes. The results and details of fabricated devices are shown in Figure S13-S14. Figure 6b shows the NO_2 (10ppm) sensor responses when varying sensor gap size and the crystal growth time during bridging process. As clearly seen in the figure, there is a maximum of sensor responses as a function of nanowire length, which corresponds to the situation when the bridging process is optimized. Thus, the present method allows us to optimize and design the sensor characteristics of bridging nanosensors *in-situ*.

5.5 Conclusion

In summary, we report the significant effect of edge-topological regulation on such *in-situ* fabrication of hydrothermally grown ZnO bridging nanostructures. The growth angle distribution of fabricated bridging nanostructures between two opposing seed layers was rather wide and could not be well controlled, when employing seed layers with a sharp edge, which is a well-defined structure in conventional lithography. We found that such conventionally well-defined shape edge structure is not appropriate and detrimental for *in-situ* fabrication of well-defined bridging nanostructures due to the inherent uncontrollability of growth directions at edges. We propose an edge-less seed layer structure using two-layers resist methods to define the growth direction for *in-situ* fabrication of bridging nanostructures. Bridging nanostructures fabricated using such edge-less seed layer structures exhibited much superior directional controllability for *in-situ* fabrication. Furthermore, such well-defined bridging nanostructures not only substantially suppress the unintentional variations of electrical resistances between electrodes, but also significantly enhance the sensing responses for NO_2 with the smaller standard deviation and the lower limitation of detection when compared with those using conventional shape edge seed layers.

5.6 References

(1) Cai, J.; Ruffieux, P.; Jaafar, R.; Bieri, M.; Braun, T.; Blankenburg, S.; Muoth, M.; Seitsonen, A. P. Saleh, M.; Feng, X. L.; Mullen, K.; Fasel, R. Atomically Precise Bottom-up Fabrication of Graphene Nanoribbons. *Nature*. **2010**, *466*, 470-473. DOI: 10.1038/nature09211

(2) Zhang, W. X.; Yang, S. H. In Situ Fabrication of Inorganic Nanowire Arrays Grown from and Aligned on Metal Substrates. *Accounts of Chemical Research.* **2009**, *42, 10*, 1617-1627. DOI: 10.1021/ar900105c

(3) Jensen, J.; Frederik C. K. From the Bottom up–flexible Solid State Electrochromic Devices. *Advanced Materials*. **2014**, *26, 42*, 7231-7234. DOI: 10.1002/adma.201402771

(4) Liu, S. T.; Maoz, R.; Sagiv, J. Planned Nanostructures of Colloidal Gold via Self-assembly on Hierarchically Assembled Organic Bilayer Template Patterns with in-situ Generated Terminal Amino Functionality. *Nano Letters*. **2004**, *4, 5*, 845-851. DOI: 10.1021/nl049755k

(5) Philipp, L.; Zielke, L.; Bouvron, S.;Moroni, R.; Voloshina, E.; Hammerschmidt, L.; Dedkov, Y. S.; Fonin, M. In Situ Fabrication of Quasi-Free-Standing Epitaxial Graphene Nanoflakes on Gold, *ACS Nano*, **2014**, *8*, *4*, 3735-3742. DOI: 10.1021/nn500396c

(6) Tang, S. Y.; Yang C. C.; Su, T. Y.; Yang, T. Z.; Wu, S. C.; Hsu, Y.C.; Chen, Y. Z.; Lin, T. Z.; Shen, J. L.; Lin, H. N.; Chiu, P. W.; Kuo, H. C.; Chueh, Y. L. Design of Core–Shell Quantum Dots–3D WS_2 Nanowall Hybrid Nanostructures with High-Performance Bifunctional Sensing Applications. *ACS Nano*, **2020**, *14, 10*, 12668-12678. DOI: 10.1021/acsnano.0c01264

(7) Jiang, H. Chemical Preparation of Graphene-based Nanomaterials and Their Applications in Chemical and Biological Sensors. *Small*, **2011**, *7*, *17*, 2413-2427. DOI: 10.1002/smll.201002352

(8) Li, M. W.; Bhiladvala, R. B.; Morrow, T. J.; Sioss, J. A.; Lew, K. K.; Redwing, J. M.; Keating, C. D.; Mayer, T. S. Bottom-up Assembly of Large-area Nanowire Resonator Arrays. *Nature Nanotechnology*, **2008**, *3, 2,* 88-92. DOI: 10.1038/nnano.2008.26

(9) Hawkeye, M. M.; Brett, M. J. Optimized Colorimetric Photonic-crystal Humidity SensorFabricated Using Glancing Angle Deposition. *Advanced Functional Materials*, **2011**, 21, 19, 3652-3658. DOI: 10.1002/adfm.201100893

(10) Huang, J. F.; Zhu, Y. H.; Yang, X. L.; Chen, W.; Zhou, Y.; Li, C. Z. Flexible 3D Porous CuO Nanowire Arrays for Enzymeless Glucose Sensing: in situ Engineered Versus ex situ Piled. Nanoscale, 2015, 7, 2, 559-569. DOI: 10.1039/C4NR05620E

(11) Xue, M.; Zhang, Y.; Yang, Y. Processing Matters: In situ Fabrication of Conducting Polymer Microsensors Enables Ultralow-limit Gas Detection. *Advanced Materials*, **2008**, *20, 11*, 2145-2150. DOI: 10.1002/adma.200702864

(12) Attia, R.; Pregibon, D. C.; Doyle, P. S.; Viovy, J. L.; Bartolo, D. Soft Microflow Sensors. *Lab on a Chip*, **2009**, *9*, *9*, 1213-1218. DOI: 10.1039/B813860E

(13) Gao, W.; Emaminejad, S.; Nyein, H. Y. Y.; Challa, S.; Chen, K.; Peck, A.; Fahad, H. M.; Ota, H.; Shiraki, H.; Kiriya, D.; Lien, D. H.; Brooks, G. A.; Davis, R. W.; Javey, A. Fully Integrated Wearable Sensor Arrays for Multiplexed in situ Perspiration Analysis. *Nature*, **2016**, *529, 7587*, 509-514. DOI: 10.1038/nature16521

(14) Mijatovic, D.; Eijkel, J. C. T.; Van den Berg, A. Technologies for Nanofluidic Systems: top-down vs. bottom-up—a review. *Lab on a Chip*. **2005**, *5*, *5*, 492-500. DOI: 10.1039/B416951D

(15) Yang, P. D.; Yan R. X.; Fardy, M. Semiconductor Nanowire: What's next? *Nano Letters*, **2010**, *10*, *5*, 1529-1536. DOI: 10.1021/nl100665r

(16) Mehta, R. J.; Zhang, Y. L.; Karthik, C.; Singh, B. Siegel. R. W.; Borca-Tasciuc, T.; Ramanath, G. A New Class of Doped Nanobulk High-Figure-of-Merit Thermoelectrics by Scalable Bottom-up Assembly. *Nature Materials*, **2012**, *11*, *3*, 233-240. DOI: 10.1038/nmat3213

(17) Zhao, D.; Huang, H.; Chen, S.; Li, Z.; Li, S.; Wang, M. Y.; Z, H. C.; Chen, X. M. In situ Growth of Leakage-Free Direct-Bridging GaN Nanowires: Application to Gas Sensors for Long-Term Stability, Low Power Consumption, and Sub-ppb Detection Limit. *Nano Letters*, **2019**, *19*, *6*, 3448-3456. DOI: 10.1021/acs.nanolett.8b04846

(18) Steinhauer, S.; Chapelle, A.; Menini, P.; Sowwan, M. Local CuO Nanowire Growth on Microhotplates: In situ Electrical Measurements and Gas Sensing Application. *ACS Sensors*, **2016**, *1*, *5*, 503-507. DOI: 10.1021/acssensors.6b00042

(19) Park, W. J.; Choi, K. J.; Kim, M. H.; Koo, B. H.; Lee, J. L.; Baik, J. M. Self-Assembled and Highly Selective Sensors Based on Air-Bridge-Structured Nanowire Junction Arrays. *ACS Applied Materials & Interfaces*, **2013**, *5*, *15*, 6802-6807. DOI: 10.1021/am401635e

(20) Han, H.; Kim, J.; Shin, H. S.; Song. J. Y.; Lee, W. Air-Bridged Ohmic Contact on Vertically Aligned Si Nanowire Arrays: Application to Molecule Sensors. *Advanced Materials*, **2012**, *24*, *17*, 2284-2288. DOI: 10.1002/adma.201200347

(21) Qi, P.; Vermesh, O.; Grecu, M.; Javey, A.; Wang, Q.; Dai, H.; Peng, S.; Cho, K. J. Toward Large Arrays of Multiplex Functionalized Carbon Nanotube Sensors for Highly Sensitive and Selective Molecular Detection. *Nano letters*, **2003**, *3*, *3*, 347-51. DOI: 10.1021/nl034010k

(22) Kamins, T. I.; Sharma, S.; Yasseri, A. A.; Li, Z.; Straznicky, J. Metal-catalysed, Bridging Nanowires as Vapour Sensors and Concept for their Use in a Sensor System. *Nanotechnology*, **2006**, *17*, *11*, S291. DOI:10.1088/0957-4484/17/11/S11

(23) Ahn, M. W.; Park, K. S.; Heo, J. H.; Park, J. G.; Kim, D. W.; Choi, K. J.; Lee, J. H.; Hong, S. H. Gas Sensing Properties of Defect-controlled ZnO-nanowire Gas Sensor. *Applied Physics Letters*, **2008**, *93*, *26*, 263103. DOI: 10.1063/1.3046726

(24) Woo, H. S.; Kwak, C. H.; Kim, I. D.; Lee, J. H. Selective, Sensitive, and Reversible Detection of H_2S Using Mo-doped ZnO Nanowire Network Sensors. *Journal of Materials Chemistry A*, **2014**, *2*, *18*, 6412-6418. DOI: 10.1039/C4TA00387J

(25) Hoa, N.D.; Le, D.; Tam, P.D.; Le, A.T.; Van Hieu, N. On-chip Fabrication of SnO_2-nanowire Gas Sensor: The Effect of Growth Time on Sensor Performance. *Sensors and Actuators B: Chemical*, **2010**, *146*, *1*, 361-367. DOI: 10.1016/j.snb.2010.02.054

(26) Steinhauer, S.; Chapelle, A.; Menini, P.; Sowwan, M. Local CuO Nanowire Growth on Microhotplates: In Situ Electrical Measurements and Gas Sensing Application. *ACS Sensors*, **2016**, *1*, *5*, 503-507. DOI: 10.1021/acssensors.6b00042

(27) Zhao, D.; Huang, H.; Chen, S.; Li, Z.; Li, S.; Wang, M.; Zhu, H.; Chen, X. In Situ Growth of Leakage-free Direct-bridging GaN Nanowires: Application to

Gas Sensors for Long-term Stability, Low Power Consumption, and Sub-ppb Detection Limit. *Nano letters*, **2019**, *19*, *6*, 3448-3456. DOI: 10.1021/acs.nanolett.8b04846

(28) Offermans, P.; Crego-Calama, M.; Brongersma, S. H. Gas Detection with Vertical InAs Nanowire Arrays. *Nano letters*, **2010**, *10*, *7*, 2412-2415. DOI: 10.1021/nl1005405

(29) Liu, J.; Nagashima, K.; Yamashita, H.; Mizukami, W.; Uzuhashi, J.; Hosomi, T.; Kanai, M.; Zhao, X.; Miura, Y.; Zhang, G.; Takahashi, T.; Suzuki, M.; Sakai, D.; Samransuksamer, B.; He, Y.; Ohkubo, T.; Yasui, T.; Aoki, Y.; Ho, J. C.; Baba, Y.; Yanagida, T. Face-selective Tungstate Ions Drive Zinc Oxide Nanowire Growth Direction and Dopant Incorporation. *Communications Materials*, **2020**, *1*, *1*, 1-10. DOI: 10.1038/s43246-020-00063-5

(30) Wang, C.; Hosomi, T.; Nagashima, K.; Takahashi, T.; Zhang, G.; Kanai, M.; Zeng, H.; Mizukami, W.; Shioya, N.; Shimoaka, T.; Tamaoka, T.; Yoshida, H.; Takeda, S.; Yasui, T.; Baba, Y.; Aoki, Y.; Terao, J.; Hasegawa, T.; Yanagida, T. Rational Method of Monitoring Molecular Transformations on Metal-oxide Nanowire Surfaces. *Nano Letters*, **2019**, *19*, *4*, 2443-2449. DOI: 10.1021/acs.nanolett.8b05180

(31) Joo, J.; Chow, B. Y.; Prakash, M.; Boyden, E. S.; Jacobson, M. Face-selective Electrostatic Control of Hydrothermal Zinc Oxide Nanowire Synthesis. *Nature Materials*, **2011**, 10, 8, 596-601. DOI: Nature Materials, 2011, 10, 8, 596-601.

(32) He, Y.; Yanagida, T.; Nagashima, K.; Zhuge, F.; Meng, G.; Xu, B.; Klamchuen, A.; Rahong, S.; Kanai, M.; Li, X.; Suzuki, M.; Kai, S.; Kawai, T. Crystal-plane Dependence of Critical Concentration for Nucleation on Hydrothermal ZnO

Nanowires. *The Journal of Physical Chemistry C*, **2013**, *117*, *2*, 1197-1203. DOI: 10.1021/jp3113232

(33) Chen, L. Y.; Yin, Y. T.; Chen, C. H.; Chiou, J. Influence of Polyethyleneimine and Ammonium on the Growth of ZnO Nanowires by Hydrothermal Method. *The Journal of Physical Chemistry C*, **2011**, *115*, *43*, 20913-20919. DOI:10.1021/jp2056199

(34) Greene, L. E.; Law, M.; Tan, D. H.; Montano, M. Goldberger, J. Somorjai, G.; Yang, P. General Route to Vertical ZnO Nanowire Arrays Using Textured ZnO Seeds. *Nano Letters*, **2005**, 5, 7, 1231-1236. DOI: 10.1021/nl050788p

(35) Guillemin, S.; Consonni, V.; Appert, E. Puyoo, E. Rapenne, L.; Roussel, H. Critical Nucleation Effects on the Structural Relationship Between ZnO Seed Layer and Nanowires. *The Journal of Physical Chemistry C*, **2012**, *116*, *47*, 25106-25111. DOI: 10.1021/jp308643w

(36) Lao, J. Y.; Huang, J. Y.; Wang, D. Z.; Ren, Z.F. ZnO Nanobridges and Nanonails. *Nano Letters*, **2003**, *3*, *2*, 235-238. DOI: 10.1021/nl025884u

(37) Zhao, C. X.; Li, Y. F.; Zhou, J. Li, L.; Deng, S. Z.; Xu, N. S.; Chen, J. Large-scale Synthesis of Bicrystalline ZnO Nanowire Arrays by Thermal Oxidation of Zinc Film: Growth Mechanism and High-performance Field Emission. *Crystal Growth & Design*, **2013**, *13*, *7*, 2897-2905. DOI: 10.1021/cg400318f

(38) Yang, P.; Yan, H.; Mao, S.; Russo, R.; Johnson, J.; Saykally, R.; Morris, N.; Pham, J.; He. R.; Choi, H. J. Controlled Growth of ZnO Nanowires and Their Optical Properties. *Advanced Functional Materials*, **2002**, *12*, *5*, 323-331. DOI: 10.1002/1616-3028(20020517)

5.7 Supporting Information

Figure Captions

Figure S1. Bridging nanosensors fabricated from sharp edge seed layers and their structural and electrical properties.

Figure S2. Cross-sectional SEM images of fabricated two-layer resists with their different side-etching rates.

Figure S3. Effect of top-view topology for two-layer photoresist lithography method.

Figure S4. Effect of top-view topology on bridging nanosensors.

Figure S5. Shadow angle dependence of umbrella-like photoresist on fabricated bridging nanosensors.

Figure S6. SEM images of seed layer edge structures of two-types with round angle patters.

Figure S7. Bridging nanosensors fabricated from edge-less seed layers and their structural and electrical properties.

Figure S8. Bridging process effect on electrical resistances when varying the gap size and growth time.

Figure S9. Electrical properties of bridging nanosensors fabricated from sharp edge and edge-less seed layers.

Figure S10. Temperature dependent NO_2 sensing property of bridging nanosensors fabricated from edge-less seed layer, and their molecular selectivity.

Figure S11. Effect of sensor length on bridging nanosensors.

Figure S12. Schematic image of interdigitated bridging nanosensors.

Figure S13. Top view SEM images of interdigitated bridging nanosensors when varying the gap size and the nanowire length.

Figure S14. Cross-sectional SEM images of interdigitated bridging nanosensors when varying the gap size and the nanowire length.

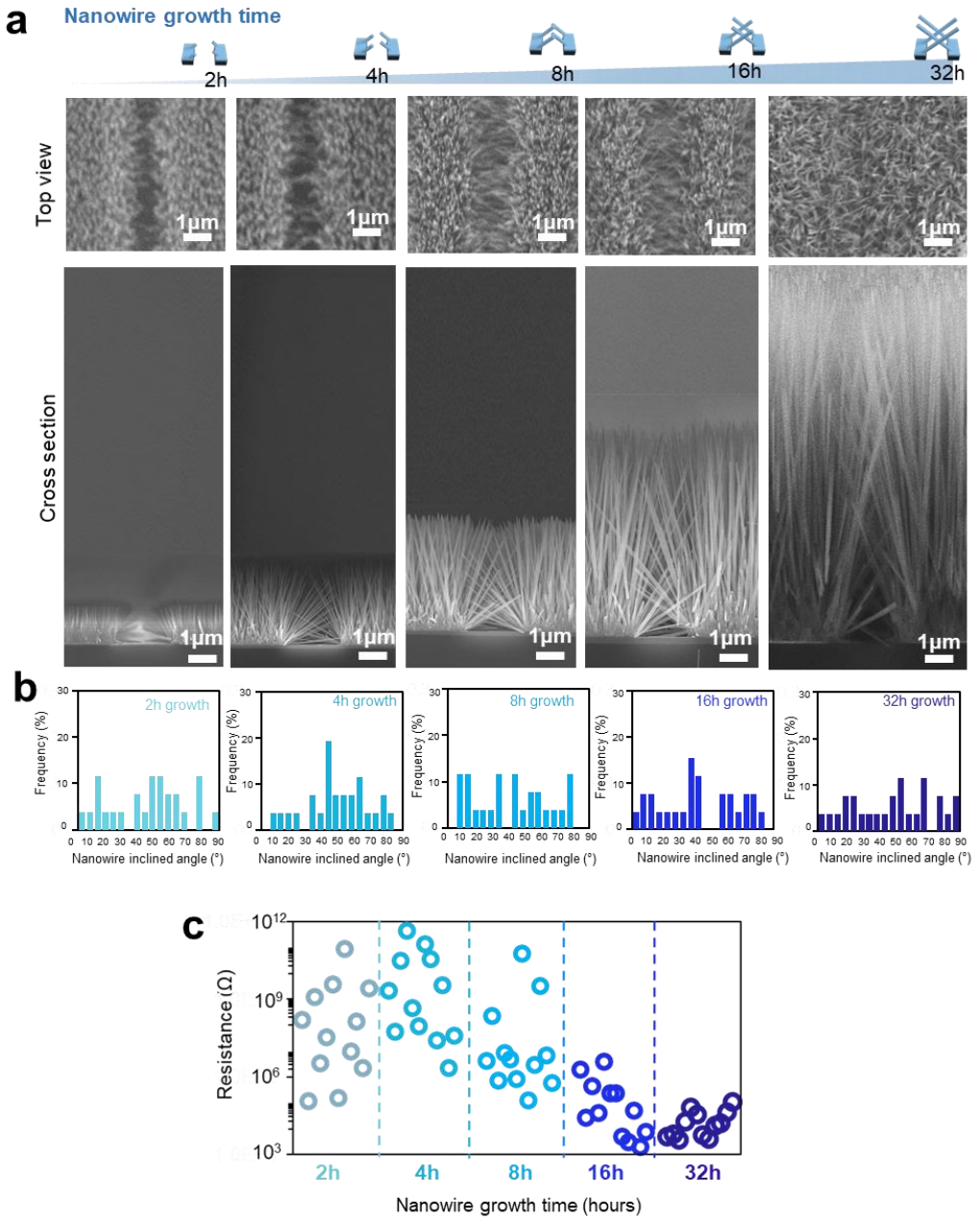

Figure S1. Bridging nanosensors fabricated from sharp edge seed layers and their structural and electrical properties. (a) SEM images (both top view and cross-sectional view) of bridging nanosensors when varying the growth time ranged from 2 to 32 hours, (b) Angle distributions of ZnO nanowires between two opposing seed layers, the estimated inclined angle was defined as shown in the inset schematic of (a), (c)

Statistical electrical resistance data of bridging nanosensors when varying the growth time ranged from 2 to 32 hours.

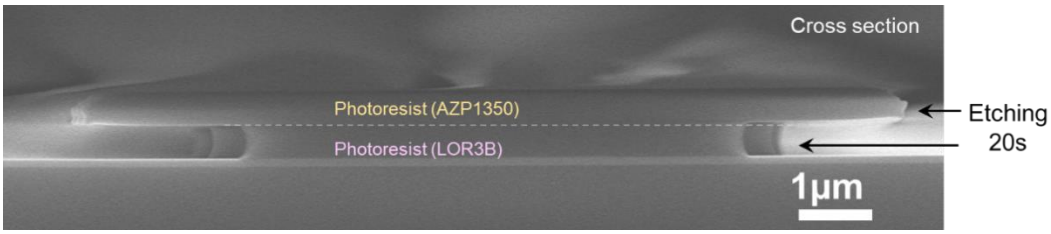

Figure S2. Cross-sectional SEM images of fabricated two-layer resists with their different side-etching rates**.** The top photoresist layer is AZP1350 with almost no side-etching, while the bottom photoresist layer is LOR3B with the significant side-etching rate ~100nm/s, resulting in the umbrella-like photoresist structures.

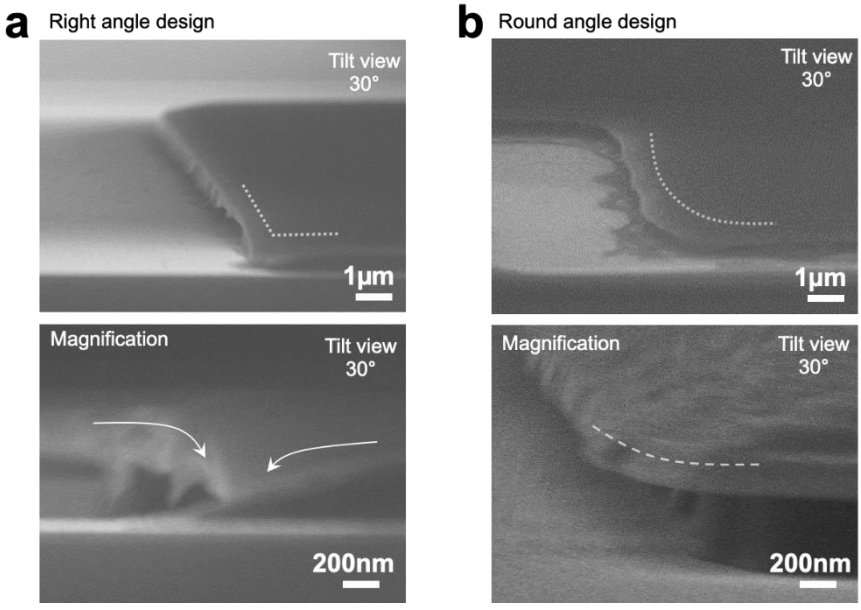

Figure S3. Effect of top-view topology for two-layer photoresist lithography method. (a) SEM images of sputtered seed-layer on two-layer photoresists with right angle design (90°) and its magnified image, (b) SEM images of sputtered seed-layer on two-

layer photoresists with round angle design and its magnified image. The collapse of umbrella-like photoresist construction occurred for "right angle design" but not for "round angle design". The "round angle design" can maintain the umbrella-like structure of two-layer photoresists.

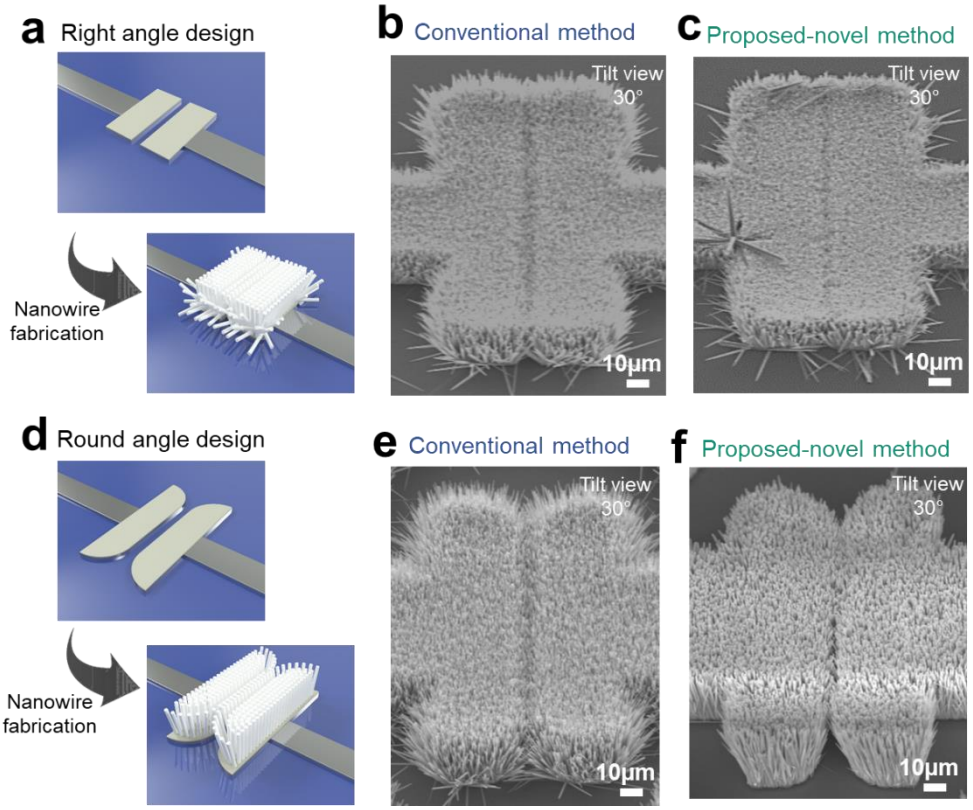

Figure S4. Effect of top-view topology on bridging nanosensors. (a) Schematic image of "right angle design", (b) SEM image of fabricated bridging nanosensors with "right angle design" through conventional one-layer photoresist lithography method, (c) SEM image of fabricated bridging nanosensors with "right angle design" through proposed-novel two-layer photoresist lithography method, (d) Schematic image of "round angle design", (e) SEM image of fabricated bridging nanosensors with "round angle design" through conventional one-layer photoresist lithography method, (f) SEM image of

fabricated bridging nanosensors with “round angle design” through proposed-novel two-layer photoresist lithography method.

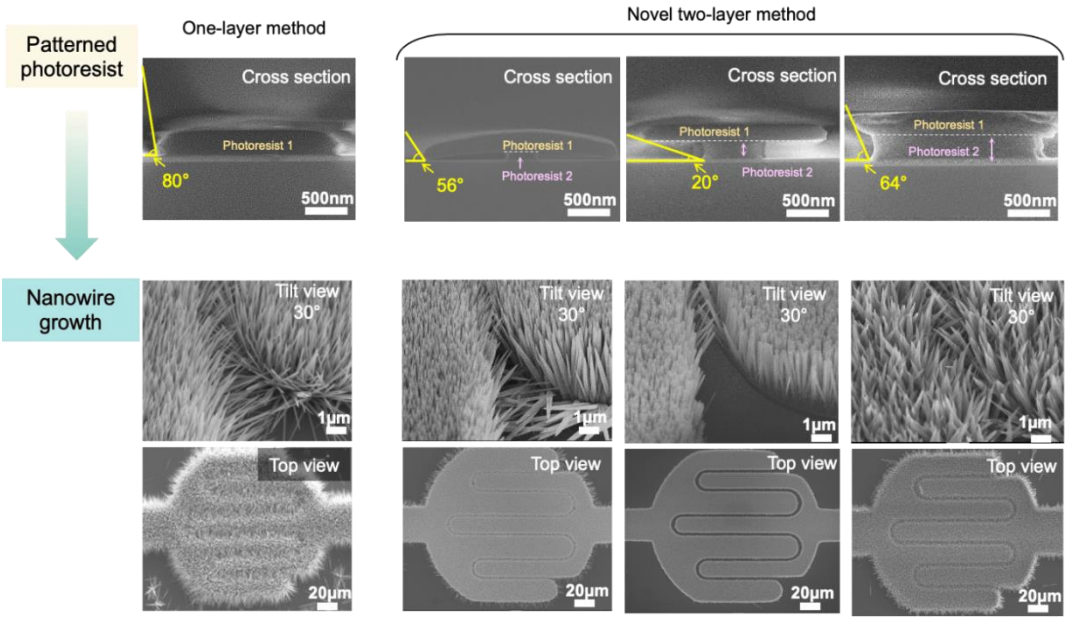

Figure S5. Shadow angle dependence of umbrella-like photoresist on fabricated bridging nanosensors.

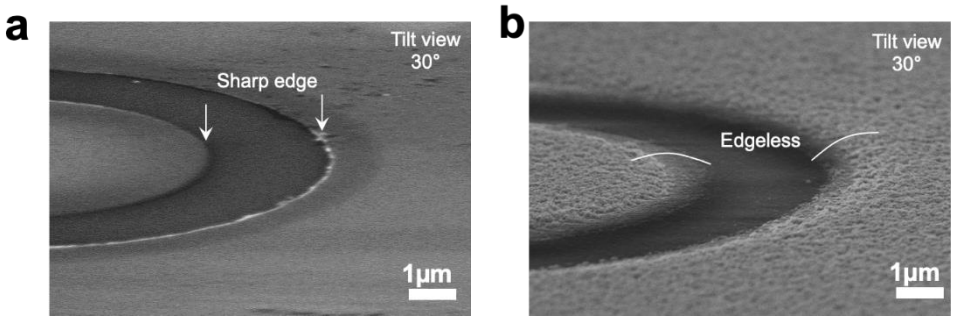

Figure S6. SEM images of seed layer edge structures of two-types with round angle patters. (a) Sharp-edge obtained by conventional one-layer photoresist lithography method, (b) Edge-less morphology obtained by proposed two-layer photoresist lithography method.

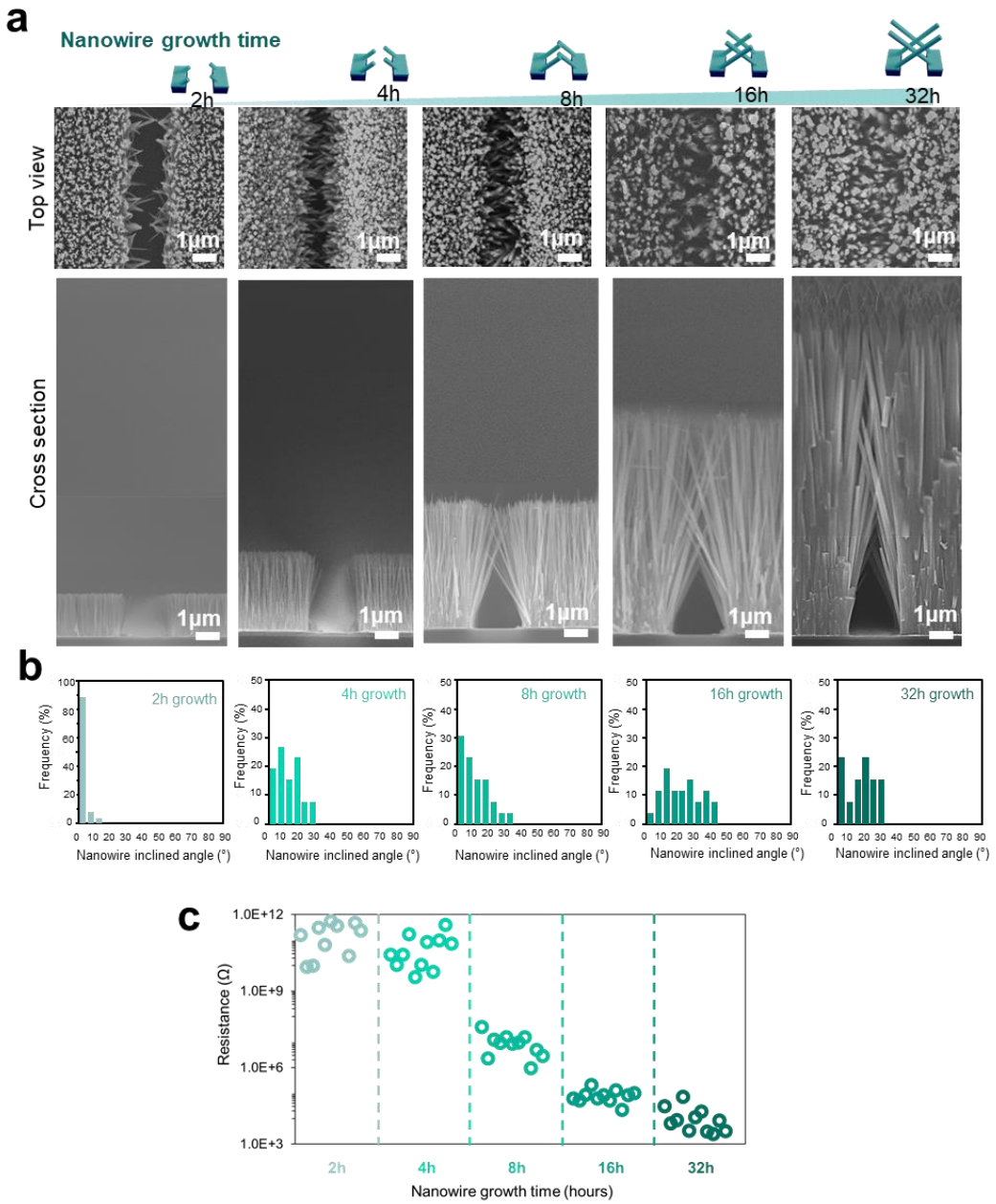

Figure S7. Bridging nanosensors fabricated from edge-less seed layers and their structural and electrical properties. (a) SEM images (both top view and cross-sectional view) of bridging nanosensors when varying the growth time ranged from 2 to 32 hours, (b) Angle distributions of ZnO nanowires between two opposing seed layers, the estimated inclined angle was defined as shown in the inset schematic of (a), (c)

Statistical electrical resistance data of bridging nanosensors when varying the growth time ranged from 2 to 32 hours.

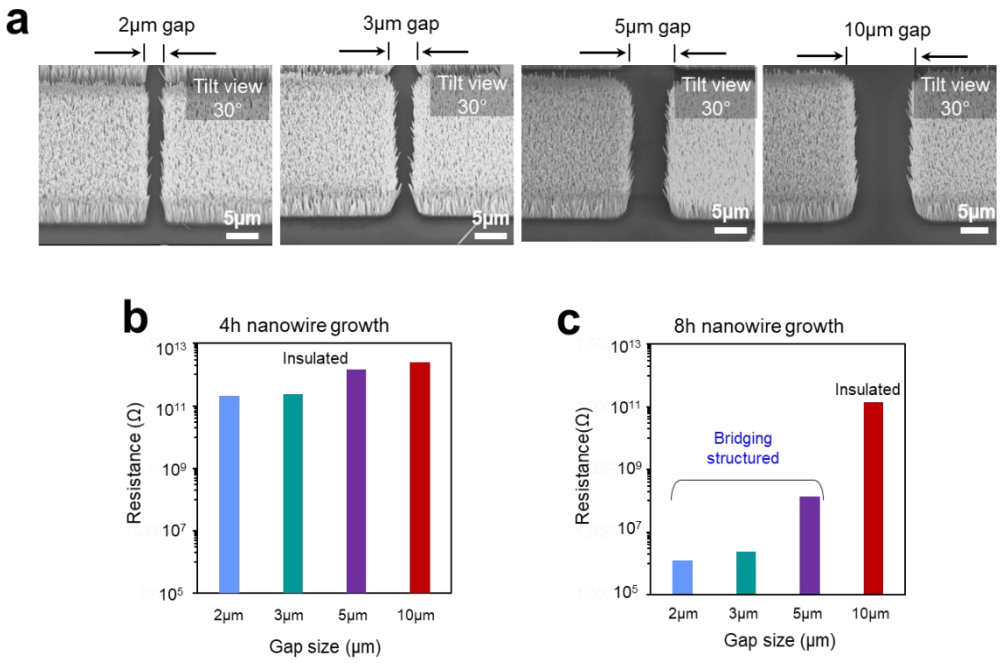

Figure S8. Bridging process effect on electrical resistances when varying the gap size and growth time. (a) Tilted SEM images of bridging nanosensors when varying gap sizes from 2-10μm with the constant growth time 4h, (b) Electrical resistances of bridging nanosensors when varying gap sizes from 2-10μm with the constant growth time 4h, (c) Electrical resistances of bridging nanosensors when varying gap sizes from 2-10μm with the constant growth time 8h.

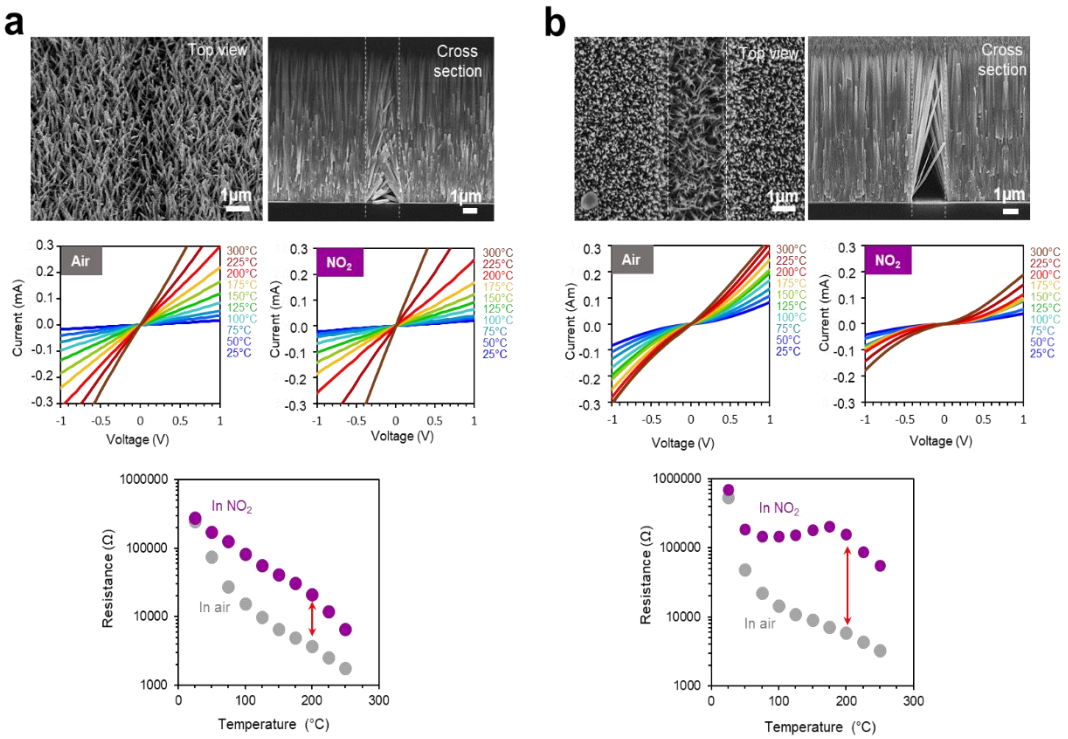

Figure S9. Electrical properties of bridging nanosensors fabricated from sharp edge and edge-less seed layers. (a) SEM images of bridging nanosensors fabricated from sharp edge seed layers and the temperature dependent electrical resistances under both air/NO_2 atmospheres, (b) SEM images of bridging nanosensors fabricated from edge-less seed layers and the temperature dependent electrical resistances under both air/NO_2 atmospheres,

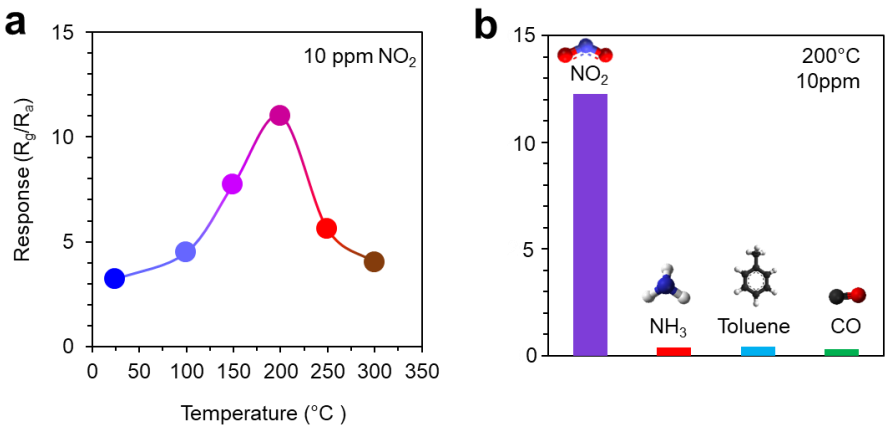

Figure S10. Temperature dependent NO_2 sensing property of bridging nanosensors fabricated from edge-less seed layer, and their molecular selectivity. The gap size and the growth time for bridging process is 2µm and 8hours, respectively. gap size for 8 hours). (a) Operation temperature dependence of NO_2 sensing performance, (b) Selectivity of sensing characters among 10 ppm NO_2, NH_3, Toluene and CO at the operation temperature of 200 °C.

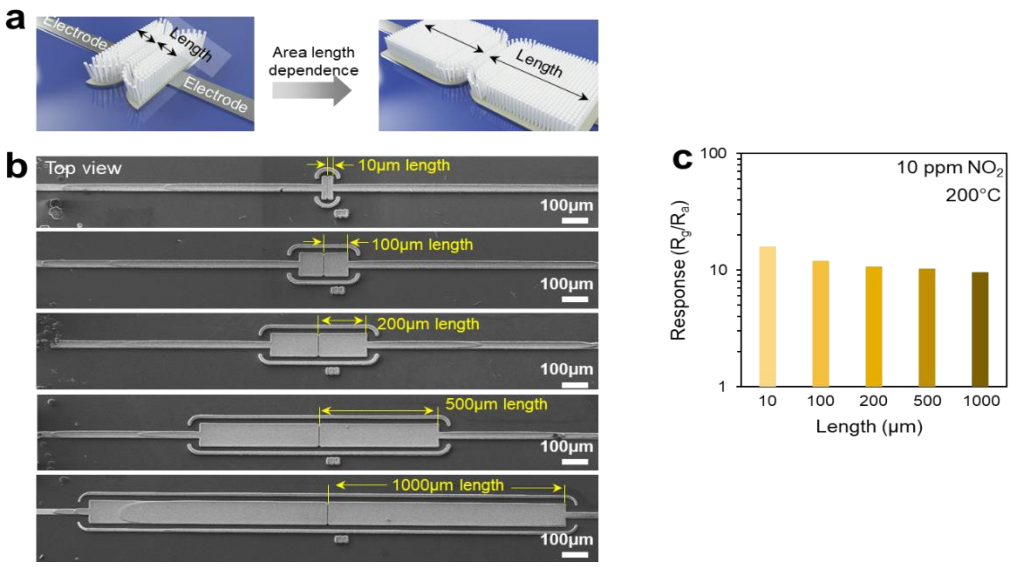

Figure S11. Effect of sensor length on bridging nanosensors. (a) Schematic illumination of bridging nanosensors with various sensor lengths, (b) SEM images of fabricated bridging nanosensors with their length ranged from 10-1000μm, (c) Effect of sensor length on NO_2 sensing response of fabricated bridging nanosensors.

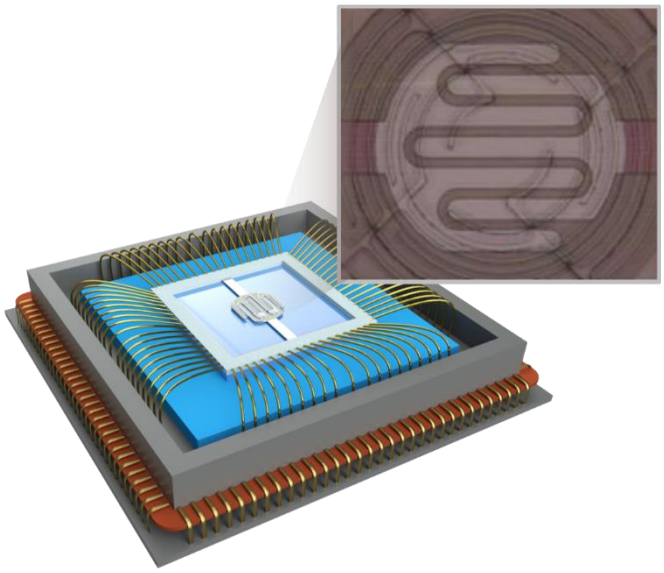

Figure S12. Schematic image of interdigitated bridging nanosensors.

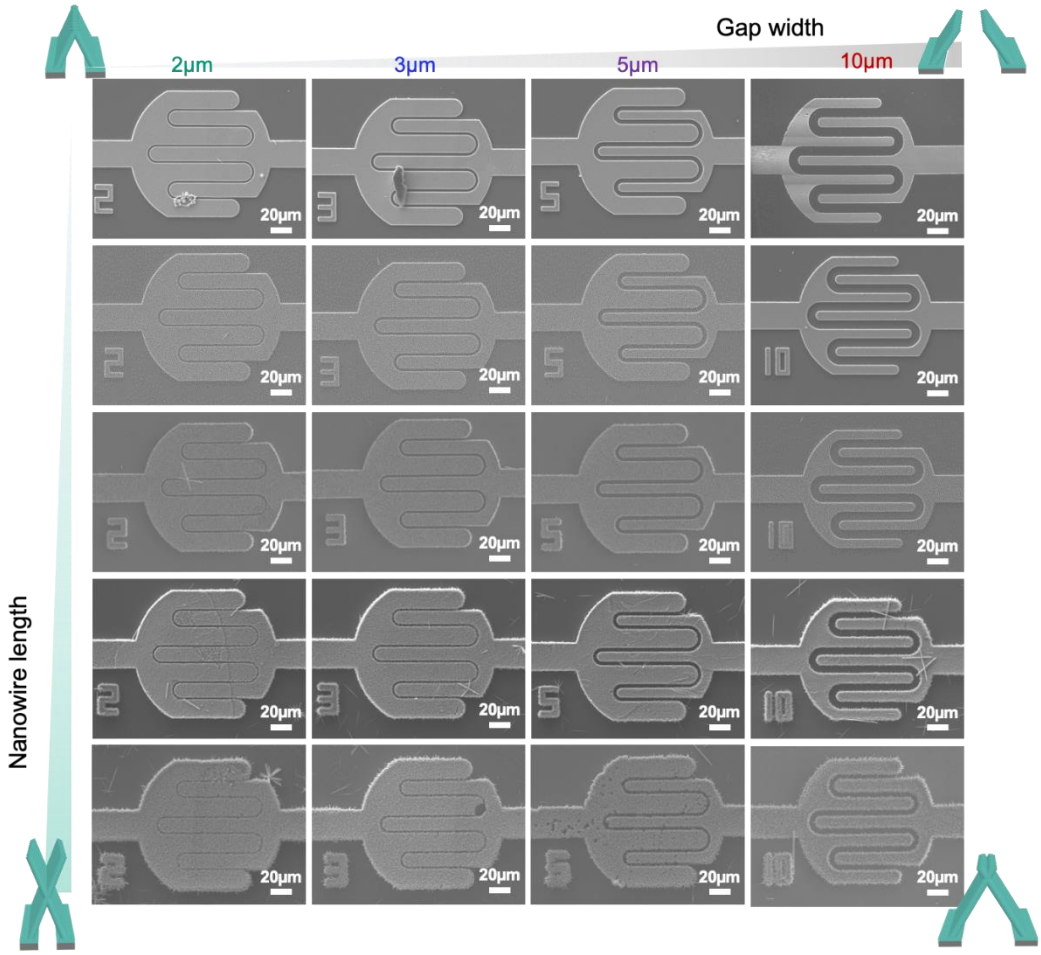

Figure S13. Top view SEM images of interdigitated bridging nanosensors when varying the gap size and the nanowire length.

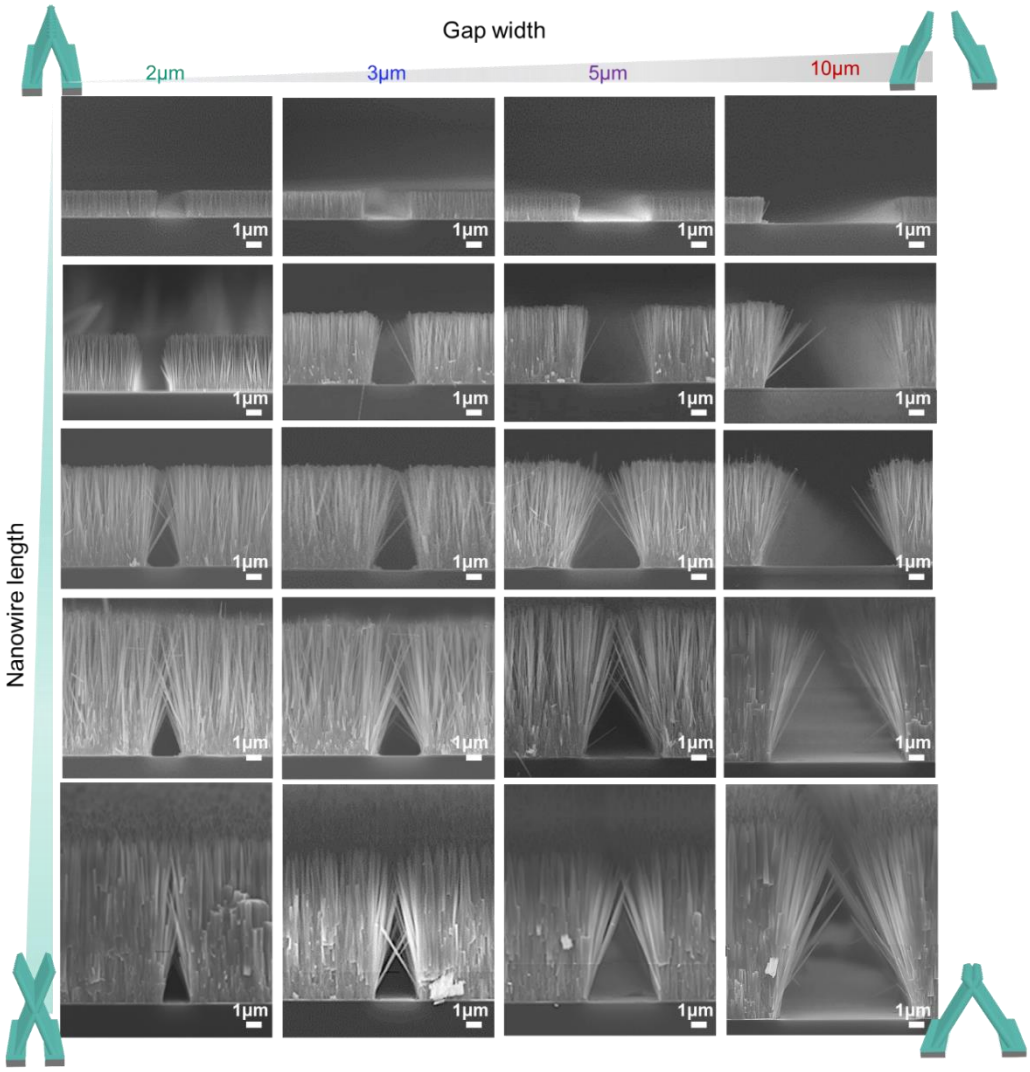

Figure S14. Cross-sectional SEM images of interdigitated bridging nanosensors when varying the gap size and the nanowire length.

CHAPTER VI

CONSTRUCTION OF THERMAL ROBUST KETONE SENSING MOLECULAR SELECTOR INTEGRATED SENSOR

6.1 Abstract

Here we demonstrate a discriminative molecular sensing in mixture using a difference of reactivity in adsorbed molecules on metal oxide nanowire surface. Sol-gel ZrO_2 coated nanowires exhibit distinct selectivity for collecting 2-nonanone (C9 ketone) in mixture containing chemically similar nonanal (C9 aldehyde), which is not available in sputter ZrO_2 coated nanowires. Infrared (IR) spectroscopy and x-ray photoemission spectroscopy indicate that such selectivity in sol-gel ZrO_2 coated nanowires is caused by the difference of oxidation stability in adsorbed species. Aldehyde i.e. nonanal is easily oxidated by activated oxygen on sol-gel ZrO_2 surface while ketone i.e. 2-nonanone with higher resistivity for oxidation remains on the surface. Based on above finding, we successfully demonstrate a discriminative molecular sensing of 2-nonanone in mixture by a nanowire selector-integrated sensor device, with which 2-nonanone is selectively collected by sol-gel ZrO_2 coated nanowire surface, thermally desorbed and electrically detected by sensor. This strategy using a difference of reactivity in adsorbed molecules breaks through the limitation of molecular sensing for electrically discriminating the chemically similar molecules in mixture.

KEYWORDS: *ketone sensing, Oxide nanowire, ZrO_2, 2-nonanone, nonanal, molecular selector*

6.2 Introduction

Molecular sensors have received considerable interest over past decades as they hold great promise for the ever-increasing demand for advancements in monitoring the environment surroundings, health condition of individuals and communication technologies of modern smart objects.[1-4] Although the generalized detection of molecules has employed for sensors, the discrimination of compounds within a given molecule mixture remains a challenging goal due to similar chemical property of contained molecules. Thus, technical breakthrough for discriminating molecule mixture is strongly required, and a molecular selector is a promising way to increase the molecular recognition for sensor.

Basically, organic method has been considered as a promising way to recognize the target molecule in molecule mixture.[5] However, it always requires for thermally robust for molecular selector in a hybrid device for sensor, while organics are widely known as their weakness in thermal robustness. On the other hand, metal oxide has shown their interaction with molecules on the surface. ZrO_2 is an important and versatile transition metal oxide that is extensively utilized in ceramics, chemical sensors, solid oxide fuel cell electrolytes, and semiconductor devices.[6-10] In recent years, ZrO_2 as a catalyst and catalyst support has attracted much attention because of its distinctive amphoteric and redox features. The crystalline phases of ZrO_2 can affect the selective reaction as well as can lead to the selective products.[11, 12] For instance, in CO hydrogenation reaction, tetragonal zirconia[13-15] showed the main products of methane, ethane, and propene, while it was observed the higher selectivity for butane using monoclinic zirconia[16]. In hydrogenation of olefins, tetragonal zirconia gave the maximum activity against 1,3-

butadiene[17,18], whereas monoclinic zirconia showed the maximum activity against cyclohexadiene[19,20].

In this work, ZrO_2 was prepared by a conventional precipitation sol-gel technique. Sol-gel technology has been widely used for the preparation of metal oxides due to its advantages of easy control of purity and homogeneity at low temperatures.[21-25] A selectivity result of 2-nonanone as ketone in the mixture was found on sol-gel processed ZrO_2 surface. Compared with conventional sputtering processed ZrO_2, by characterization method of XPS and EXAFS, a highly oxygen occupied surface was found only on sol-gel processed ZrO_2 surface. With this highly oxidation surface, nonanal as aldehyde was fully oxidized like burn on the sol-gel ZrO_2 surface. By using FT-IR, we can clearly see the peak that represented the oxidation for nonanal compare with 2-nonanone. We extended our study to check the selectivity of ketone in mixture with various chain length (C8 and C11) on sol-gel processed ZrO_2 surface. The molecular selection result showed same the tendency with C9, which verified this highly oxidation surface could be extended to sensing other ketone molecules in mixture. Furthermore, with the sol-gel ZrO_2 surface, we fabricated a hybrid sensor device. The sensing result demonstrated this highly oxidation surface was a promising method for selectivity ketone sensing in sensor device.

6.3 Experimental Section

Sample preparation. ZnO nanowires utilized as template for depositing ZrO_2 layer were synthesized on SiO_2/Si (100) wafer by a seed-assisted hydrothermal method.[21] First, Ti adhesion layer (5 nm) and ZnO seed layer (100 nm) were sequentially deposited on the wafer via radio frequency (RF) sputtering method. Aqueous solution for the nanowire growth was prepared by mixing 50 mM zinc acetate

dehydrate ($Zn(CH_3COO)_2)\cdot 2H_2O$, Sigma-Aldrich ≥98.0 %), 50 mM hexamethylenetetramine ($C_6H_{12}N_4$, Wako 99.0 %) and 20 mM polyethyleneimine (PEI, M_n~1800, Sigma-Aldrich 50 wt% in H_2O) in 200 mL deionized (DI) water.[22-25] The seed-deposited substrate was then immersed into the aqueous solution in manner of up-side-down to avoid the deposition of precipitate in the solution. The hydrothermal process was conducted at 95 ºC for 24 h and ZnO nanowires with ca. 100 nm diameter and ca. 11 μm length were formed. ZrO_2 layer was coated on the ZnO nanowires by two different methods including sol-gel synthesis and sputtering. For sol-gel synthesis, the sol was prepared by pouring 3 μmol zirconium propoxide ($Zr(OCH_2CH_2CH_3)_4$, Sigma-Aldrich 70 wt% in 1-propanol) in 15 mL 2-propanol and stirring at 70 ºC for 1 h. Then the sol-gel was coated on the ZnO nanowires at 2000 rpm for 200 s and then baked at 130 ºC for 1 h to perform a sol-gel process. Finally, the ZnO/ZrO_2 core-shell nanowires were annealed at various temperature and time conditions (400-1000 ºC, 5 min-7 days) in air and vacuum (10^{-5}-10^{-3} Pa). To discuss the molecular behaviors on ZrO_2 surface without influence of ZnO nanowires, ZrO_2 films were also prepared on SiO_2 coated Si (100) substrate as controls.

Sample characterization. Morphology, crystal structure, composition, chemical state and coordination structure of ZnO/ZrO_2 core-shell nanowires and ZrO_2 films were characterized by field emission scanning electron microscopy (FESEM, JEOL JSM-7610F) at accelerating voltage of 15 kV, Transmission electron microscopy (TEM, JEOL JEM-2100F) equipped with energy dispersive x-ray spectroscopy (EDS) at accelerating voltage of 200 kV, X-ray diffraction (XRD, Rigaku SmartLab) with Cu Kα radiation source (45 kV, 40 mA) at scan rate of 2°/s, X-ray photoemission spectroscopy (XPS, Kratos AXIS-ULTRA) with Al Kα radiation source (12 kV, 5 mA, monochromator), Raman spectroscopy and x-ray adsorption fine structure (XAFS,

Kyushu Synchrotron Light Research Center (SAGA Light Source) at beam line BL07) for Zr K-edge using the conversion electron yield mode at room temperature. Fourier transform infrared spectroscopy (FTIR, Thermo Fisher Scientific Nicolet iS50) equipped with MCT (HgCdTe) detector was employed to characterize the adsorbed molecules on the sample surface. For monitoring the temperature dependence on the states of adsorbed molecules, the samples were heated at a given temperature for 5 min and immediately cooled to room temperature in air prior to the FTIR measurements. FTIR spectra were recorded at room temperature.

Analysis of desorbed molecules. For the desorbed molecule analysis, the analyte molecules were first adsorbed on the sample surface. The samples with 2 mm×20 mm size were suspended in 20 mL vial bottle filled with saturated volatile molecule mixture (2-nonanone, nonanal, 1-nonanol and nonanoic acid) and kept for 60 s. Then the samples were transferred to gas chromatograph mass spectrometry (GCMS, Shimadzu GCMS-QP2010 Ultra). The desorbed molecules were analysed by GCMS with inlet temperature control unit (OPTIC-4) and Supelco SLB-IL60 capillary column. Samples were heated from 35 ºC to 300 ºC at a rate of 60 ºC/s and kept during the measurement. The desorption temperatures of molecules were characterized by GCMS (Shimadzu GCMS-QP2020 Ultra) with a capillary column (length of 1 m and internal diameter of 0.1 mm) without stationary phases. The samples were heated at the inlet port from 35 to 500 ºC at a rate of 0.5 ºC/s utilizing a multi-shot pyrolyzer (Frontier Lab EGA-PY-3030D).

Sensor preparation and molecular sensing measurements. For the molecular sensing, a nanowire-sensor hybrid device was employed. A chemisensitive resistor sensor used in this study was fabricated by a customized ink-jet printing system (Musashi Engineering Inc.). Material ink composed of 10 mg/ml polyethylene glycol

(PEG 4000, Aldrich Chemical Co.) and 7.5 mg/ml carbon black (CB2350, Mitsubishi Chemical) with water solvent was deposited on an electrode-patterned chip (details can be seen elsewhere [26,27]). After the deposition, the samples were dried for 3 days at room temperature in N_2 atmosphere. The heater-equipped nanowire chips were fabricated by synthesizing the ZnO/ZrO_2 core-shell nanowires on an electrode-patterned chip. Ti/Pt electrodes (thickness: Ti 1 nm and Pt 100 nm) used for Joule heater were deposited by RF sputtering with metal mask. The nanowire-sensor hybrid device was fabricated by integrating the sensor chip and the heater-equipped nanowire chip on a specially designed print-circuit board (PCB) in a side-by-side manner. The temperature of nanowire chip was controlled by applying voltage to Ti/Pt heater electrodes and evaluated by infrared (IR) thermography camera (Infra Tec, VarioCAM®HD head 900 with IRBIS®3 analysis software). For the molecular sensing measurement, the saturated volatile molecule mixture in 20 mL vial bottle was pumped at a flow rate of 100 mL/min. After 60 s of the molecular adsorption process, the pump was stopped, and the nanowire chip was heated to 130 ºC for 10 s in order to detect the desorbed compounds by the chemisensitive resistor sensor. The sensing response was readout by voltage.

6.4 Results and Discussion

Figure1 showed the morphology and crystal structure of the materials. The schematic of sol-gel ZrO_2 coated ZnO nanowires was presented in Figure 1a, from which ZnO nanowires were initially synthesized, and then sol-gel processed ZrO_2 was coated on ZnO nanowires by spin coating method. Figure 1b showed the overall view of sol-gel processed ZrO_2 (sol-gel for short in this paper) coated ZnO nanowires, the length of ZnO nanowires was about 11 μm. TEM image of single nanowire in Figure

1c exhibited that ZrO_2 was uniformly coated on surface of ZnO nanowire. Figure 1d of EDS clearly showed the element distribution in this ZrO_2 coated ZnO nanowire material. In this work, sputtering processed ZrO_2 was processed as comparison experiment to understand the mechanism of the selectivity. To specifically investigate the crystal structure of sol-gel and sputter processed ZrO_2, both sol-gel and sputter ZrO_2 thin film were formed. Figure 1f of HRTEM, SAED and EELS for sol-gel and sputtering processed ZrO_2 thin film showed that sol-gel ZrO_2 was monoclinic crystalline and sputter ZrO_2 is cubic crystalline[28,29]. EELS peak energy of Zr L-edge for the sputter sample is higher than the sol-gel sample, which was consistent with the trend of binding energies in each sample in following results.

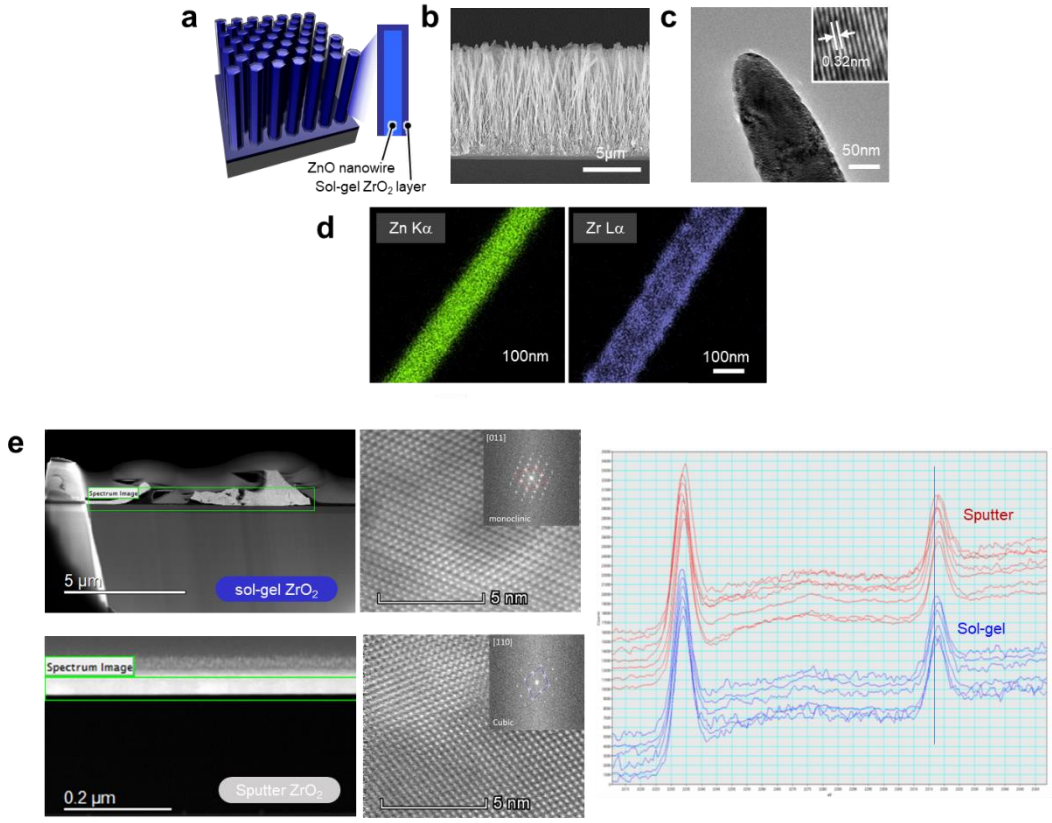

Figure 1 morphology and structure characterization for sol-gel processed ZrO_2 coated ZnO nanowire. a, schematic diagram of sol-gel ZrO_2 coated ZnO nanowires; b, overview SEM of ZrO_2 coated ZnO nanowires; c, TEM of single ZrO_2 coated ZnO nanowire; d, EDS mapping. e, HRTEM, SAED and EELS for sol-gel and sputtering processed ZrO_2 thin film.

Figure 2a shows the molecular selectivity result of sol-gel processed ZrO_2 among mixture gas (2-nonanone, nonanal, 1-nonanol. Nonanoic acid). Sputter processed ZrO_2 (sputter for short in this paper) was utilized as a control group experiment. Compared with sputter ZrO_2 coated ZnO nanowires, sol-gel ZrO_2 coated ZnO showed an extremely high selectivity of 2-nonanone in the mixture gas, desorption of each molecule was 97 nmol for 2-nonanone, 4 nmol for nonanal, 1.3 nmol for 1-nonanol and 0.7 nmol for nonanoic acid. Calibration curve for each molecule was shown in S2. Sputter sample showed no selectivity between 2-nonanone and nonanal. 1-nonanol and

nonanoic acid showed low desorption amount on all surfaces. The molecular occupation in vapor of each molecule was checked (S3a), with which we can find that desorption result on sputter surface was in consistent with molecular ratio in vapor between 2-nonanone and nonanal. Sol-gel processed ZrO_2 thin film (sol-gel TF for short) and sputter processed ZrO_2 (sputter TF) were checked their selectivity in mixture gas, respectively. In thin film cases, even the whole desorption amounts of molecules were limited, the selectively of 2-nonanone still could be clearly seen on the sol-gel processed ZrO_2 surface. For sputter processed ZrO_2 thin film, a similar desorption result among molecules was shown, compared with sputter ZrO_2 coated ZnO nanowire. With selectivity result on bare thin film surface, we could exclude that impact of ZnO NWs on selectivity. The result clear showed that the selectivity of 2-nonanone on sol-gel was coming from the sol-gel processed ZrO_2, and the ZnO nanowires as a platform provided a large surface for enough molecular amount in adsorption.

We have assumed ZrO_2 as high thermally robust surface, desorption result for 2-nonanone on surface in Figure 2b verified this assumption. Sol-gel processed ZrO_2 was annealed at high temperature from 400 to 1000 ^oC, and the recognition of 2-nonanone on this surface kept almost no change until 800 ^oC. Sol-gel processed ZrO_2 thin film was also annealed from 400 to 1000 ^oC (S4), the desorption result showed that the recognition of 2-nonanone in mixture kept until 800 ^oC, which was similar with sol-gel coated NWs. Figure 2c showed that recognition property of 2-nonanone on this surface will not change even after annealing in air at 400 ^oC for 7 days. We also checked the lifetime of this ketone recognition surface at other annealing temperature as shown in S5. This ketone recognition surface showed the high thermal stability and long-time endurance even heated at 800 ^oC for 7 days. When heating temperature increasing to 900 ^oC, decline of selectivity had appeared after 1 day annealing. When sol-gel sample

was annealed at 1000 ^{o}C, the selectivity of 2-nonanone disappeared after annealed for 15 min. Based on these results, we used Arrhenius plot to simulate the lifetime of this sol-gel processed ZrO_2 ketone recognition in figure 2d, we calculated the lifetime at 400 ^{o}C should be near 3×10^{7} years. This extremely long lifetime strongly supported that this ketone recognition surface was valuable for practical application. Furthermore, we also made a comparison between sol-gel and sputter in Figure S6, sputter samples were annealed from 400 to 800 ^{o}C to check their selectivity. The results showed that higher temperature helped nothing with the selectivity on sputter ZrO_2 surface.

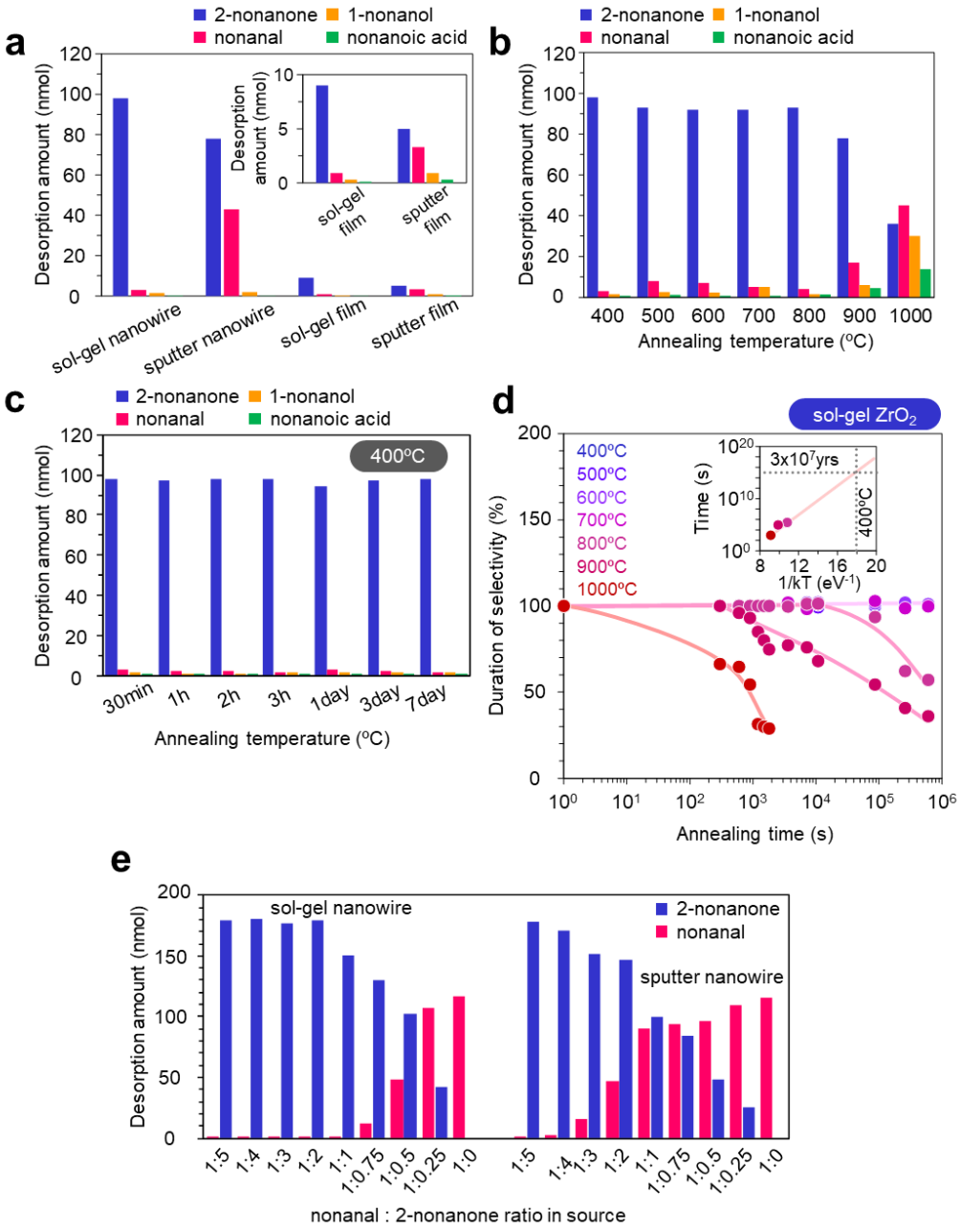

Figure 2 Sol-gel processed ZrO_2 showed thermal stability and selectivity of 2-nonanone in structural similar mixture gas. a, Desorption amounts of volatile molecules (2-nonanone, nonanal, 1-nonanol, nonanoic acid) on sol-gel ZrO_2 coated ZnO nanowires (sol-gel nanowire), sputter ZrO_2 coated ZnO nanowires (sputter nanowire), sol-gel ZrO_2 film (sol-gel film) and sputter ZrO_2 film (sputter film). Inset shows the magnified data for sol-gel film and sputter film.; b, Annealing temperature dependence and (c) annealing time dependence on desorption amounts of volatile molecules (2-

nonanone, nonanal, 1-nonanol, nonanoic acid) on sol-gel ZrO_2 coated ZnO nanowires. For the annealing temperature dependence, the annealing time was 30 min. For the annealing time dependence, the annealing temperature was 400 ºC; d, Duration of selectivity in desorbed molecules as a function of annealing time with varying the annealing temperature. The selectivity and its duration were evaluated as an amount ratio of desorbed 2-nonanone and nonanal, and as degradation by normalizing the initial state to be 100 %. Inset shows the duration time at 50 % selectivity when varying the annealing temperature. For all samples, the annealing was performed in air; e, Desorption amounts of 2-nonanone and nonanal on sol-gel nanowire and sputter nanowire when varying their mixing ratio of liquid source. Prior to the measurements, the samples were annealed at 400 ºC in air.

Meanwhile, the selectivity result made it necessary to notice the huge difference between 2-nonanone and nonanal on sol-gel and sputter ZrO_2 surface. To find out why only sol-gel sample had selectivity for 2-nonanone, we should first find out what has happened to nonanal on the surface of Sol-gel. To fully investigate why this selective result of 2-noannone has shown on the surface, we only checked the desorption result with 2-nonanone and nonanal and changed the ratio of 2-nonanone and nonanal specifically. The ratio of nonanal to 2-nonanone was changed from 1:5 to 1:0. Figure 2e showed the desorption result on sol-gel nanowire and sputter nanowire surface. The ratio of nonanal and 2-nonanone at headspace were also checked (S3b). Sol-gel nanowire surface showed the obvious selectively for 2-nonanone until the ratio of nonanal : 2-nonaone was 1 : 0.5, which meant the amount of nonanal was 2 times higher that 2-nonanone in the mixture. At the same time, desorption result on sputter nanowire surface was consistent with the ratio of nonanal : 2-nonanone in the mixture, further demonstrated sputter ZrO_2 surface had no selectivity for 2-nonanone in the mixture.

Result in figure 2e showed that both nonanal and 2-nonanone could be adsorbed and desorbed on sol-gel surface, so the selectivity was neither coming from the exclusive adsorption of 2-nonanobe nor stronger connection between nonanal and sol-gel surface. After the ratio of nonanal : 2-nonanone decreased under 1:1, there was no obvious threshold of this 2-nonaone selectivity, which indicated that adsorb competition between nonanal and 2-nonanone was not the main factor for the 2-nonaone selectivity result on sol-gel surface.

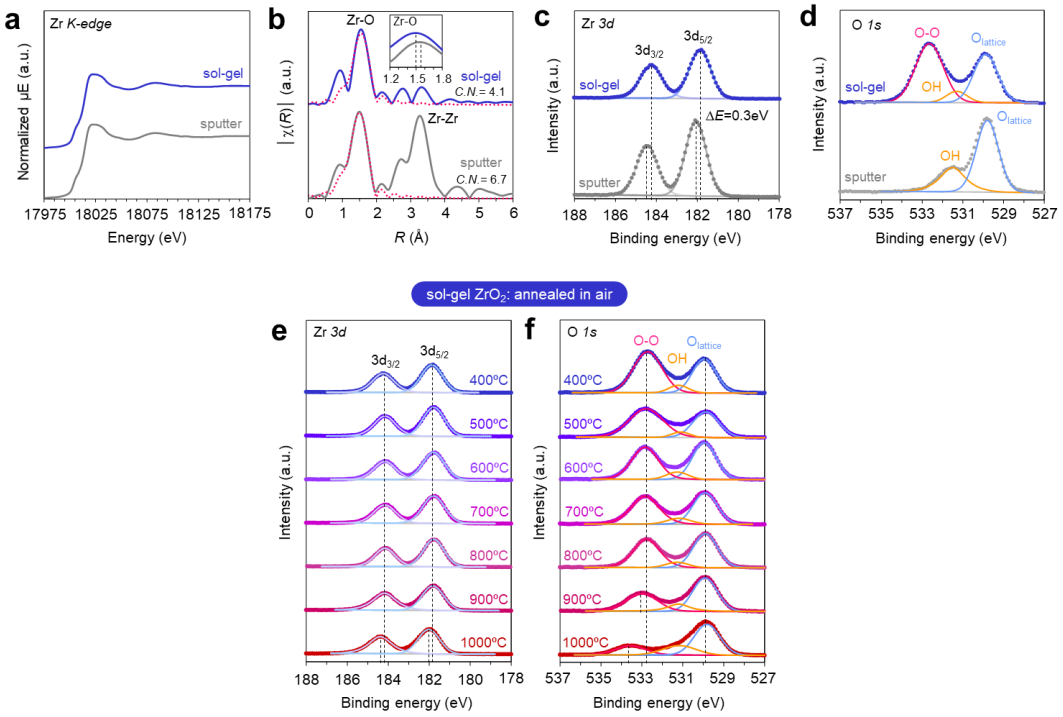

Figure 3. (a) Zr K-edge XANES spectra and (b) EXAFS spectra of sol-gel ZrO_2 film and sputter ZrO_2 film. Inset of (b) shows the magnified data around the Zr-O peak top. (c) Zr 3d and (d) O 1s XPS spectra of sol-gel ZrO_2 film and sputter ZrO_2 film. Prior to XANES, EXAFS and XPS measurements, the samples were annealed at 400 ºC in air. (e,f) Annealing temperature dependence on (e) Zr 3d and (f) O 1s XPS spectra of sol-gel ZrO_2 film annealed in air. (g,h) Annealing temperature dependence on (e) Zr 3d and (f) O 1s XPS spectra of sputter ZrO_2 film annealed in vacuum (10^{-3} Pa). All the measurements were conducted at room temperature.

Based on above result, we considered the different surface structure between sol-gel and sputter should be possible reason result in this selectivity result. X-ray absorption near edge structure (XANES) in Figure 3a and X-ray absorption fine structure spectroscopy (EXAFS) in Figure 3b were probed to check the local lattice distortion of sol-gel and sputter ZrO_2 thin film. Figure 3a, b and S7 indicated that sol-gel showed more unsaturated coordination site than sputter ZrO_2, which indicated that sol-gel surface should have a higher active surface[30,31]. As the sol-gel and sputter samples had same crystal phase, the selectivity was probably coming from the difference in surface. 2-nonanone and nonanal should have different interaction with sol-gel and sputter surface, which resulted in this salient selectivity. XPS characterization was used for surface chemistry investigation. Figure 3c and d showed the XPS spectra of Zr 3d and O 1s regions of ZrO_2 in sol-gel and sputter samples, respectively. XPS spectra for Zr 3d exhibited two peaks as Zr $3d_{3/2}$ and Zr $3d_{5/2}$.[32] For sol-gel, the binding energy at Zr $3d_{3/2}$ and $3d_{5/2}$ were 184.2 eV and 182.8 eV, respectively. For sputter, the binding energy at Zr $3d_{3/2}$ and $3d_{5/2}$ were 184.5 eV and 182.1 eV, respectively. Binding energy of Zr shifted negatively to lower energies from sputter to sol-gel, 0.3 eV, indicating that the electron-equilibrium structure of metal sites in sol-gel had an electron-richer structure. Figure 3d showed the O 1s XPS spectra. The lower binding energy at ~529.9 eV and 531.6 eV were ascribed to the lattice oxygen ($O_{lattice}$) and hydroxy-like groups (O-H).[33] The O species at 532.8 eV was typical for adsorbed O-O bonds.[34] The lattice oxygen and O-H groups had negligible changes in sol-gel and sputter samples. However, an obvious increase in intensity of adsorbed free oxygen (O-O) was observed in sol-gel only, suggesting that the surface of sol-gel had much higher oxidizing than sputter. In Figure S7, the R space XAFS and K-edge XANES spectra was in line to the XPS results. According to the previous thermal stability result, we also annealed the sol-gel thin film

from 400 to 1000 ^{o}C and checked their XPS spectrum, respectively. The XPS spectrum for Zr_{3d} in figure 3e showed there was no chemical state change for Zr in the annealing process. While for O_{1s} XPS spectrum, the peak for O-O showed an obvious decrease after annealed at 900 ^{o}C and shift 0.4 eV from original peak position. Furthermore, the O-O peak disappeared at 1000 ^{o}C, and a new peak located at 533.7 eV formed, which indicated that the chemical state was totally different from 400 ^{o}C. Based on the O-O site in sol-gel sample, we assumed that if we can use the vacuum annealing method to create O-O site in sputter sample, we probably can get the 2-nonanone selectivity result on sputter sample. We annealed the sputter ZrO_2 nanowires in vacuum at 800 ^{o}C, but result showed no selectivity for 2-nonanone. Meanwhile, XPS results for vacuum annealed sputter ZrO_2 thin film indicated that O-O site could not be created under this process. This result also supported O-O site was the main factor for 2-nonanone selectivity from the side.

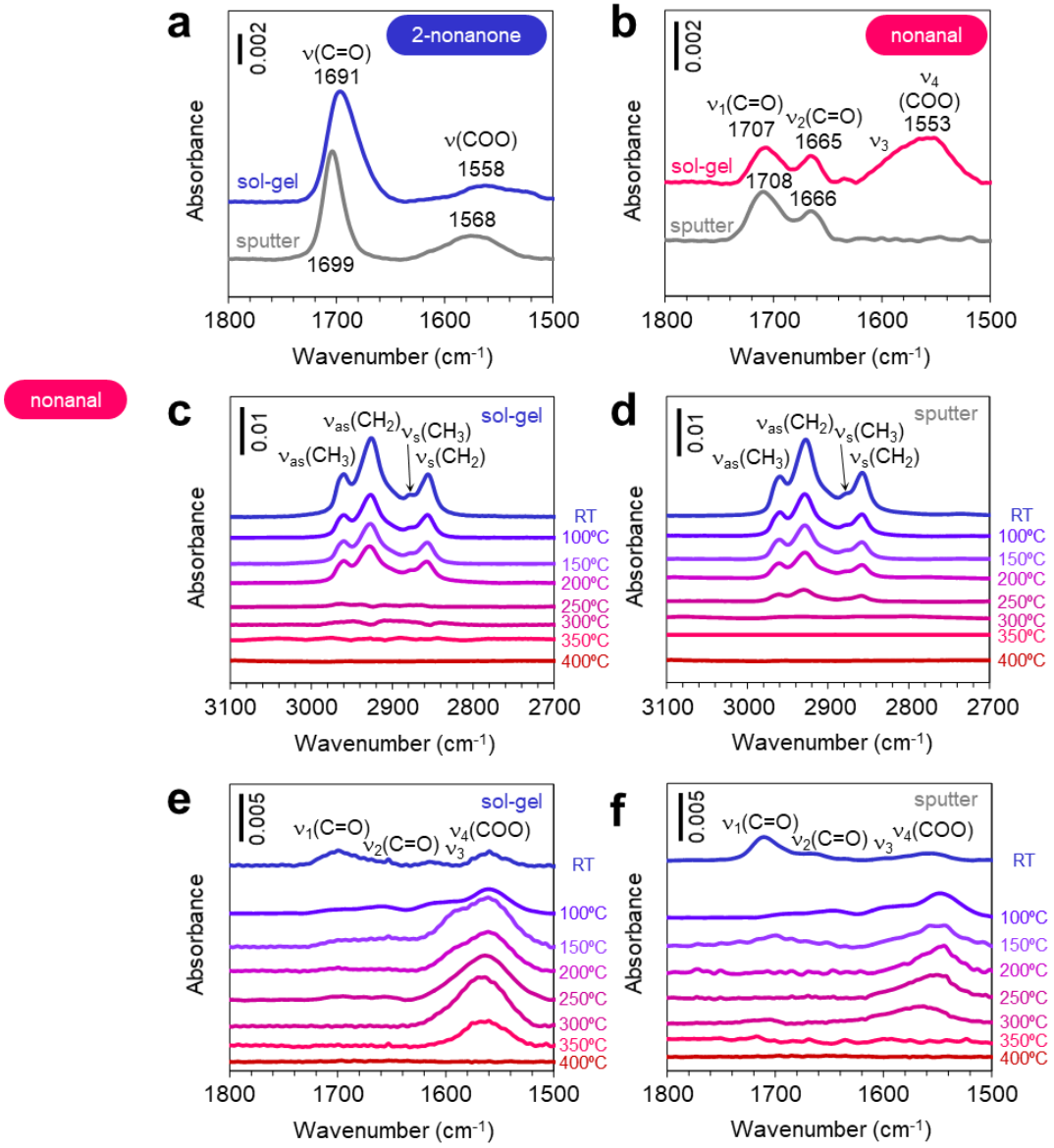

Figure 4. (a,b) FTIR spectra of (a) 2-nonanone and (b) nonanal adsorbed on sol-gel ZrO_2 coated ZnO nanowires and sputter ZrO_2 coated ZnO nanowires. (c-f) Temperature dependent FTIR spectra of nonanal adsorbed on (d,f) sol-gel ZrO_2 coated ZnO nanowires and (d,f) sputter ZrO_2 coated ZnO nanowires. (c,d) Alkyl region and (e,f,) carbonyl and carboxyl regions, respectively. For the temperature dependence, the samples were annealed for 5 min at given temperature in air. All measurements were conducted at room temperature. Prior to the measurements, the samples were annealed at 400 ºC in air.

The change in surface chemistry for oxidation on sol-gel ZrO_2 surface was anticipated to influence the interaction of molecule-to-surface. Further, the desorption result of 2-nonanone and nonanal showed selectivity. S9 showed the desorption result for mixture and single gas species 2-nonanone by GC-MS. The desorption amount of 2-nonanone in single gas species was a little higher than mixture, which meant some parts of the sol-gel surface were occupied by nonanal. To fully understand what has happened, we then carried out the FT-IR to examine the state of molecule on surface as shown in Figure 4. Firstly, with the FT-IR spectra of molecule-to-surface for after adsorption and after desorption, we can clear see there was no molecule remain on sol-gel surface, which meant all molecules were fully desorbed at 400 ^oC (Figure S10).

Figure 4a and 4b compared the adsorption states of 2-nonanone and nonanal on sol-gel and sputter ZrO_2, respectively. For 2-nonanone, the peaks at 1691 and 1699 cm^{-1} were signed to the C=O stretching vibration ν(C=O), which were considered as physical adsorption. Peaks at 1558 and 1568 cm^{-1} were attributed to the ν_{as} (OCO) signal of carboxylate species which represented the molecular oxidation on metal oxide surface.[35] The blue shift of both ν(C=O) and ν_{as} (COO) indicated a stronger bonding of 2-nonanone on sol-gel surface than on sputter surface, due to the higher O-O oxygen on sol-gel surface. As for nonanal case, the O-O oxygen leaded to completely different result. The FT-IR spectra of nonanal adsorbed on sol-gel and sputter ZrO_2 were shown in Figure 4b. Peaks at 1707 and 1665 cm^{-1} on sol-gel (red line) for C=O vibration[36] indicated the interactions between the carbonyl groups and the ZrO_2 surface. Such C=O vibration peaks on sputter ZrO_2 surface (blue line) were located at 1708 and 1666 cm^{-1}. There was no significant difference for C=O vibration between sol-gel and sputter. However, nonanal on sol-gel showed a huge peak at ν_{as} (OCO) position, 1566 cm^{-1}, where sputter showed almost no peak. This difference strongly indicated that a strong

oxidation has happened for nonanal on sol-gel surface. This strong oxidation was coming from the O-O oxygen on sol-gel ZrO_2. Compare with 2-nonanone, nonanal was more easily to be oxidized. When the surface had huge amount of free oxygen, 2-nonanone as ketone structure had strong physical bonding strength with the surface rather than being oxidized, while nonanal as aldehyde structurally preferred to be oxidized on the high oxidation surface. Based on above results and discussions, we proposed a possible mechanism for the interact process of nonanal and 2-nonanone on sol-gel surface. When the mixture gas approaching the sol-gel surface, 2-nonanone will make a stable bonding with ZrO_2 surface with its ketone site C=O. For nonanal, aldehyde site C=O was more easily to be oxidized, when it attached with the highly oxidation O-O, a chemistry bonding formed (high ν_{as} (OCO) peak). This comparison of nonanal on sol-gel and sputter was much more obvious than 2-nonanone. Figure 4 c, d, e, and f showed the temperature dependence adsorption state of nonanal during the desorption process on sol-gel and sputter surface. Figure 4c and d showed the alky chain part while figure 4e and f showed the carboxylate part for nonanal on sol-gel and sputter surface respectively. From figure 4c and d, it was clear that carbonyl group in nonanal had fully removed at 250 ^{o}C on sol-gel surface, which was fully removed from sputter surface until 300 ^{o}C. From 4e and f, there was a huge COO peak on sol-gel appeared after 100 ^{o}C, which didn't disappear until 400 ^{o}C. But there was no huge COO peak on sputter surface compare with on sol-gel surface. These FT-IR spectrums strongly supported that nonanal was strongly oxidized and carboxylate part had strong bonding on sol-gel surface, while on sputter surface, nonanal was slightly connected to surface. The increase COO peak on sol-gel from room temperature to 300 ^{o}C indicated that the oxidation of nonanal increased with the temperature. During desorption process, nonanal will burn into small molecules which cannot be detected by GC-MS (S9a). For

2-nonanone, it could be kept as 2-nonanone on so-gel surface during the desorption process (S9). S11 showed the desorption process of 2-nonaonone and nonanal on sol-gel and sputter surface by FT-IR. The spectrums exhibited that there was no big difference of 2-nonanone during desorption process on sol-gel and sputter surface. Meanwhile, we still can observe that the bonding strength of 2-nonanone on sol-gel was stronger that sputter.

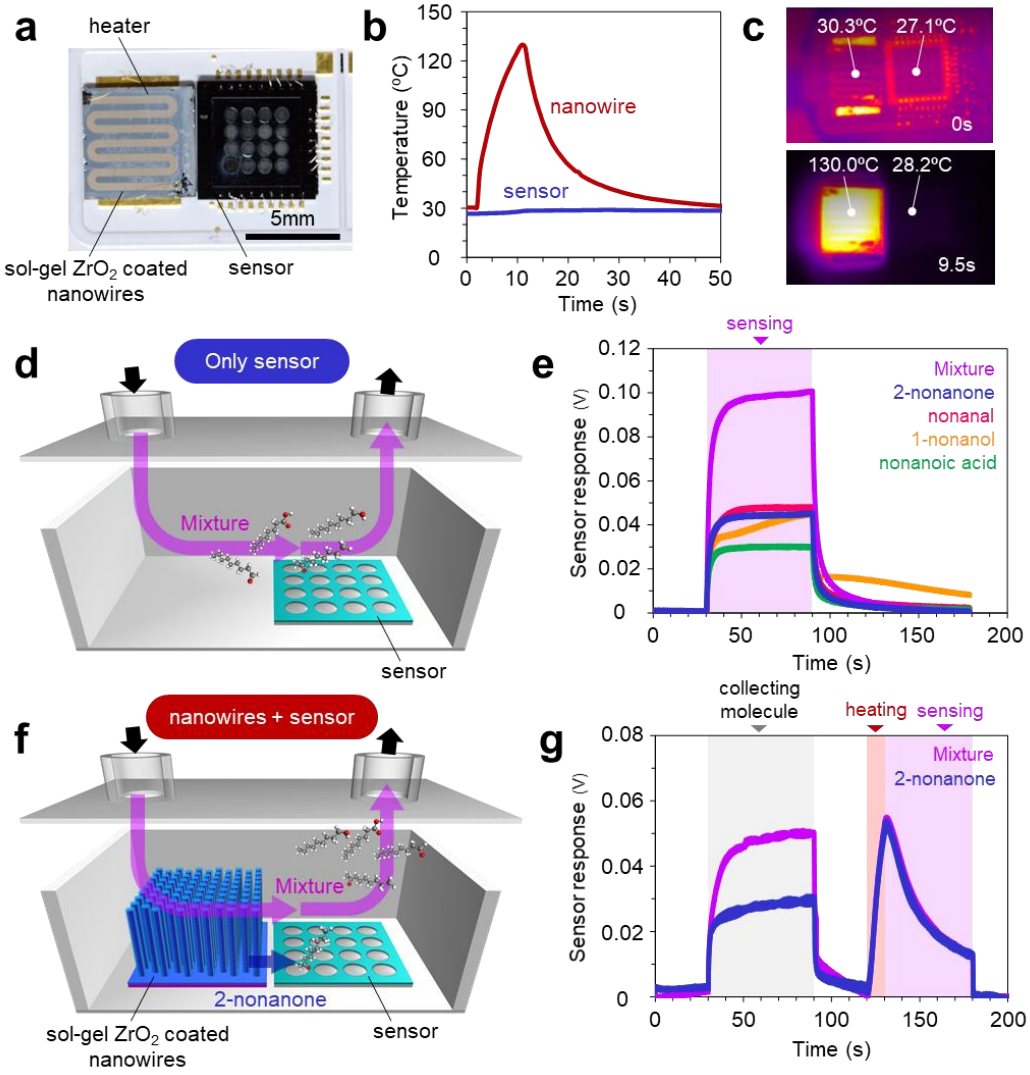

Figure 5. (a) Photograph of a nanowire-sensor hybrid device. (b) Temperature profiles of nanowire chip and sensor chip when applying 15 V to the heater. (c) Thermographic images of a nanowire-sensor hybrid device taken at 0 s (upper) and 9.5 s (lower) after the voltage apply. (d) Schematic illustration of molecular sensing measurement and (e) sensor responses to various volatile molecule analytes performed by only a sensor chip. (d) Schematic illustration of molecular sensing measurement and (g) sensor responses to volatile molecule analytes performed by a nanowire-sensor hybrid device. The nanowire chip is composed of sol-gel ZrO_2 coated ZnO nanowires, which was annealed at 400 ºC in air. For (e) and (g), mixture consists of 2-nonanone,

nonanal, 1-nonanol and nonanoic acid. The molecular sensing measurement for a nanowire-sensor hybrid device was conducted by 60 s molecular collection, 10 s heating for releasing molecules from nanowire surface and 50 s sensing. The heating and the sensing processes were performed without flowing carrier gas.

Since this O-O oxygen rich surface formed by sol-gel process had such salient selectivity for ketone in mixture, it should have the ability to be used as molecular selector for sensor in complex mixture. Here, we demonstrated its ability by using a hybrid device with sensor. By checking the desorption temperature for mixture, we found that 130 ^{o}C was a suitable working temperature for molecular selector. Figure 5 showed the sensor signal from single 2-nonanone gas species was same with signal from mixture gas species. Figure 5a was a photo for sol-gel ZrO_2 coated nanowires molecular selector integrated with 16 channeled chemo resistive sensor. Figure 5b was the thermal spectrum for ZrO_2 coated nanowire and sensor during the heating process. We also used thermal camera to check the temperature for sensor and molecular selector in heating process. The molecular selector was 27.1 ^{o}C and sensor was 30.3 ^{o}C at initial state 0 s, the molecular selector changed to 28.2 ^{o}C and sensor increased to 130 ^{o}C after heating process at 9.5 s. The sensing response was checked by only sensor method as comparison experiment. Figure 5d showed the schematic of sensing process. In this only sensor process, molecules will catch the sensor material surface directly. Both mixture and single gas species sensing results were checked by this only sensor way. Sensing spectrum clearly reflected that it was difficult to distinguish single gas species from the mixture (figure 5e). Figure 5f was the schematic of sensing process for molecular selector-sensor integrate device. There were two steps for ketone sensing in this device. First step was for collecting molecules which was same as only sensor

device. Second step was partly included in first step. Molecules will first arrive at the sol-gel ZrO_2 coated nanowire surface and been adsorbed, other molecules will be flowed away by carrier gas; after adsorption, the heating process will remove the adsorbed molecules and the sensor will detect the desorbed molecules. Figure 5g showed the molecular collection and sensing process. Sensing response for mixture and single gas species 2-nonane was totally different. While after heating the molecular selector, sensing response was same for mixture and 2-nonanone. The spike signal came from the decreasing amount of molecular desorption from nanowire surface. This result demonstrated this sol-gel processed O-O rich surface could be utilized as ketone molecular selector for improving sensing performance. This technique also had been introduced to other chain length ketone involved mixture such as C8 and C11, which also showed satisfying selectivity result of ketone in mixture by GC-MS (Figure 6). Ketone recognition also realized in C8 and C11mixture by GC-MS, which meant this sol-gel surface could be utilized in other chain length ketone sensing.

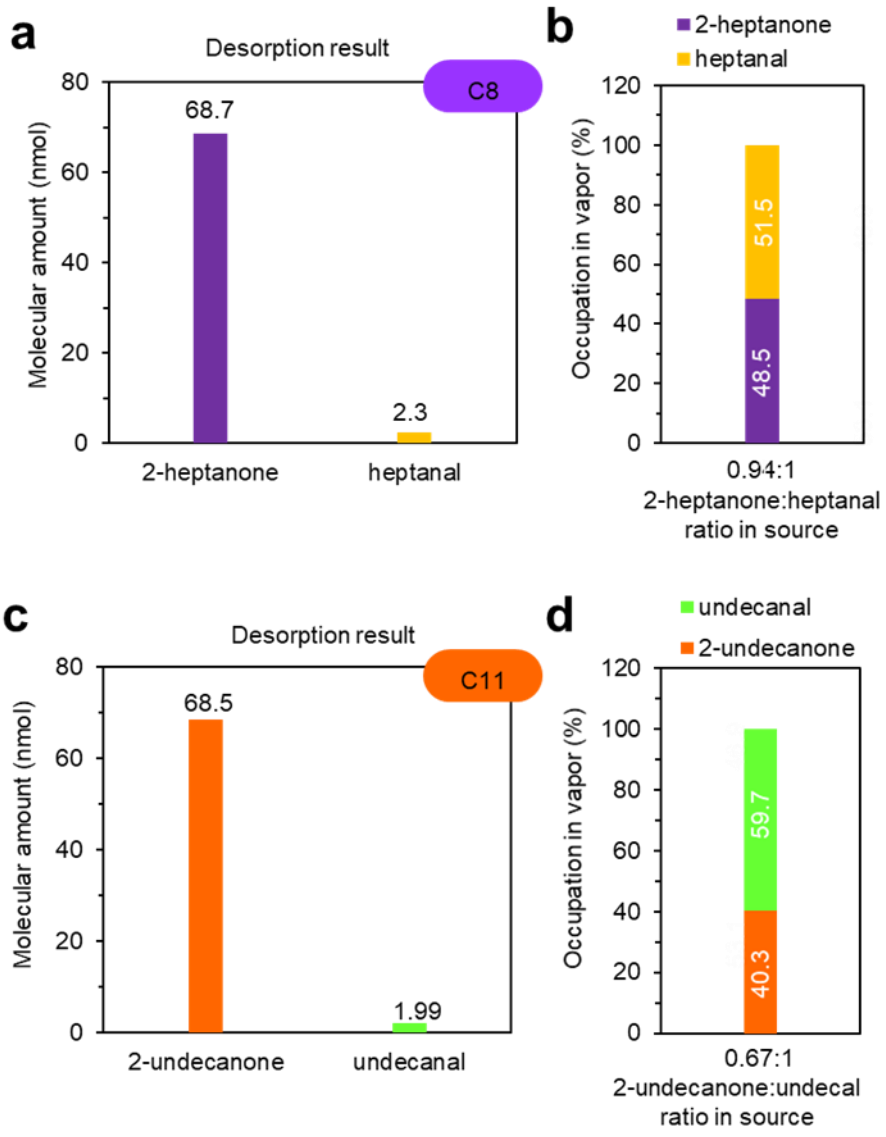

Figure 6 Selectivity result for ketone in C11 and C8 mixture. a, desorption result on sol-gel processed ZrO_2 for C8 mixture--heptanal and 2-heptanone; b, ratio of heptanal and 2-heptanone in mixture gas phase; c, desorption result on sol-gel processed ZrO_2 for C11 mixture--undecanal and 2-undecanone; d, ratio of undecanal and 2-undecanone in mixture gas phase.

6.5 Conclusions

In summary, we reported a study of discriminating ketone in mixture based on promoted reactivity on metal oxide surface, using 2-nonanone, nonanal, 1-nonanol, nonanoic acid as model compound, ZrO_2 as thermally robust metal oxide surface. 2-nonanone and nonanal showed similar desorption result on unpromoted reactivity surface (sputter ZrO_2), while O-O oxygen rich surface (sol-gel ZrO_2) exhibited extraordinary selectivity of 2-nonaone in mixture. The sol-gel process created huge amount of free oxygen on ZrO_2 surface, which provided a stronger physical bonding for ketone. Meanwhile, based on the chemistry property of nonanal, a chemistry bonding was formed between O-O and aldehyde. Further, during the desorption process, nonanal cannot easily desorbed from the surface and burned into very small molecules. FT-IR spectra provided a clear picture of the oxidation of nonanal on sol-gel surface. Further demonstration of this ketone selectivity based on reactivity promotion was tested by other chain length molecules as C8 and C11 mixture. Based on above finding, a molecular selector of ketone for sensor was conducted, and the integrate molecular selector-sensing device showed excellent ketone sensing result in mixture gas.

6.6 References

(1) Chen H, Yada R. Nanotechnologies in agriculture: new tools for sustainable development[J]. Trends in Food Science & Technology, 2011, 22(11): 585-594.

(2) Mayer M, Baeumner A J. A megatrend challenging analytical chemistry: biosensor and chemosensor concepts ready for the internet of things[J]. Chemical reviews, 2019, 119(13): 7996-8027.

(3) Chen S, Jiang K, Lou Z, et al. Recent developments in graphene-based tactile sensors and e-skins[J]. Advanced Materials Technologies, 2018, 3(2): 1700248.

(4) Bohr A, Memarzadeh K. The rise of artificial intelligence in healthcare applications[M]//Artificial Intelligence in healthcare. Academic Press, 2020: 25-60.

(5) Balkenhohl F, von dem Bussche-Hünnefeld C, Lansky A, et al. Combinatorial synthesis of small organic molecules[J]. Angewandte Chemie International Edition in English, 1996, 35(20): 2288-2337.

(6) Sasaki H, Scholl D, Parsons M, et al. Development of an Al2O3/ZrO2-composite high-accuracy NOx sensor[R]. SAE Technical Paper, 2010.

(7) Haefele E, Kaltenmaier K, Schoenauer U. Application of the ZrO2 sensor in determination of pollutant gases[J]. Sensors and Actuators B: Chemical, 1991, 4(3-4): 525-527.

(8) Tan G L, Wu X J. Electronic conductivity of a ZrO2 thin film as an oxygen sensor[J]. Thin Solid Films, 1998, 330(2): 59-61.

(9) Gao N, He C, Ma M, et al. Electrochemical co-deposition synthesis of Au-ZrO2-graphene nanocomposite for a nonenzymatic methyl parathion sensor[J]. Analytica chimica acta, 2019, 1072: 25-34.

(10) Fate W A, Hetrick R E, Vassell W C. Absolute pressure measurements using ZrO2 electrochemical cells[J]. Applied Physics Letters, 1981, 39(11): 924-926.

(11) Tyagi B, Sidhpuria K, Shaik B, et al. Synthesis of nanocrystalline zirconia using sol− gel and precipitation techniques[J]. Industrial & engineering chemistry research, 2006, 45(25): 8643-8650.

(12) Xu J, Zhang Y, Xu X, et al. Constructing La2B2O7 (B= Ti, Zr, Ce) compounds with three typical crystalline phases for the oxidative coupling of methane: the effect of phase structures, superoxide anions, and alkalinity on the reactivity[J]. ACS Catalysis, 2019, 9(5): 4030-4045.

(13) Schild C, Wokaun A, Koeppel R A, et al. Carbon dioxide hydrogenation over nickel/zirconia catalysts from amorphous precursors: on the mechanism of methane formation[J]. The Journal of Physical Chemistry, 1991, 95(16): 6341-6346.

(14) Ding J, Zhao W, Zi L, et al. Promotional Effect of ZrO2 on supported FeCoK Catalysts for Ethylene Synthesis from catalytic CO2 hydrogenation[J]. International Journal of Hydrogen Energy, 2020, 45(30): 15254-15262.

(15) Indovina V, Cimino A, De Rossi S, et al. Nature of the active site for propene hydrogenation on CrOx/ZrO2 catalysts[J]. Journal of molecular catalysis, 1992, 75(3): 305-319.

(16) Huang J, Jiang S, Wang M, et al. Dynamic Evolution of Fe and Carbon Species over Different ZrO2 Supports during CO Prereduction and Their Effects on CO2 Hydrogenation to Light Olefins[J]. ACS Sustainable Chemistry & Engineering, 2021.

(17) Yamaguchi T, Hightower J W. Hydrogenation of 1, 3-butadiene with 1, 3-cyclohexadiene and molecular deuterium over zirconium dioxide catalysts[J]. Journal of the American Chemical Society, 1977, 99(12): 4201-4203.

(18) Nakano Y, Yamaguchi T, Tanabe K. Hydrogenation of conjugated dienes over ZrO2 by H2 and cyclohexadiene[J]. Journal of Catalysis, 1983, 80(2): 307-314.

(19) Chowdhury I A. Zirconia catalyst and acid-base bifunctional catalysis by zirconia[D]. Lamar University-Beaumont, 1998.

(20) Shane M, Mecartney M L. Sol-gel synthesis of zirconia barrier coatings[J]. Journal of materials science, 1990, 25(3): 1537-1544.

(21) Kim J, Lin Y S. Sol-gel synthesis and characterization of yttria stabilized zirconia membranes[J]. Journal of membrane science, 1998, 139(1): 75-83.

(22) Wang J A, Valenzuela M A, Salmones J, et al. Comparative study of nanocrystalline zirconia prepared by precipitation and sol–gel methods[J]. Catalysis today, 2001, 68(1-3): 21-30.

(23) Y. He, T. Yanagida, K. Nagashima, F. W. Zhuge, G. Meng, B. Xu, A. Klamchuen, S. Rahong, M. Kanai, X. M. Li, M. Suzuki, S. Kai and T. Kawai, J. Phys. Chem. C 2013, 117, 1197-1203.

(24) D. Sakai, K. Nagashima, H. Yoshida, M. Kanai, Y. He, G. Zhang, X. Zhao, T. Takahashi, T. Yasui, T. Hosomi, Y. Uchida, S. Takeda, Y. Baba and T. Yanagida, Sci. Rep. 2019, 9, 14160.

(25) X. Zhao, K. Nagashima, G. Zhang, T. Hosomi, H. Yoshida, Y. Akihiro, M. Kanai, W. Mizukami, Z. Zhu, T. Takahashi, M. Suzuki, B. Samransuksamer, G. Meng, T. Yasui, Y. Aoki, Y. Baba and T. Yanagida, Nano Lett. 2020, 20, 599-605.

(26) Y. Akihiro, K. Nagashima, T. Hosomi, M. Kanai, H. Anzai, T. Takahashi, G. Zhang, T. Yasui, Y. Baba and T. Yanagida, ACS Omega 2019, 4, 8299-8304.

(27) Q. Liu, T. Yasui, K. Nagashima, T. Yanagida, M. Hara, M. Horiuchi, Z. Zhu, H. Takahashi, T. Shimada, A. Arima and Y. Baba, J. Phys. Chem. C 2020, 124, 20563-20568.

(28) Axelsson K O, Keck K E, Kasemo B. Surface compositional changes of ZrO2 in H2O, H2 and atomic hydrogen, investigated by aes and eels[J]. Applied surface science, 1986, 25(1-2): 217-230.

(29) Gritsenko V, Gritsenko D, Shaimeev S, et al. Atomic and electronic structures of amorphous ZrO2 and HfO2 films[J]. Microelectronic engineering, 2005, 81(2-4): 524-529.

(30) Akiyama D, Akiyama H, Uehara A, et al. Phase analysis of uranium oxides after reaction with stainless steel components and ZrO2 at high temperature by XRD, XAFS, and SEM/EDX[J]. Journal of Nuclear Materials, 2019, 520: 27-33.

(31) Choy J H, Yoon J B, Park J H. In situ XAFS study at the Zr K-edge for SiO2/ZrO2 nano-sol[J]. Journal of synchrotron radiation, 2001, 8(2): 782-784.

(32) Reddy B M, Chowdhury B, Smirniotis P G. An XPS study of the dispersion of MoO3 on TiO2–ZrO2, TiO2–SiO2, TiO2–Al2O3, SiO2–ZrO2, and SiO2–TiO2–ZrO2 mixed oxides[J]. Applied Catalysis A: General, 2001, 211(1): 19-30.

(33) Reddy B M, Sreekanth P M, Yamada Y, et al. Surface characterization of sulfate, molybdate, and tungstate promoted TiO2-ZrO2 solid acid catalysts by XPS and other techniques[J]. Applied Catalysis A: General, 2002, 228(1-2): 269-278.

(34) Zhou Z, Chen S, Qin J, et al. Catalytic Enantioselective Intramolecular C (sp3)− H Amination of 2-Azidoacetamides[J]. Angewandte Chemie International Edition, 2019, 58(4): 1088-1093.

(35) Zhang G, Hosomi T, Mizukami W, et al. A thermally robust and strongly oxidizing surface of WO 3 hydrate nanowires for electrical aldehyde sensing with long-term stability[J]. Journal of Materials Chemistry A, 2021, 9(9): 5815-5824.

(36) Wang C, Hosomi T, Nagashima K, et al. Rational method of monitoring molecular transformations on metal-oxide nanowire surfaces[J]. Nano letters, 2019, 19(4): 2443-2449.

6.7 Supporting Information

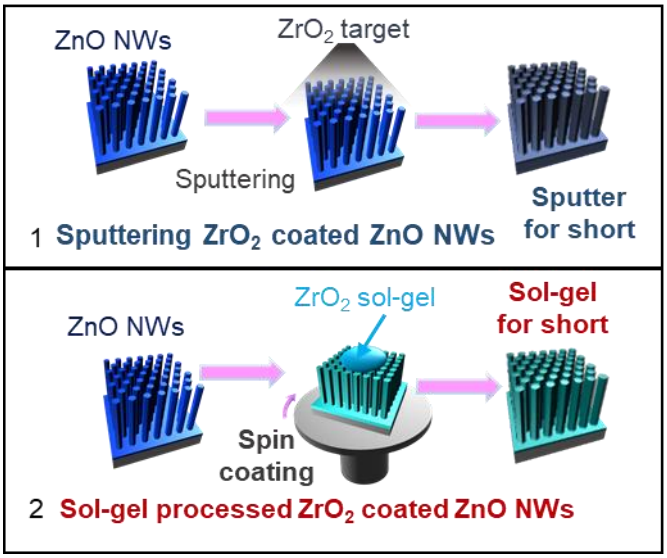

Figure S1. Procession of produce sol-gel and sputter ZrO_2 coated ZnO nanowires, respectively.

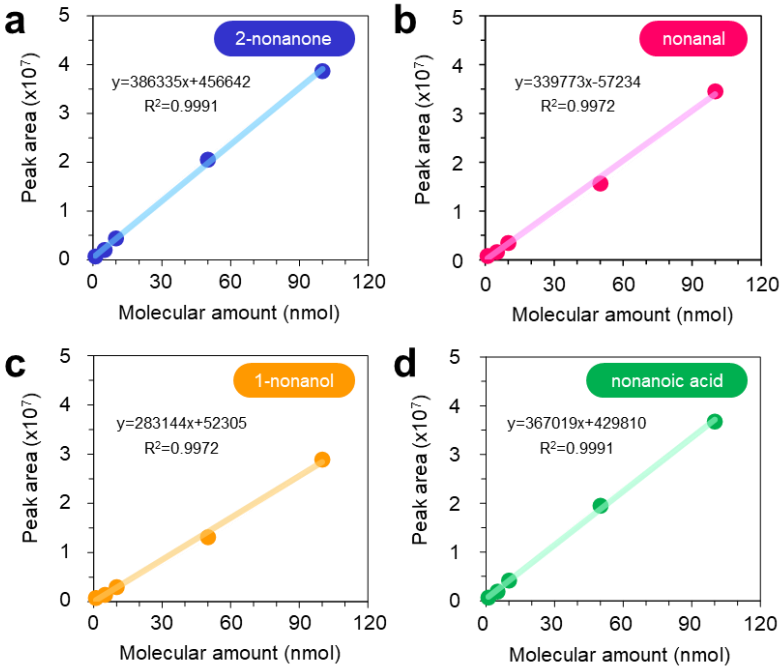

Figure S2. Calibration curves of peak area vs. molecular amount for (a) 2-nonanone, (b) nonanal, (c) 1-nonanol and (d) nonanoic acid in GCMS analyses.

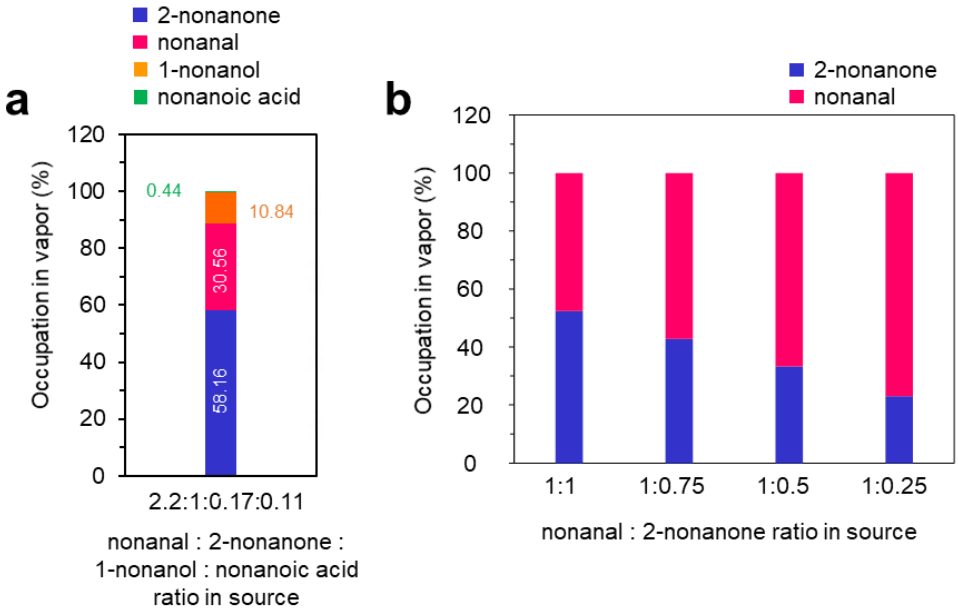

Figure S3. Occupation of analyte volatile molecules at the head space of 20 mL vial bottle (left) when adding equal volume of liquid concentrates (2-nonanone, nonanal, 1-nonanol and nonanoic acid) at the bottom of vial bottle and when varying the volume ratio of 2-nonanone and nonanal (right).

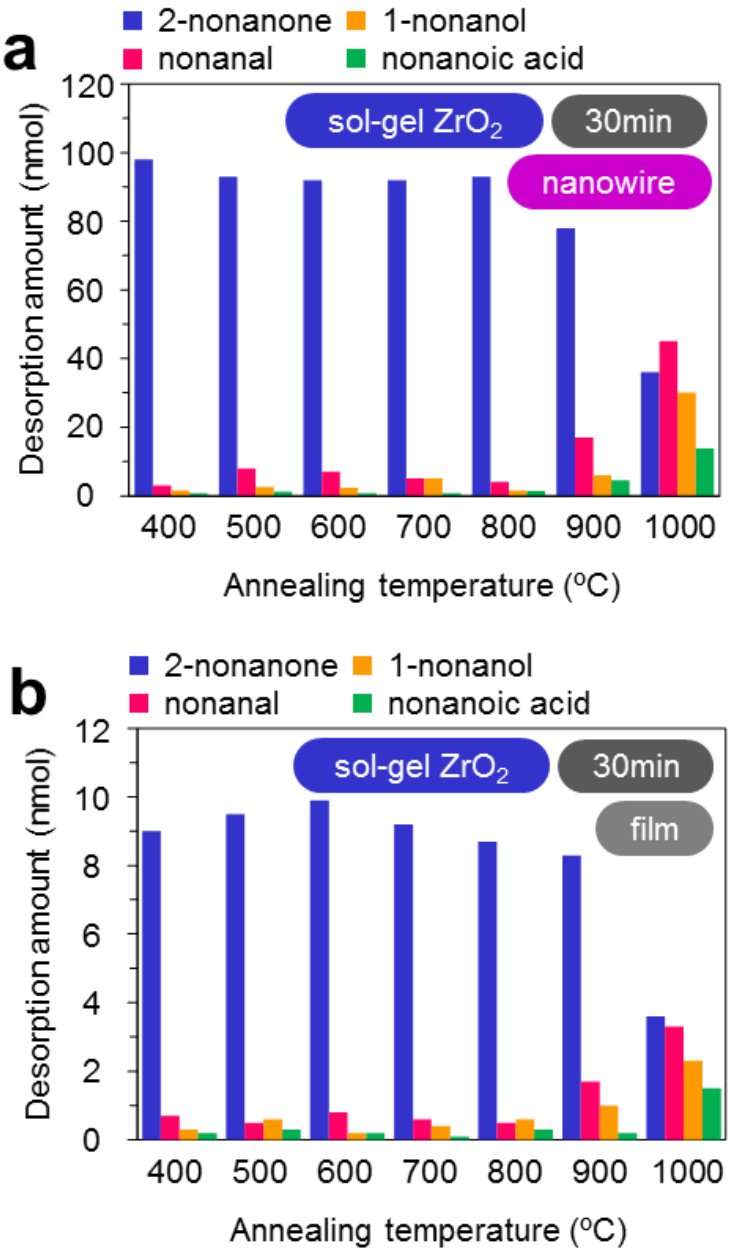

Figure S4. Annealing temperature dependence on desorption amounts of volatile molecules (2-nonanone, nonanal, 1-nonanol, nonanoic acid) on (a) sol-gel ZrO_2 coated ZnO nanowires and (b) sol-gel ZrO_2 film. For the annealing temperature dependence, the annealing time was 30 min. For all samples, the annealing was performed in air.

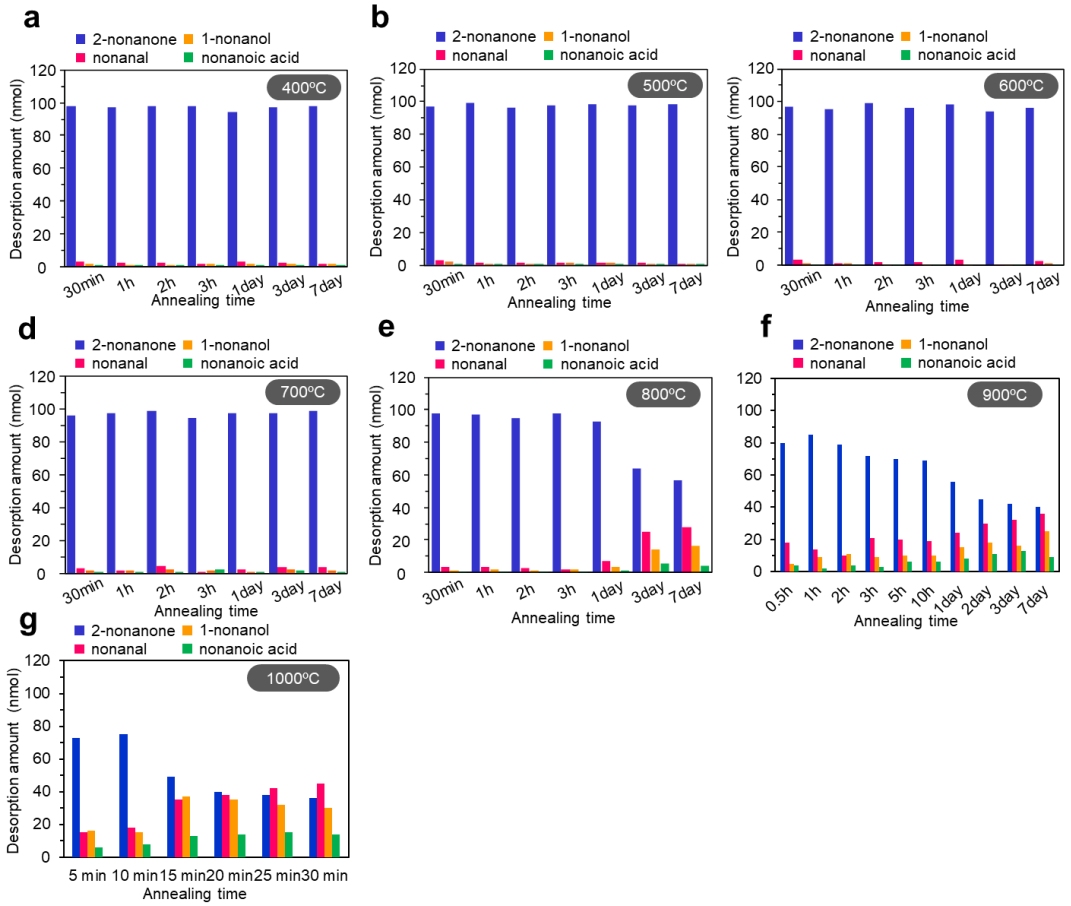

Figure S5. Thermal robustness endurance test of sol-gel processed ZrO2 coated ZnO nanowires by annealing in air. a, desorption result on sol-gel of annealing at 400 °C for 7 days; b, desorption result on sol-gel of annealing at 500 °C for 7 days; c, desorption result on sol-gel of annealing at 600 °C for 7 days; desorption result on sol-gel of annealing at 700 °C for 7 days; d, desorption result on sol-gel of annealing at 800 °C for 7 days; e, desorption result on sol-gel of annealing at 900 °C for 7 days; e, desorption result on sol-gel of annealing at 1000 °C for 30 mins.

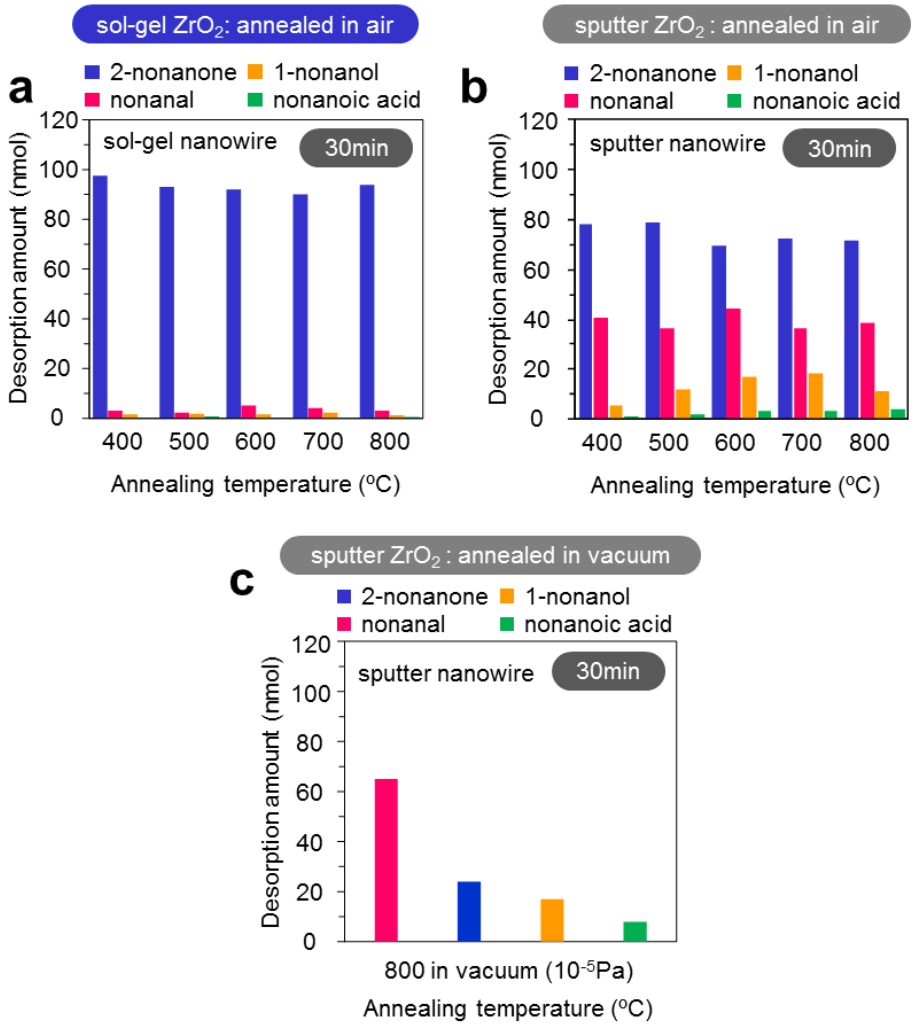

Figure S6. Annealing temperature dependence on desorption amount of volatile molecules (2-nonanone, nonanal, 1-nonanol, nonanoic acid) on (a) sol-gel ZrO_2 coated ZnO nanowires and (b) sputter ZrO_2 coated ZnO nanowires. For these measurements, the samples were annealed in air. (c) Desorption amount of volatile molecules on sputter ZrO_2 coated ZnO nanowires, which were annealed at 800 ºC in vacuum. For all samples the annealing time was 30 min.

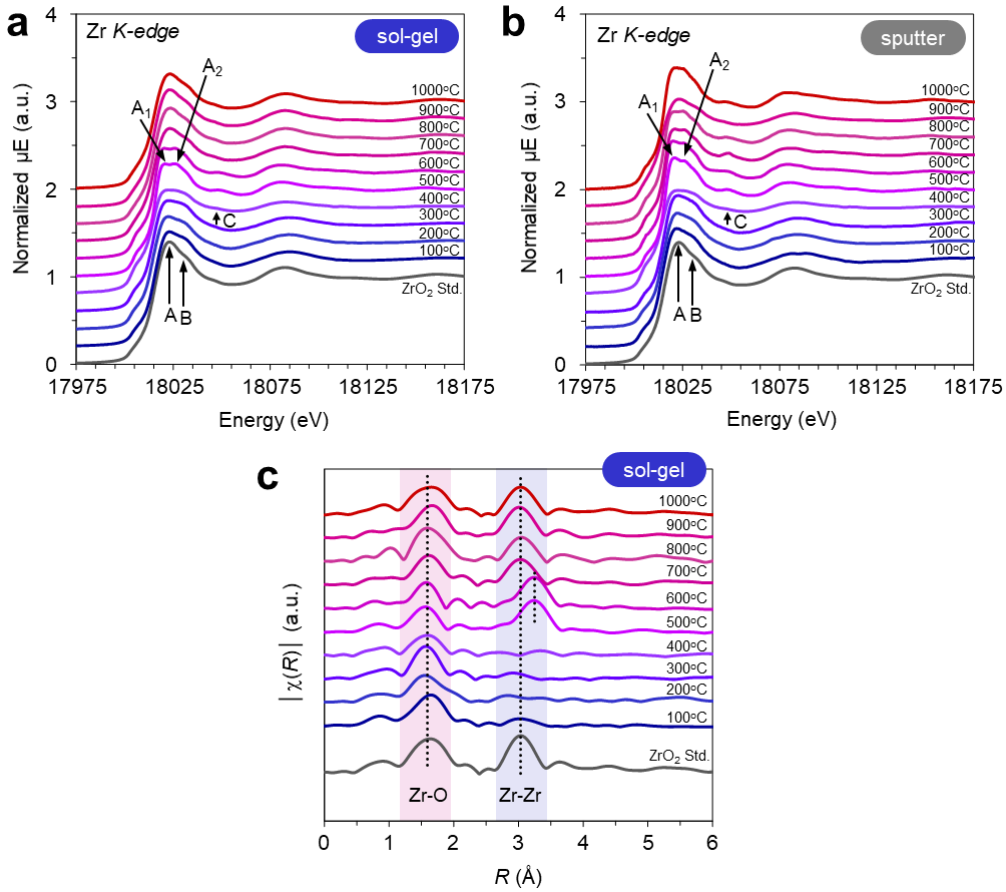

Figure S7. Annealing temperature dependence on Zr K-edge XANES spectra of (a) sol-gel ZrO_2 film and (b) sputter ZrO_2 film. As a comparison, the spectrum of ZrO_2 tablet is also shown. (c) Annealing temperature dependence on EXAFS spectra of sol-gel ZrO_2 film. For all samples, the annealing was performed for 30 min in air.

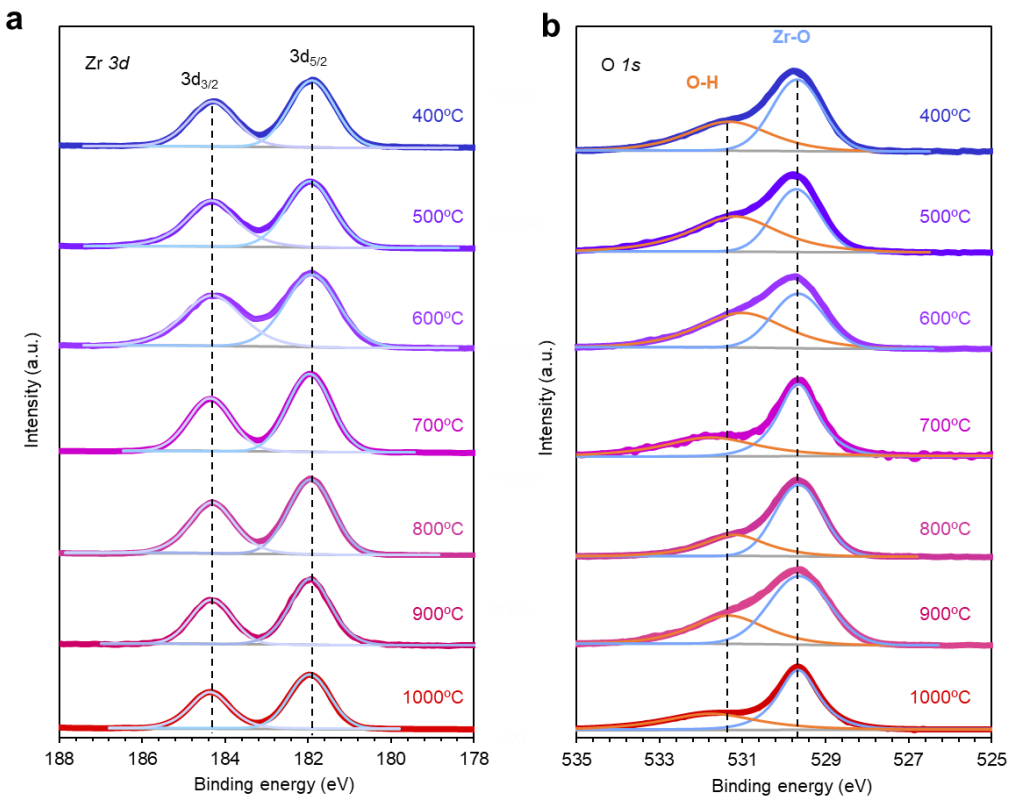

Figure S8. XPS result for sputter processed ZrO_2 annealed in vacuum for 30 min from 400 to 1000 ºC. a, spectrum for Zr 3d; b, spectrum for O 1s.

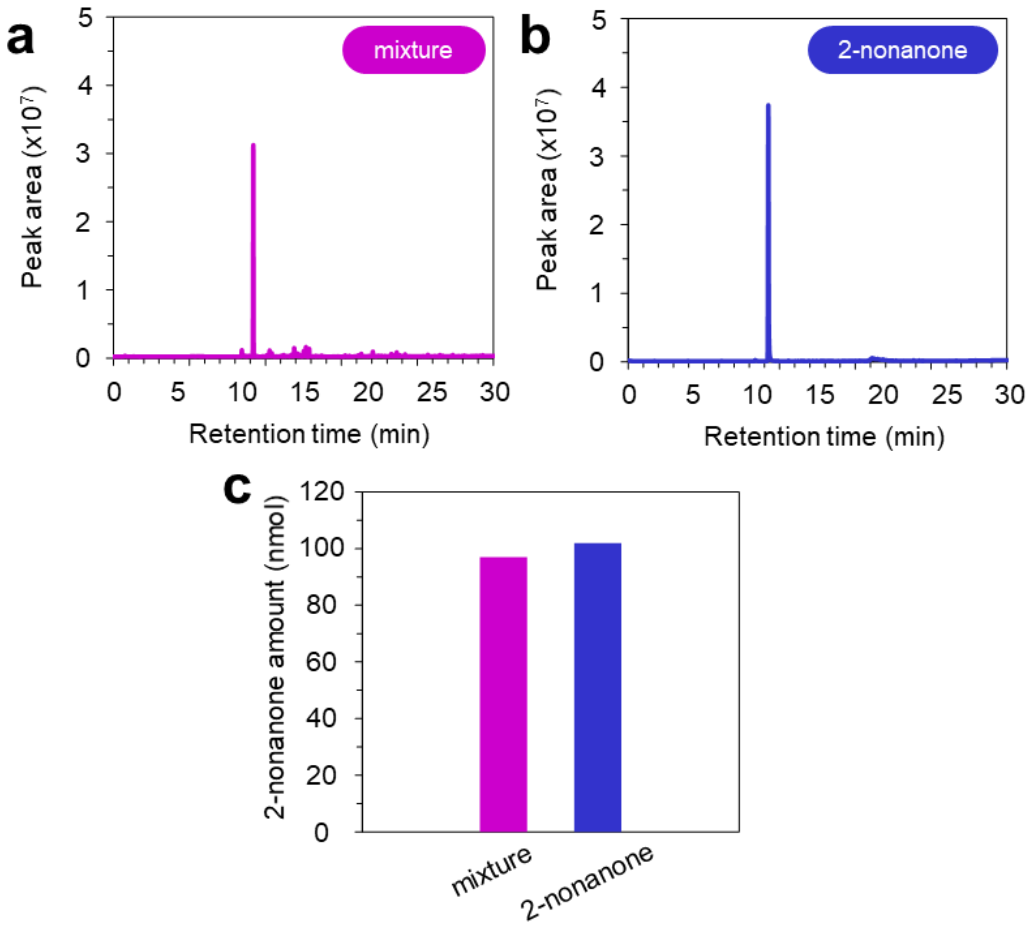

Figure S9. GCMS spectra of desorbed compounds when adsorbing (a) volatile molecule mixture (2-nonanone, nonanal, 1-nonanol and nonanoic acid) and (b) only 2-nonanone on sol-gel ZrO_2 coated ZnO nanowires (annealed at 400 ºC in air). (c) Desorption amount of 2-nonanone when adsorbing volatile molecule mixture and only 2-nonanone.

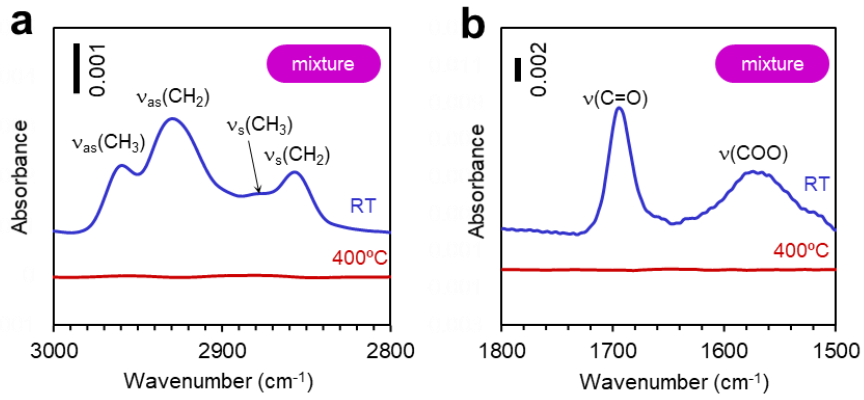

Figure S10. Molecular state on mixture-adsorbed sol-gel processed ZrO_2 surface and after annealed at 400 °C.

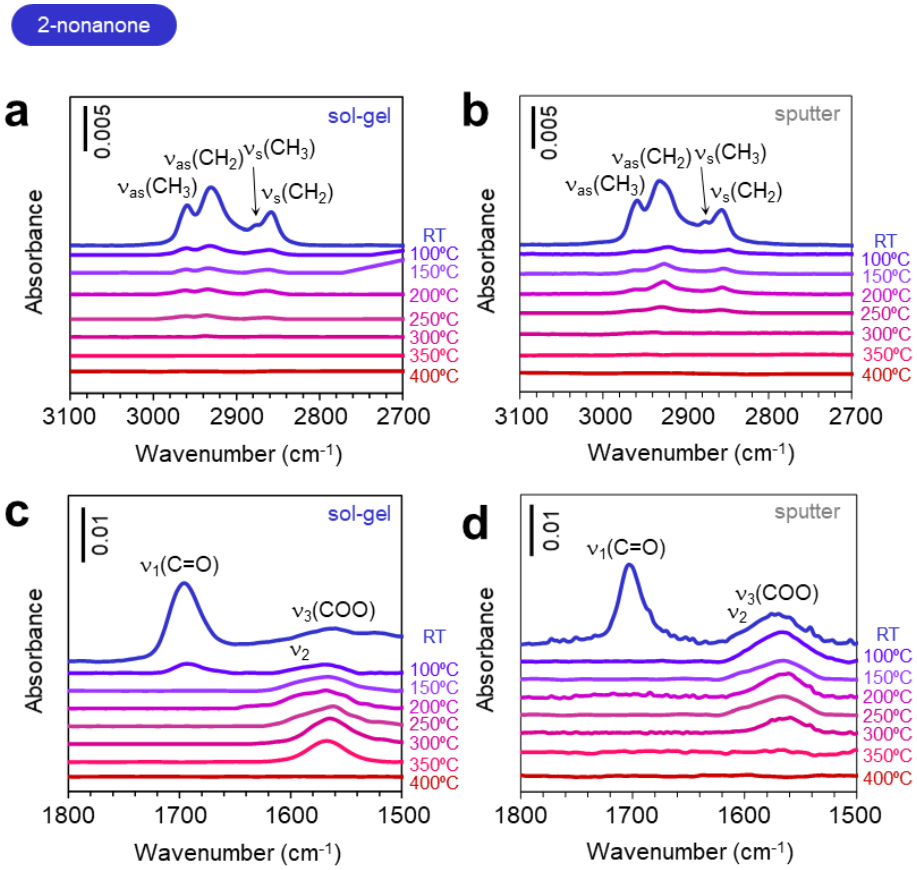

Figure S11. Molecular state in temperature dependent thermal desorption process on sol-gel and sputter ZrO_2 surface by FT-IR. a, b, covers the regions for alkyl group (2700-3100 cm^{-1}), a for sol-gel and b for sputter; c, d, covers the carbonyl region (C=O and COO, 1500-1800 cm-1), c for sol-gel and d for sputter.

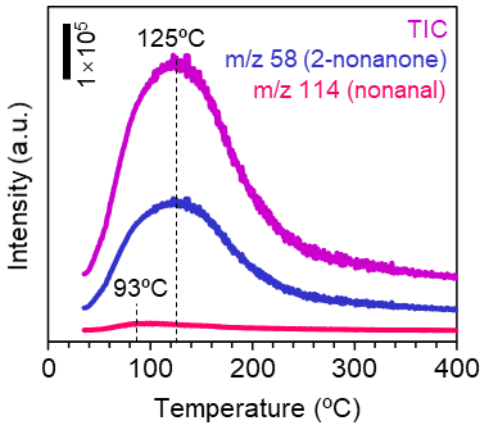

Figure S12. TPD/MS profiles of mixture-adsorbed sol-gel processed ZrO_2 surface (pretreated at 400 ℃ in air).

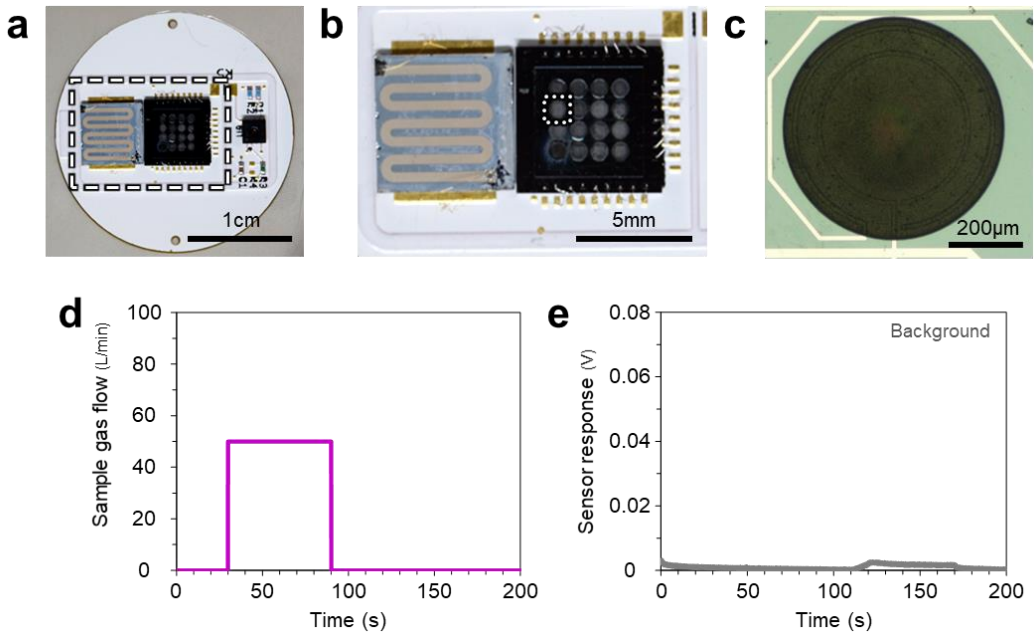

Figure S13. (a) Photograph and (b) close-up photograph of a nanowire-sensor hybrid device integrated on a circular-shaped PCB board. The nanowire chip is composed of sol-gel ZrO_2 coated ZnO nanowires, which was annealed at 400 ºC in air. (c) A typical optical microscopy image of chemisensitive resistor sensor. (d) Program of gas flow for the molecular sensing in a nanowire-sensor hybrid device. (e) Sensor response of a nanowire-sensor hybrid device when only N_2 carrier gas was flown.

CHAPTER VII

OVERALL CONCLUSION AND OUTLOOK

Although a large number of polymer sensors and metal oxide sensors have been commercialized and are extensively utilized in various fields nowadays, the upcoming era of IoT put forward higher technical demands on them. Long-term stability and suitable design of sensor device are key issues that determine the performance of the final sensor in practical application. In this thesis, we demonstrate that based on the understanding of chemical reaction on sensing material's surface, the long-term stability and selectivity of target molecule can be achieved.

The chemical reaction on PEG-carbon black nanocomposite sensor for degradation mechanism was well investigated by using a dual-use device with capable check for FT-IR and sensing performance. The results were shown in chapter III. By comparing the sensing properties and the IR spectroscopy on a same device, it revealed that the oxidation induced consumption of PEG was a key factor for the degradation of sensing performance. Depending on the mechanism, an anti-oxidizing agent (*i.e.* ascorbic acid) was incorporated into the PEG-CB nanocomposite sensor to inhibit the PEG oxidation and successfully proved its long-term sensing stability in ambient air for 30 days. Because the oxidation is a typical problem for polymer materials, the proposed method was feasible to various polymer-carbon nanocomposite sensors to promote their long-term stability. After that, in chapter IV, we investigated the material dependence of metal oxides (i.e. ZnO, ZrO_2, TiO_2) on the molecular adsorption behaviors of volatile molecules. Spectroscopic and spectrometric analyses revealed that the Lewis acidity of meal cations give a strong impact on the bonding strength of molecules but not on the adsorption amount. Since the performance of catalyst/molecular sensor/molecular filter is essentially determined via the adsorption/desorption behaviors of molecules on material surface, the proposed nanowire array structure based analytical platform and the obtained implications in this study offer a foundation to design the performance of

these nanoscale metal oxides based applications. In chapter V, we found in-situ fabrication of hydrothermally grown ZnO bridging nanosensors can substantially suppress the unintentional variations of electrical resistances between electrodes and significantly enhance the sensing responses for NO_2 with the smaller standard deviation and the lower limitation of detection compare with conventional shape edge seed layers. In chapter VI, we fabricated a highly active metal oxide surface with sol-gel processed ZrO_2 coated on ZnO nanowire array. This surface can achieve selective ketone sensing in mixture, because aldehyde i.e. nonanal is easily oxidated by activated oxygen on sol-gel ZrO_2 surface while ketone i.e. 2-nonanone with higher resistivity for oxidation remains on the surface. By combine this ZrO2 coated ZnO nanowire array as molecular selector with PEG-carbon black sensor, selective ketone sensing can be obtained. At the same time, this ZrO_2 surface exhibited excellent thermally robust for keep its selectivity at 400 ^oC for near 3×10^7 years.

However, there are still many obstacles in the practical application of metal oxide gas sensors. The effect of ambient environmental factors like temperature, humidity and ambient light cannot be ignored. In particular, the application of biomarker detection in human respiration is not accurate enough, because the large amount of moisture contained in the respiratory gas can disturb the sensing results. Integrating multiple detection devices based on different principles should be a possible way to improve recognition capabilities. In order to realize the next generation of innovation in the area of chemical sensors, the exploration of high-quality materials and new integration methods should be further explored.

LIST OF PUBLICATIONS

LIST OF PUBLICATIONS

Scientific Journals

1. **Wenjun Li,** K. Nagashima, T. Hosomi, C. Wang, Y. Hanai, A. Nakao, A. Shunori, J. Liu, G. Zhang, T. Takahashi, W. Tanaka, M. Kanai and T. Yanagida. "Mechanistic Approach for Long-term Stability of Polyethylene Glycol-Carbon Black Nanocomposite Sensor." ***ACS sensors, 2022,*** 7, 151-158. **(IF=7.711)**
2. **Wenjun Li,** Kazuki Nagashima, Takuro Hosomi, Jiangyang Liu, Tsunaki Takahashi, Guozhu Zhang, Wataru Tanaka, Masaki Kanai and Takeshi Yanagida. "Core-Shell Metal Oxide Nanowire Array to Analyze Adsorption Behaviors of Volatile Molecules." ***Chemistry Letters,*** *in press.*
3. **Wenjun Li**, K. Nagashima, T. Hosomi, G. Zhang, A. Nakao, Y. Hanai, H. Saito, T. Takahashi, W. Tanaka, M. Kanai and T. Yanagida. "Discriminative Ketone Sensing in Mixture by Promoted Reactivity on ZnO/ZrO_2 Core-Shell Nanowire Molecular Selector." ***In preparation***.
4. G. Wang, L. Liao, L. Niu, L. Chen, **Wenjun Li,** C. Xu, E. Mbeng, Y. Yao, D. Liu, and Q. Song. "Nuclei position-control and crystal growth guidance on frozen substrates for high performance perovskite solar cells." ***Nanoscale***, ***2019***, 11, 12108-12115. (**IF=7.79**)
5. J. Yang, J. Hou, Y. Niu, **Wenjun Li,** F Yi, S. Liu, G. Li, and M. Xu. "Improved cycle capability of Titanium-doped Fe2O3 anode material for Li-ion batteries." ***Journal of Alloys and Compounds, 2017,*** 722, 414-419. **(IF=4.715)**
6. J. Liu, H. Zeng, G. Zhang, **Wenjun. Li**, K. Nagashima, T. Takahashi, T. Hosomi, W. Tanaka, M. Kanai and T. Yanagida. "Edge-Topological Regulation for In-situ Fabrication of Nano-Bridging Sensors." ***In submission***